Evaluating the Role of Heterogenous Mechanical Forces on Lung Cancer Development and Screening

Dissertation

Presented in Partial Fulfillment of the Requirements for the Degree Doctor of Philosophy in the Graduate School of The Ohio State University

By

YouJin Cho

Graduate Program in Biomedical Engineering

The Ohio State University

2021

Dissertation Committee

Samir N. Ghadiali

Joshua Englert

Arunark Kolipaka

Abstract

Lung cancer is leading cause of cancer-related deaths in the United States with 5-year survival rate of 18.6%. This is due to late detection of lung cancer and problems in screening for lung cancer. Indeterminate pulmonary nodules (IPNs) are pulmonary nodules size between 7-20mm diameter solid nodules. 90% of IPNs are incidentally found and they are hard to diagnosis due to their small size and current diagnosis methods such as CT, PET scans and biopsy involve high exposure to radiation or invasive and could lead to complications.

The majority of lung cancer patients have non-small cell lung cancer (NSCLC) and 64% of these patients exhibit driver mutations such as epithelial growth factor receptor (EGFR), anaplastic lymphoma kinase (ALK) and Ras mutations. These patients have shown to have improved survival rate if they are treated with targeted therapies directed against the driver mutations. Although these patients initially show strong response to targeted therapies, most patients develop resistance to these targeted treatments through secondary point mutation and epithelial to mesenchymal transition (EMT).

The lung is a dynamic organ where alveolar epithelial cells are normally exposed to significant mechanical forces (i.e. ~8% cyclic strain, transmural pressure and shear stress) while primary lung tumor cells experience a 40-fold decrease in these mechanical

forces/strain. Although biomechanical factors in the tumor microenvironment have been shown to be a significant driver of cancer progression, there is limited information about how biophysical forces alters drug sensitivity in lung adenocarcinoma cells. Based on the known importance of mechanical forces/strain on lung injury and repair and the significant difference in cyclic strain applied to normal and cancer cells in the lung, we hypothesized that cyclic mechanical strain would activate important oncogenic pathways and alter drug sensitivity. Although local mechanical properties of the lung tumor may be an important prognostic factor, there is currently no way to non-invasively assess local lung mechanical properties.

Magnetic resonance electrography (MRE) is a non-invasive imaging technique that uses shear wave propagation to measure mechanical stiffness of soft tissues. Dr. Kolipaka's lab has developed an MRE protocol that can measure temporally and spatially varying changes in lung tissue stiffness from normal adults. Furthermore, MRE has been used to quantify a 3-fold increase in lung tissue stiffness in fibrotic patients compared to normal controls. However, MRE has not been used to evaluate the stiffness profile of tumors within in lung cancer patients.

Therefore, in this study, we test the hypothesis that the mechanical forces present within lung tumor microenvironment plays an important role in tumor progression and therapeutic response. Based on this hypothesis, we propose to 1) define different biophysical forces present in lung tumor microenvironment 2) investigate role of biomechanical forces in drug response and migratory behavior on the lung adenocarcinoma cells *in-vitro* and 3) verify and identify the biomechanical forces in

patients with using the non-invasive imaging (i.e. MRE) and finite element modeling (FEM).

The overall goal of this study is to both obtain a better understanding of how dynamic biomechanical forces in the lung tumor microenvironment affect tumorigenesis and therapeutic response and to establish a clinically-relevant methodology to non-invasively assess local tumor mechanical properties in patients with IPN. Using finite element modeling of idealized lung model with tumor, the study have shown that the there are heterogeneous strains and stresses present – low strain in stiff center of tumor, high strain and strain gradient in the peritumoral region. Using this a novel in-vitro system was developed to deliver non-uniform deformation. Our study has shown that high strain and strain gradient led to increase in migration and increase in response to drug therapy. Furthermore, in this study, novel non-invasive technique was developed using MRE and FEM. This technique highlighted the importance of the heterogeneity spatial stiffness is important in characterizing strain magnitude and spatial strain gradient in normal, CF and IPN patients.

Dedication

In loving memory of Joyce and Dennis.

Also, I dedicate this dissertation to my family, friends and all who helped me get here.

Acknowledgments

I would like to thank my advisor Dr. Samir Ghadiali for his guidance, support and mentorship throughout my journey through PhD. His advice and guidance have allowed me to grow both personally and professionally. I would also like to thank my committee members Dr. Joshua Englert and Dr. Arunark Kolipaka for their advice and continued support.

I would like to thank my mentors. Dr. Vasudha Shukla for continued endless support and advice during my time in the lab. She has not only provided with numerous advice on the research but also she has been giving endless numerous support throughout my time at the Ohio State University. Furthermore, I would like to thank Dr. Cassandra Guarino and Dr. David Infanger for their inspiration and motivation in research during high school and college education. Their passion and advice have always been a driving force for me during my PhD studies.

I thank the contributions of: Dr. Faisal Fakhouri and Dr. Vasudha Shukla for their time and help on the projects. I also thank all the past and present members of Dr. Ghadiali's lab: Dr. Chris Bobba, Dr. Justo Torres-Rodriguez, Rachel Zielinski, Dr. Kevin Nelson, Dr. Jennifer Malik, Tricia Oyster, Basia Gabela-Zuniga, Qinqin Fei, Chris Chang, Kelsey Watts, Grant Chudik, and Yevgeniy Gladiky. I would also like to thank

past and present members of Dr. Englert's lab: Wenjuan Zhang, Adam Streicher, and Hyunwook Lee.

I thank the members of Ohio State University Biomedical Engineering Department especially Melanie Senitko, Kirsten Gibbons, and Jada Harmon for their continued support and help.

Lastly, I would like to thank the Ohio State Medical Scientist Training Program. To both directors of the program, Dr. Lawrence Kirschner and Dr. Tamar Gur, for providing advice, and programmatic support. Also sincere thanks to Ashley Bertran for her continued support and time in the MSTP program.

Vita

2010…….Ithaca High School

2008-10…….....….Research Assistant, Chemical Engineering, Cornell University

2014……..……B.S. Biological & Environmental Engineering, Cornell University

2010-14……..……. Research Assistant, Biomedical Engineering, Cornell University

2013-14…Teaching Assistant, Biological Engineering/Biochemistry/ Physical Education, Cornell University

2016…….....……...Graduate Teaching Assistant, Biomedical Engineering, The Ohio State University

2017…….....University Fellowship, Biomedical Engineering, The Ohio State University

2020…Graduate Teaching Assistant, Biomedical Engineering, The Ohio State University

2018-present.....……..…Graduate Research Assistant, Biomedical Engineering, The Ohio State University

2018-present.....Medical Scientist Training Program, the Ohio State University

Publications

Cho, Y., Fakhouri, F., Englert, J., Kolipaka, A. & Ghadiali, S.N. Computational Using Magnetic Resonance Elastography and Computational Modeling to Evaluate Heterogeneous Lung Biomechanical Properties during Cystic Fibrosis. *NMR in Biomedicine*. (2021). Manuscript in preparation

Cho, Y., Shukla, V., Englert, J. & Ghadiali, S.N. Understanding the non-uniform deformation in lung cancer migration. *Journal of Biomechanics.* (2021). Manuscript in preparation

Cho, Y., Fakhouri, F., Englert, J., Kolipaka, A. & Ghadiali, S.N. Using Mechanical Properties for Early Diagnosis for Indeterminate Pulmonary Nodules. *NMR in Biomedicine*. (2021). Manuscript in preparation

McCallinhart, P., **Cho, Y.**, Sun, Z., Ghadiali, S. N., Meininger, G. A. & Trask, A. J. (2020). Reduced Stiffness and Augmented Traction Force in Type 2 Diabetic Coronary Microvascular Smooth Muscle. Amer J of Phys-Heart and Circulatory Phys, 318(6): H1410-H1419.

Jones, C. E., Hammer, A. M., **Cho, Y.**, Sizemore, G. M., Cukierman, E., Yee, L. D., Ghadiali, S. N., Ostrowski, M. C. & Leight, J. L. (2019). Stromal PTEN Regulates Extracellular Matrix Organization in Mammary Gland. Neoplasia, 21(1): 132-145.

Infanger, D. W., **Cho, Y.**, Lopez, B. S., Mohanan, S., Liu, C., Gursel, D., Boockvar, J.A . & Fischbach C. (2013). Glioblastoma stem cells are regulated by interleukin-8 signaling in a tumoral perivascular niche. Cancer Research, 73: 7079-7089.

Fields of Study

Major Field: Biomedical Engineering

Table of Contents

List of Tables

List of Figures

Chapter 1. Introduction

Lung Cancer

Lung cancer is the leading cause of cancer related deaths in the United States. In 2018, there was estimated to be 234,030 newly diagnosed lung cancer and 154,050 estimated deaths[1]. Lung cancer's five-year survival rate is 18.6% which is very low compared to other types of leading cancers such as colorectal (64.5%), breast (89.6%) and prostate (98.2%)[2]. This low survival rate is due to late detection from lack of proper screening – only 16% of lung cancer cases are diagnosed at early stage when the cancer is pre-metastatic and localized within the lungs[2]. Although, early detection through screening could increase the lung cancer survival rate, there is currently an ongoing debate regarding the cost-effectiveness and risks associated with lung cancer screening.

The American Cancer Society recommends yearly screening for individuals between 55 to 74 years old with smoking history of 30 pack year. Lung cancer screening is done through low dose computed tomography (LDCT) where early detection can reduce lung cancer mortality by 14 to 20% in high-risk populations[3]. Although early screening reduces mortality rate for lung cancer, LDCT still has risks for radiation exposure, false positive and false negative findings and overdiagnosis[3].

Indeterminate pulmonary nodules (IPN) are small lung nodules with diameter between 6-20mm in size that are found incidentally through computed tomography (CT)

scans. 90% of IPN are incidentally found when patients are undergoing CT scans. Although majority of the IPNs are benign, current diagnosing tools are not optimal[4]. Current Fleischner Society 2017 Guidelines[5] look at the nodule size and risk factors (i.e. age, gender, family/smoking history) to determine if the patients need further follow-up. If the patients are in low-risk group – young age, no smoking history, no family history – following guidelines are followed. If the nodules are < 6mm in size the nodule is most likely benign and there is no need for routine follow up. Nodule size between 6-8 mm they recommend follow-up CT within 6-12 months and afterwards 18-24 months. If there is change in size within these monitoring period, the patients undergo positron emission tomography (PET)/CT scan and/or biopsy to determine if the nodule is benign or malignant. For nodule size >8mm, follow-up CT at 3 months and PET scan and/or biopsy is required.

For high-risk patients – older age, with smoking history and with positive family history – different guideline is followed. If nodule size is <6mm, CT follow-up in 12 months is recommended. For nodule size between 6-8mm, they recommend follow-up CT within 6-12 months and afterwards 18-24 months. For nodule size >8mm, follow-up CT at 3 months and PET scan and/or biopsy is required. With these imaging guidelines if there is increase in risk for lung cancer as discussed above based on size and risk factors, patients undergo further imaging through PET scan and/or biopsy through bronchoscopy or fine needle biopsy[5]. However, these imaging and biopsy methods are not very efficient in identifying the lung cancer at proper stage. Figure 1 shows the current prediction model for diagnosis IPN and future optimal diagnosis. Current prediction models only

can define 21% as low probability and 15% of patients as high probability. 64% of current patients with IPN undergo unnecessary PET scan and or biopsy[4]. Optimally, as show in Figure 1, the goal is to reduce the red box percentage from 64% to 35% to reduce the number of patients with IPN to undergo invasive biopsy. In order for this to happen, we need better ways to determine the IPN to low and risk group to reduce the number of people undergoing invasive biopsy.

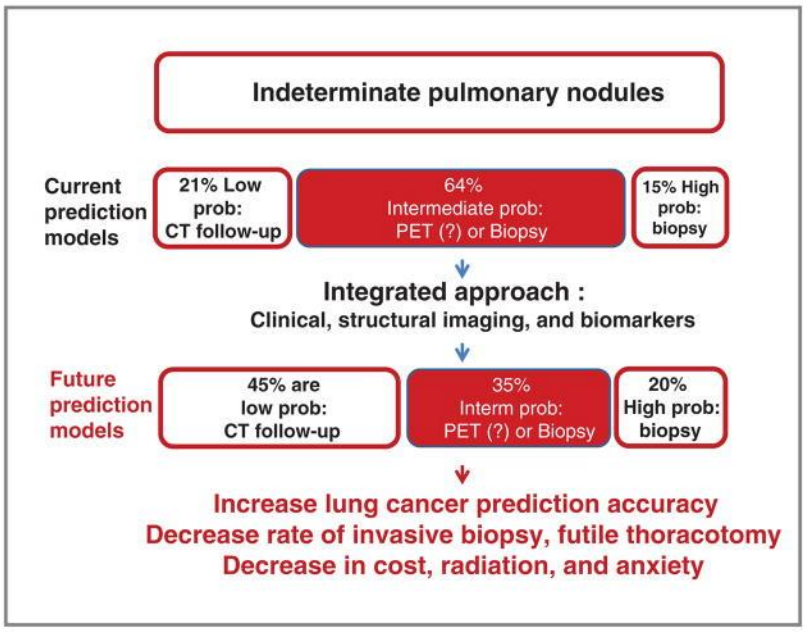

Figure 1. Current IPN diagnosis guideline and future prediction models. Adapted from Massion, P.P. (2014), Cancer Prev, 7 (12): 1173-8.

Furthermore, 80-85% of lung cancers are non-small cell lung cancer (NSCLC). For the stage I, II, IIIA patients, surgical resection is the first line therapy which is often accompanied by adjuvant treatments such as chemotherapy, radiation and/or targeted therapy. However, 40% of the diagnosed patients are at stage IV, and cytotoxic

chemotherapy is the first-line therapy[6]. Among NSCLC patients, 64% exhibit driver mutations such as epithelial growth factor receptor (EGFR), anaplastic lymphoma kinase (ALK) and Ras[7]. Patients with identified mutations are often treated with targeted therapies which have shown to improve patient survival in NSCLC[8]. Within NSCLC patients, 10-15% exhibit EGFR mutation, 10-25% Ras mutation and 3-7% ALK mutations[9]. Although EGFR and ALK have established targeted therapies such as elrotinib or gefitinib and crizotinib respectively, patients develop resistance to these targeted therapies due to the development of point mutations and chromosomal rearrangements[10, 11]. Although some 3rd generation therapies, including osimertinib, can target these secondary point mutations, drug/chemotherapy resistance continues to be a significant problem in the pulmonary oncology field and there is a clinical need for biomarkers that better predict response to targeted therapies.

Cancer Metastasis and Biomechanics

Cancer metastasis is the cause of 90% of cancer-related fatalities. It is marked by detachment of cancer cells from primary tumor site and invasion into blood circulation[12]. The cells survive in the circulatory system and extravasate into different locations and initiate tumor growth (Figure 2). Epithelial-mesenchymal transition (EMT) is a biological process where the cells lose the epithelial-like characteristics and become more motile is one mechanism by which cancer cells in the primary site gain invasive potential[13-16]. Furthermore, recent studies have shown evidence that biophysical forces

present in tumor microenvironment causes cancer cells to become more motile and influence EMT process[17-21].

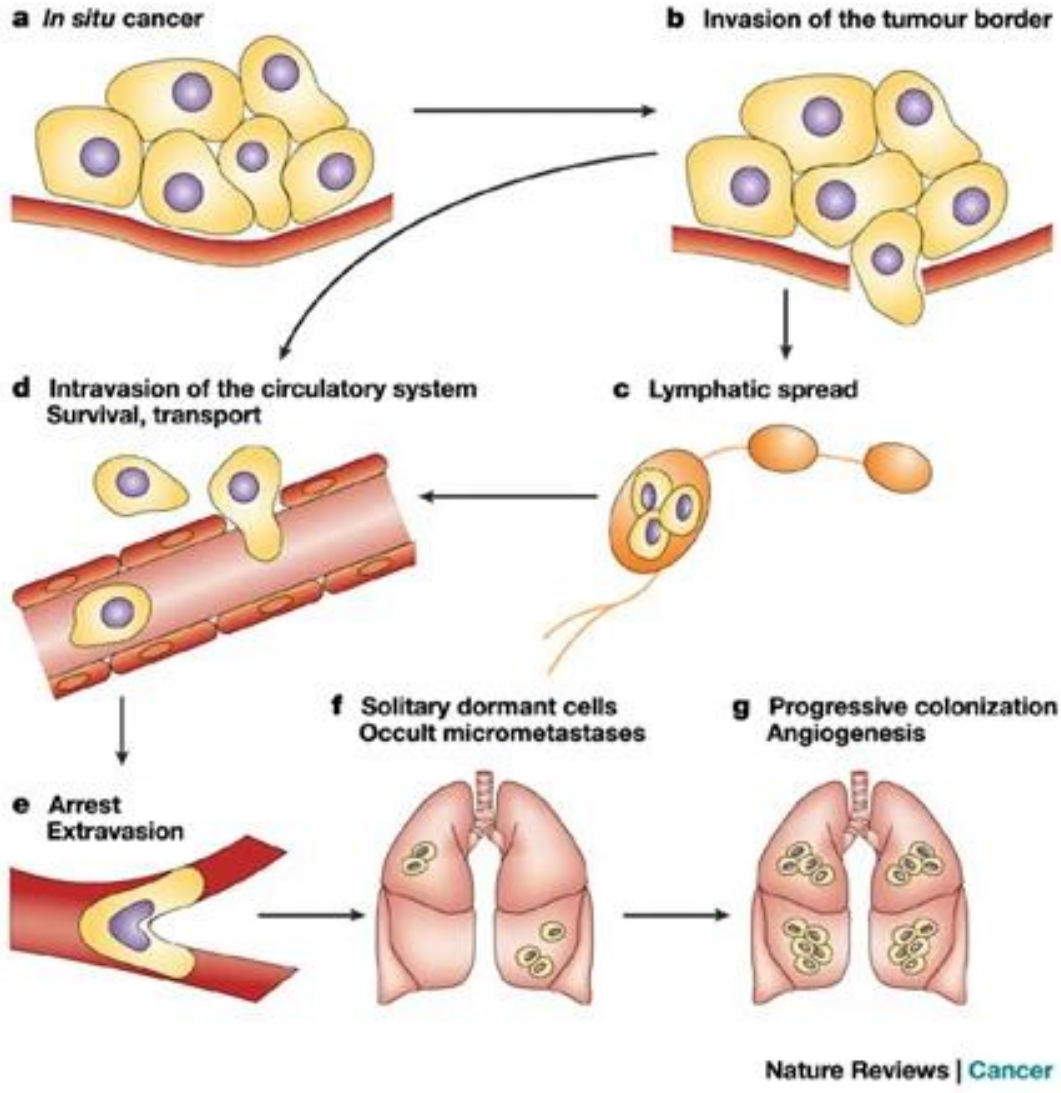

Figure 2. Process of metastasis Process of metastasis Process of metastasis a) cancer at primary site b) metastatic cells invade out of tumor border and can enter c) lymphatic system or d) directly into blood circulation. The cells in circulation survive and e) extravasate into other organs. f) some cells may remain dormant for over years and/or g) progress into colonization of the site. Adapted from Steeg, P. S. (2003), Nat Rev Cancer, 3(1): 55-63.

Myoferlin (MYOF) is a membrane vesicle trafficking protein. Knocking down MYOF have shown to reverse EMT in highly metastatic MDA-MB231 breast cancer cells and results in significant decrease in migration and invasion[22, 23]. Overexpression of MYOF expression was found in breast cancer which plays important role in controlling EGFR degradation[24]. In lung cancer, increased MYOF expression correlates with worse outcomes[25]. Although there is correlation between lung cancer and MYOF expression, currently there is limited in understanding of how MYOF alters EMT signaling and cellar biomechanics to alter migratory potential and EGFR expression changes.

The tumor microenvironment (TME) is very complex. TME consists of various cell types such as fibroblasts, endothelial cells, pericytes, immune cells and inflammatory cells. Cross talks between different cell types activate and differentiate the cells to promote tumor growth and progression. Immune cells such as T-cell, B-cell, tumor associated macrophages are present within TME to cross talk between the cancer cells and stromal cells. They produce chemokines induces cell signaling in various cells present within the TME such as endothelial cells and pericytes stimulating process for angiogenesis[26]. Furthermore, cancer-associated fibroblasts (CAFs) are myofibroblasts that are present in TME[27] and they are derived from multiple precursors in TME such as endothelial cells, smooth muscle cells, mesenchymal stem cells[28-30]. These CAFs secrete chemokines and growth factors such as TGF-β to promote EMT[31]. In addition CAFs play important role in secretion and remodeling of extra cellular matrix (ECM) of TME[31].

Majority of the ECM proteins such as collagen, fibronectin, laminins, proteoglycans and polysaccharides are produced by CAFs. Increased deposition of these

ECM proteins and increased crosslinking of collagen and elastin leads to increased matrix stiffness of TME. As the tumor progresses the ECM constantly undergoes remodeling through matrix metalloproteinase (MMP). MMPs play important role in breaking ECM degradation for tumor cell migration and matrikine production. This further triggers extracellular matrix renewal and increased cellular proliferation[32]. As shown in Figure 3, dense tumor mass causing compressive stress within the interior of the tumor and circumferential tension on the periphery of tumor[33]. Studies have shown that increased solid stress in lung cancer causes increased migration in 2D[34, 35]. Furthermore, tumor progression is marked by increase in deposition type I collagen and fibronectin and remodeling of ECM and leads to increased stiffness and decrease in ECM stiffness as you migrate away from the tumor edge.

Change in matrix stiffness have shown to affect cell motilities in several 2D studies[36, 37]. Another study has shown that there is increase in contractility and force generation in breast, prostate and lung cancer with increase in stiffness[38]. Not only the stiffness of the ECM plays important role in inducing cell motility but also the orientation of the fibers direction play important role in cell migration in TME. Study have shown that more malignant tumor had irregular invasive boundaries marked by radial alignment of the collagen fibers[39] that can lead to structure guided cell motility[40]. Collectively, these previous studies demonstrate that there are various biophysical mechanical forces that are present in tumor microenvironment which play an important role in tumor motility and drive metastasis. TME is complex and has shown evidence there are spatial heterogeneities in ECM that play important role in cancer migration and progression.

Lung microenvironment introduces additional complexity to lung cancer TME through externally applied loads that are temporally and spatially heterogeneous.

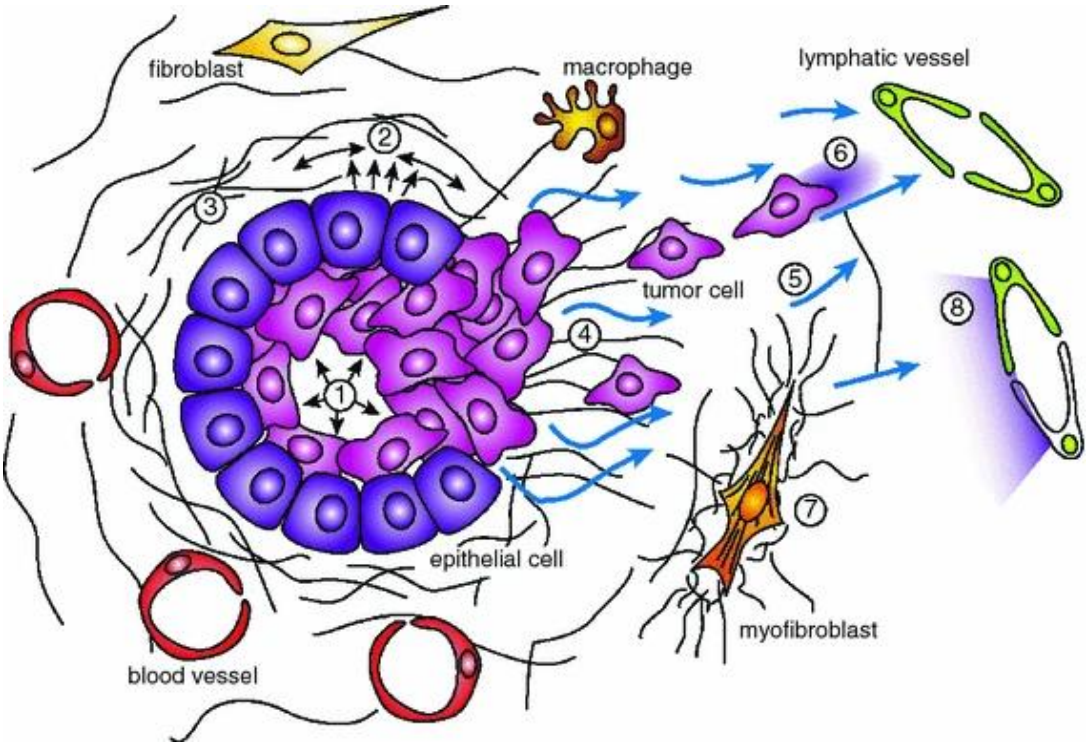

Figure 3. Tumor microenvironment and biomechanical forces. 1) highly dense tumor from increased proliferation results in tumor stress 2) ECM becomes more dense and stiffer 3) towards the edge of the tumor microenvironment matrix becomes reorganized 4) fluid pressure increases resulting in angiogenesis 5) increased lymphatic drainage and gradient 6) increased interstitial flow induces myofibroblast differentiation 8) and chemokine secretion. Adapted from Shieh, A. C. (2011), Annals of Biomed Eng, 39(5): 1379-1389.

Lung Biomechanics

Lung is a highly dynamic mechanical organ. The primary function of the lungs is gas exchange, bringing in oxygen (O_2) into the body and removing carbon dioxide (CO_2).

Changes in the pressure within the lungs drive the inhalation and exhalation of the air. Figure 4 shows normal negative pressure ventilation. During inhalation, the diaphragm contracts, the chest wall muscles contracts to expand the lungs. This causes a drop in air pressure within the lungs that drives the air from the outside to enter the lungs. After proper gas exchange in the alveoli, the body begins the exhalation process where the chest wall muscles and diaphragm relaxes back into the normal position and chest contracts back to normal called elastic recoil. The pressure within the lungs increases and push the air out from the lungs.

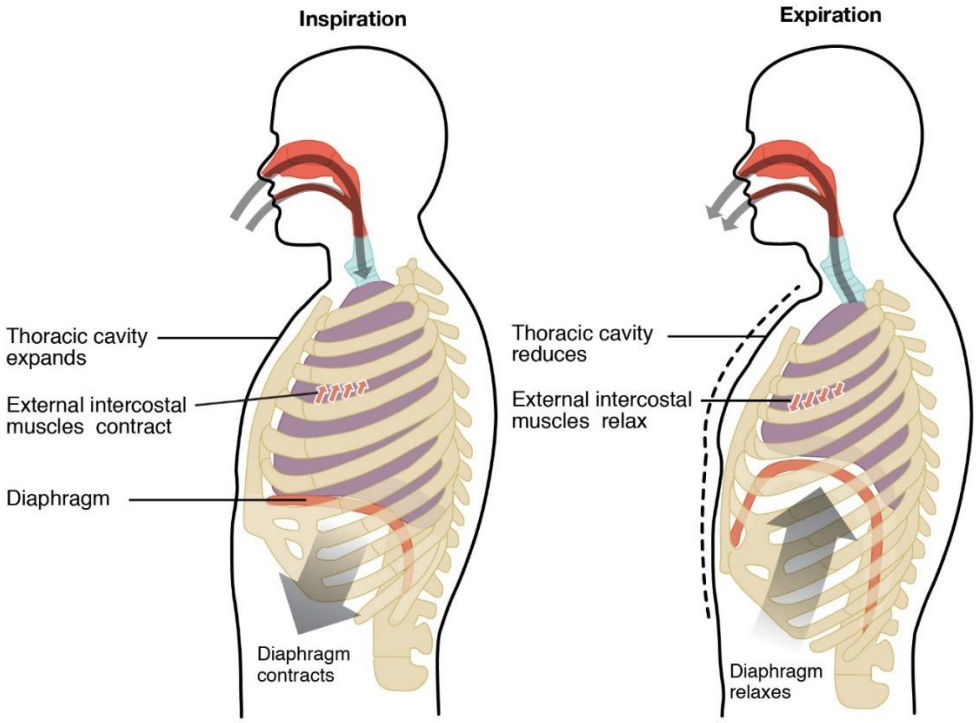

Figure 4. Schematic for normal breathing. Left image shows the inhalation process where negative pressure from chest expansion and diaphragm drives air to enter the lung. Right image is the process of exhalation where positive pressure from relaxation of chest and diaphragm drives the pressure out. Adapted from https://openstax.org/books/anatomy-and-physiology

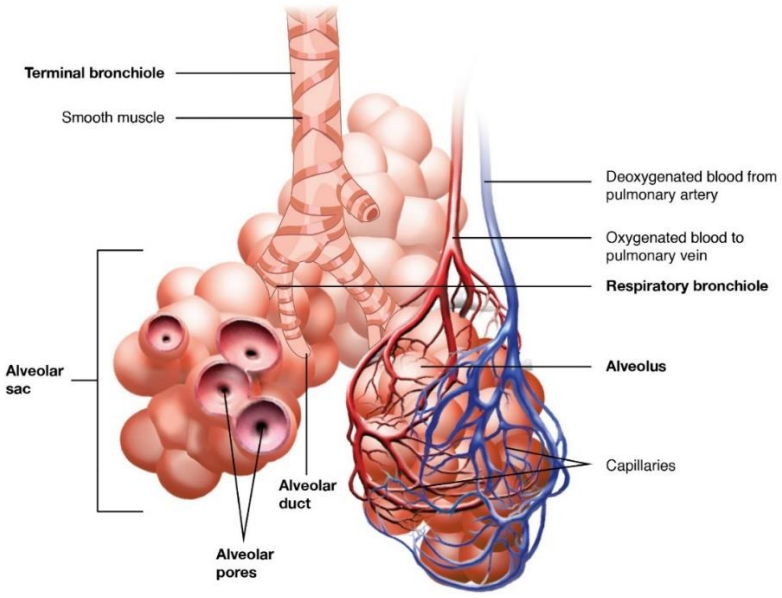

Figure 5. Respiratory zone of the respiratory system. Air comes through the bronchioles and lead to alveolar sac where the gas exchange occurs. Adapted from https://openstax.org/books/anatomy-and-physiology

As the cyclic breathing pattern repeats at the macroscopic level as discussed above, the microstructures within the respiratory zone, including the alveoli, are constantly undergoing cyclic deformation. As the air enters into the bronchioles, alveolar sac and to individual alveoli, the walls the of each alveolus undergo elastic stretch (Figure 6). Breathing results in cyclic inflation/deflation and deformation of lung tissue and exposes cells in the lung microenvironment to cyclic tensile strains (i.e. stretching deformations) [41]. Previous studies have found that normal breathing exerts 4-10% cyclic strains on normal alveolar epithelial cells at the frequency of 0.2 Hz (12 breaths/min)[42, 43]. Several studies have demonstrated that these normal physiological strains promote homeostatic cellular responses including surfactant production, epithelial cell

proliferation and differentiation and prostacyclin production [44-47]. However, the degree of tissue deformation and tensile strain is highly dependent on the local stiffness of lung tissue and altered tissue stiffness and/or lung compliance during several pulmonary disorders may significantly alter the degree of tensile strain in the lung. As a result, developing non-invasive tools that can monitor changes in the lung's biomechanical properties during disease is a major area of research.

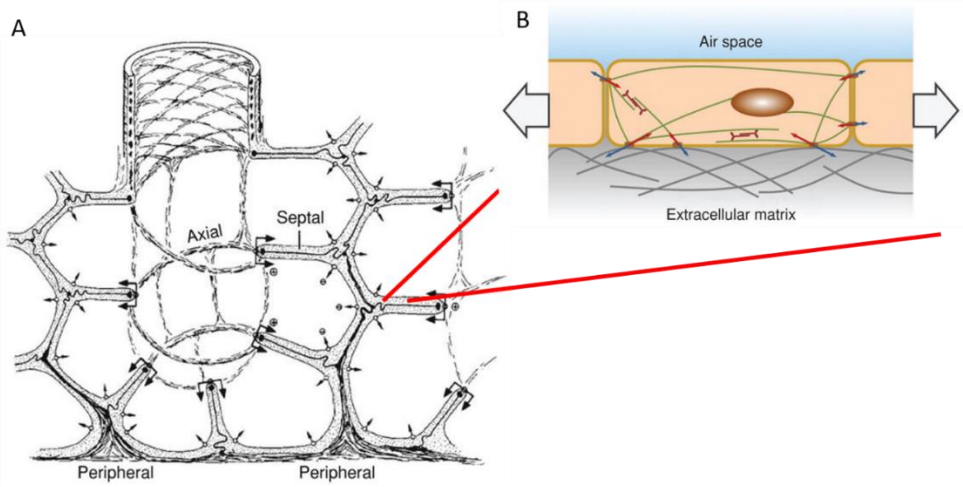

Figure 6. Alveolar sac and forces present A) shows the surface forces that are present on each alveolus B) cyclic strain that each alveolar epithelial cell experience is shown. Adapted from Waters, C.M. (2012). Compr Physiol, 2(1): 1-29.

Several respiratory diseases involve changes in the lung's extracellular matrix (ECM) composition/structure results which alters lung tissue stiffness and inhibits normal lung function. For example, degradation of the ECM during COPD leads to parenchymal destruction, enlarged alveoli, decreased lung stiffness and reduced elastic recoil during

exhalation[48]. Conversely, excessive matrix production and deposition during pulmonary fibrosis leads to increased lung stiffness and reduced lung expansion during inhalation[49]. Modulation of the ECM during lung cancer can also lead to increased lung stiffness[50] while excessive mucus production can elevate lung stiffness during cystic fibrosis [51]. Importantly, at the cellular level, altered substrate/tissue stiffness has been shown to directly modulate cellular function[52-54] and regulate the mechano-transduction processes that lead to fibrosis[55].

In addition to changes in tissue stiffness, it has been recently recognized that changes in tensile strain magnitude and the development of spatial gradients in strain may also influence the cellular mechanobiology processes that contribute to lung disease. For example, excessive mechanical strain during artificial ventilation and during impaired alveolarization can exacerbate lung injury and inflammation[56] and can cause epithelial and endothelial cell injury and dysfunction[42, 57]. Furthermore, the heterogenous spatial distribution of strain within the deforming lung[58, 59] will lead to significant spatial gradients in strain and these spatial strain gradients have been shown to alter fibroblast orientation and contractility[60, 61]. Therefore, developing non-invasive tools that can quantify regional lung stiffness is an important clinical need.

Models to Study Lung Mechanics

Different models have been developed to study the mechanics of the lungs – *in-vitro*, *in-vivo* and computational modeling. For *in-vitro* models, stretching devices have been developed to study the effect of cyclic tension on lung epithelial and endothelial

cells as occurs during both normal and abnormal ventilation. Numerous studies have applied cyclic deformation on lung carcinoma cells A549 or alveolar type I/II cells by seeding monolayer of cells on an elastic polydimethylsiloxane (PDMS) membrane and putting on cyclic forces ranging from 10-30% uniaxially via using compression device (Figure 7 A) [45, 46, 62, 63] and biaxially vacuum pump (Figure 7 B)[64-66]. Figure 7 A works by putting PDMS membrane on membrane chamber with sliding blocks on each end. The compression motor device then moves that derives the chamber to slide laterally on each end applying uniaxial deformation. Figure 7 B is Flexcell system and it works by using vacuum pump to pull down on silicone membrane against circular post which applies biaxial deformation on the membranes. Major limitation with these stretching systems is that 2D monolayer of cells does not recapitulate the 3D mechanical environment of the lung.

Another form of 2D in-vitro system is a Lung-on-a-chip device that mimics the physiology of breathing[67-72]. This device allows you to coculture different cell types generally lung epithelial cells on one side of the PDMS membrane representing gas interface of the alveolar sacs and endothelial cells on the opposite side of the PDMS membrane representing the liquid interface of the blood vessel. The lung on a chip allows you to mechanically stimulate the device as well as create separate liquid and gas interface to model the gas exchange apparatus (Figure 7 C). Although these lung-on-a-chip systems better recapitulate the microenvironment compared to 2D cell culture experiments, they still lack vascular network, immune cells and other stromal cells[73].

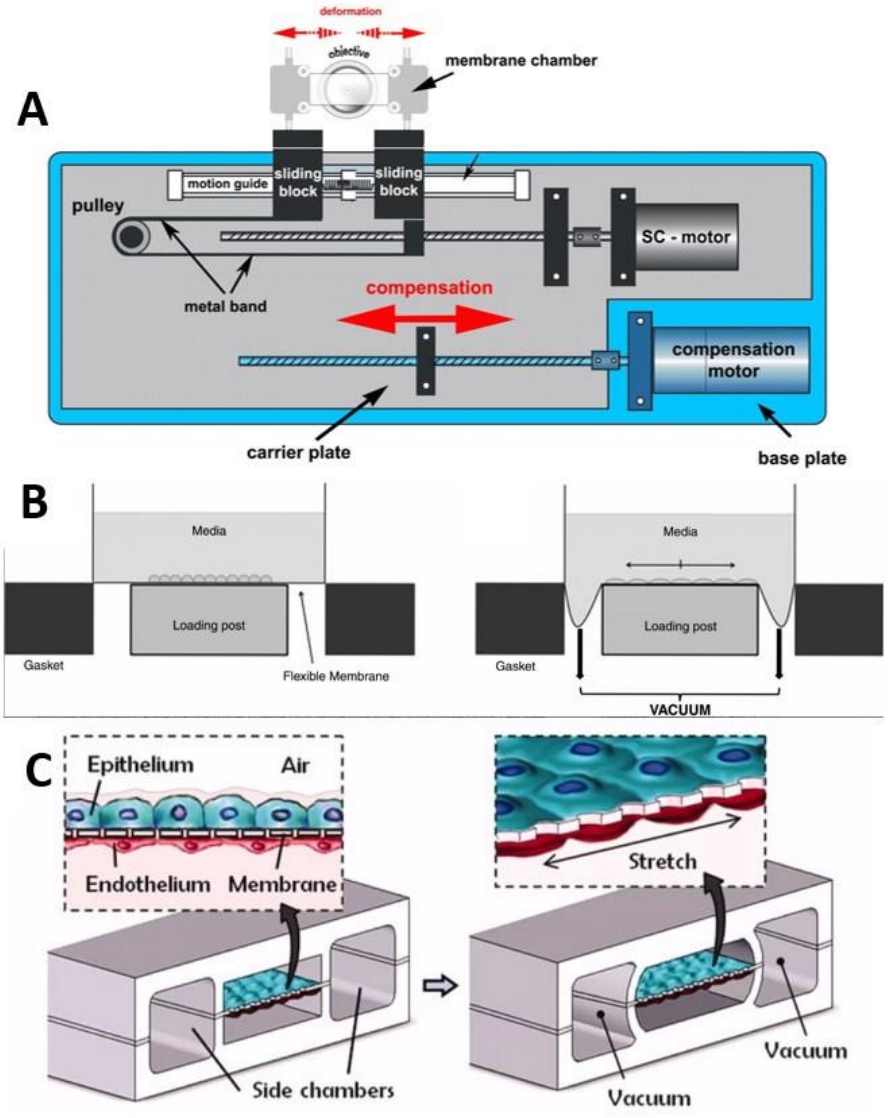

Figure 7. Schematic of current *in vitro* models A) Stretching device using the pump. Adapted from Lutz, A. (2020), *FASEB J*, 34(8):11227-11242. B) stretching device using the vacuum pump to pull down on the membrane. Adapted from Schmitt, S. (2012), *Assay Drug Dev Technol*, 10(2): 137-47. C) lung-on-a-chip model displaying air and liquid interface and stretching. Adapted from Huh, D. (2010), *Science*, 328(5986):1.

To overcome the limitations of *in-vitro* model, *in-vivo* studies have been carried out in the animal models. Study of lung mechanics are performed on but not limited to

mice, rats, pigs, and goats[74-79]. Animal studies are conducted by putting the animals under anesthesia and connecting them to mechanical ventilator. For example, for mouse studies, needle is inserted into trachea which is connected to computer-controlled small ventilator. Using controlled ventilation, pressure-volume curves, tissue dampening, tissues elastance, hysteresivity can be calculated using animal models[79]. Hysteresivity is a material property of tissue that measures the ratio of energy dissipated per cycle over the stored potential energy at maximum stretch[80]. The ventilated tissues can also be further analyzed for tissue stiffness, protein expression studies, etc. Different cell types are present in animal model allows direct measurements of tissue stiffness and expression with the presence of other cell types (i.e. immune cells). However, there are limitations where they have found that even different animal model properties, the lung mechanics differ[79]. Meaning that the animal models do not properly recapitulate the anatomy of human lungs. Furthermore, the animal models lack the ability to precisely control the mechanical forces that occur that will not allow look at regional mechanical deformations.

Direct measurements of lung deformation *in-vivo* in human can be obtained by using imaging techniques and computational modeling. CT-based techniques have been used to document heterogenous lung deformation *in-vivo*[58]. 4-dimensional computed tomography (4DCT) takes sequential images using 3-dimential computed tomography (3DCT). Using image registration, the 4DCT images can be used to calculate volumetric strain by aligning structures and calculating regional deformation that occurs during breathing. Although the use of 4DCT allows for measurement of volumetric strain, it

does not offer information on the directionality of the deformation. Furthermore, 4DCT relies heavily on the structural landmarks. If there are any lung abnormalities or injury, lack of landmark may lead to challenges. In addition to imaging, finite element models have been used to study lung breathing motion, gravitational effect on human lung deformation[81], and lung tumor motion simulation[82]. These computational models take the 3DCT or 4DCT images, recreate the geometry and simulate breathing to calculate regional deformation within the lungs. However, main limitation of these computational models assume homogenous stiffness distributions[82-86] and therefore cannot capture the spatial variations in lung deformation observed *in-vivo*.

Magnetic Resonance Elastography

Elastography is non-invasive technique that is used to measure soft tissue stiffness. The elastography works by introducing vibration and the images of the organs are taken through various conventional imaging modes such as ultrasound, computed tomography (CT) and magnetic resonance imaging (MRI). The images are taken at each phase, the propagating waves are processed to estimate their wavelengths and calculate stiffness of the tissues with assumption of isotropy, homogeneity and incompressibility of the materials [87]. Numerous studies have been done using ultrasound elastography (UE) to study different lung diseases[88-91], and especially in primary lung tumor UE have found that there is 40-fold decrease in lung deformation in the region of tumor[91]. And although mechanical differences of different lung disease can be detected with UE, depth of

measurement is shallow and offers limited information. There are several studies using CT elastography on lungs[92-94]. However, the problem still remains using CT will expose patients to high dose of radiation and risk further complication.

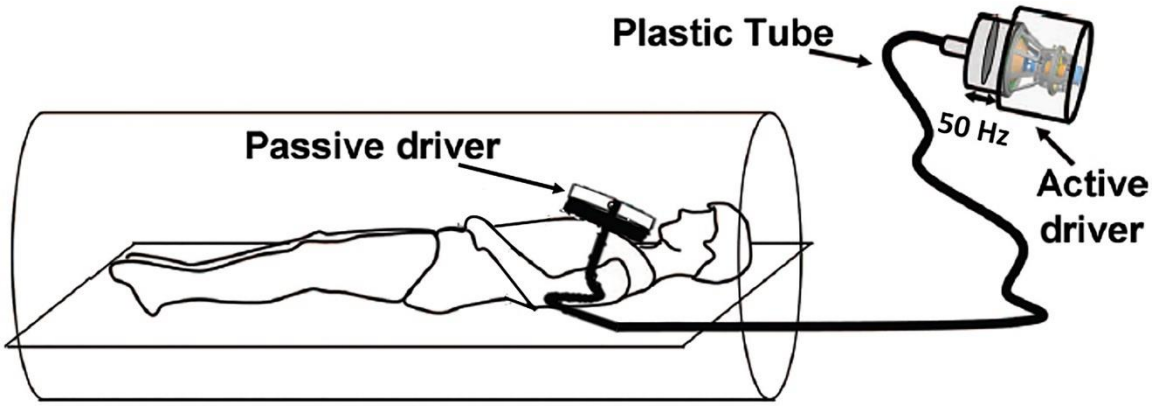

Figure 8. Schematic for MRE scan on lungs. MR compatible driver is placed at the apex of the lung and the vibrations is introduced by the active driver. Adapted from Fakhouri, F. (2019), NMR in Biomedicine, 32(7): e4102.

Magnetic resonance elastography (MRE) is noninvasive imaging method that uses phase-contract (PC) magnetic resonance imaging (MRI) to measure shear stiffness in various organs such as lungs, pancreas, liver and breast[95-99]. MRE works by placing a driver that introduces mechanical vibrations (Figure 8). The external vibrations are then synchronized to motion-encoding gradients (MEG) to calculate the displacement fields in the MR images which then can be used to obtain stiffness maps[87]. MRE has been previously used in lungs to study lung stiffness where during total lung capacity (TLC) was significantly higher than the mean lung stiffness during residual volume (RV)[95].

MRE is a direct measure of lung tissue stiffness and can also resolve spatial and temporal variations in lung stiffness with higher depth and resolution and without risk of radiation exposure.

Biomechanics in Lung Cancer

Lung cancer microenvironment is very complex. Like any tumor, lung cancer TME becomes complex with varying cancer cells, immune cells and stromal cells but also with increase ECM deposition and remodeling by CAFs lead to 1) compressive forces within the stiff center of tumor 3) circumferential tension on the periphery of tumor 2) heterogenous stiffness TME that has high to low varying stiffnesses[33]. And there have been studies done on lung cancer cells that increased solid stress causes increased migration in 2D[34, 35]. However, currently there are not a lot of in-vitro studies that look at dynamics of the lung environment in lung cancer. In addition to the forces that are present in tumor environment, as discussed lung is dynamic organ constantly undergoing inflation and deflation. As a result, the lung cancer will have additional dynamic deformation (i.e. cyclic strain) that they are experiencing. Although the heterogenous changes in mechanical properties (i.e. tissue stiffness) during lung cancer likely lead to spatially heterogenous change in mechanical tension/stretch, previous studies have only investigated the effect of homogenous tension on lung cancer cell dynamics. As a result, it is not known how heterogenous mechanical tension influences cancer cell migration/proliferation or response to therapy.

Concluding Remarks

Lung cancer is complex due to complexity of tumor microenvironment as well as mechanically dynamic lung environment. There are evidences that shows that lung cancer has spatial and temporal heterogeneous mechanical properties. Despite the current progress made in the lung cancer field in trying to understand how stiffness and mechanical strain affect cancer progression, the models that are present in the field still lacks at comprehensively analyzing lung cancer progression under heterogenous mechanical properties. Therefore, this field will benefit from investigation into characterizing heterogeneous mechanical properties of the lung cancer and understanding their role in tumor progression.

Contributions of this Dissertation

This dissertation describes the development and implementation of *in-vitro* and *in-vivo* finite element modeling models to characterize the mechanical properties present within the lung cancer microenvironment. This dissertation also uses this mechanical characterization information to develop novel *in-vitro* systems that better recapitulate the heterogenous mechanical environment that develops during lung cancer and uses these systems to better understand the role of heterogeneity in tumor progression, cancer cell migration and drug resistance. Furthermore, developing new tool of combining MRE and finite element modeling to characterize and quantify heterogenous strain and strain gradient distributions in IPN patients.

Chapter 2 The goal of the study is to develop a novel in-vitro system that better recapitulates the mechanical environment that develops during lung cancer and uses and idealized computational models of lung deformation to develop that in-vitro system. Furthermore, the second goal is to use the in-vitro system to understand how complex heterogenous changes in mechanical strain influence cancer cell migration and response to therapy. The finite element modeling of idealized lung model with tumor showed that there are heterogeneous strains and stresses present – low strain in stiff center of tumor, high strain and strain gradient in the peritumoral region. Using this, we have developed novel *in-vitro* system to generate non-uniform deformation. High strain and strain gradient led to increase in migration and increase in response to drug therapy. Furthermore, we have studied the effect of myoferlin (MYOF) protein as a therapeutic method and found MYOF knock down shows decrease in migration and increase in sensitivity to drug therapy.

Chapter 3 the goal of the study is to integrate these magnetic resonance elastography (MRE) stiffness measurements to into a novel FEM of lung deformation and quantify heterogenous strain and strain gradient distributions. Comparing FEM lung deformation with uniform average stiffness with MRE heterogeneous stiffness models, we have found that although the uniform FEM models was able to capture strain measurement, there was lack of variation in the values and failed to capture the changes in strain gradient within the model. After verifying the importance of heterogeneity in understanding lung deformation, this novel FEM technique to analyze the strain and strain distribution in cystic fibrotic (CF) patients. In CF patients the CF consolidation

areas were stiffer than other part of the lung and showed decrease in strain and smaller variation in strain gradient values.

Chapter 4 the goal of this study was to develop new diagnosing tool using MRE and FEM to investigate mechanical differences between benign and malignant pulmonary nodules. For this study we have recruited indeterminate pulmonary nodule (IPN) patients that have undergone diagnosis of the nodule to quantify heterogenous stiffness, strain and strain gradient distributions in benign and malignant nodules to compare and understand the different spatial gradients in tensile strain. We have seen increased stiffness and low strain and high strain gradient in malignant nodule patients.

Chapter 2. Using Computational and Experimental Tools to Understand How Heterogenous Changes in Lung Cancer Mechanics Influence Cancer Cell Migration and Resistance to Therapy

The results of this study is under manuscript preparation and to be submitted in the *Journal of Biomechanics*, Reference:

Cho, Y., Shukla, V., Englert, J. & Ghadiali, S.N. Understanding the non-uniform deformation in lung cancer migration. *Journal of Biomechanics,* (2021).

Introduction

Lung cancer is leading cause of cancer related death in the United States in both male and females. 80-85% of lung cancers are non-small cell lung cancer (NSCLC). For the stage I, II, IIIA patients, surgical resection is the first line therapy which is often accompanied by adjuvant treatments such as chemotherapy, radiation and/or targeted therapy. However, 40% of the diagnosed patients are at stage IV, and cytotoxic chemotherapy is the first-line therapy[6]. Among NSCLC patients, 64% exhibit driver mutations such as epithelial growth factor receptor (EGFR), anaplastic lymphoma kinase (ALK) and Ras[7]. Patients with identified mutations are often treated with targeted therapies which have shown to improve patient survival in NSCLC[8]. Within NSCLC patients, 10-15% exhibit EGFR mutation, 10-25% Ras mutation and 3-7% ALK mutations[9]. Although EGFR and ALK have established targeted therapies such as erlotinib or gefitinib and crizotinib respectively, patients develop resistance to these targeted therapies due to intrinsic mechanisms (i.e. K-Ras and N-Ras mutations),

secondary point mutations (T790M) or epithelial to mesenchymal transition (EMT) [10, 11, 100]. Although some 3rd generation therapies, including osimertinib, can target these secondary point mutations, drug/chemotherapy resistance continues to be a significant problem in the pulmonary oncology field and there is a clinical need for biomarkers that better predict response to targeted therapies.

Biophysical factors play an important role in tumor development and progression. Increased tissue stiffness promotes tumor growth[101] whereas interstitial flows promotes cell migration and invasion[102]. Importantly, growth induced mechanical stress and the resulting tissue deformation have been shown to alter tumor growth, invasion and metastasis[33, 103, 104]. The lung is one of the most dynamically mechanical organs where non-cancerous alveolar epithelial cells are normally exposed to high levels of mechanical stress (i.e. 15% cyclic strain). In contrast, primary lung tumor cells may experience a 40-fold decrease in this cyclic mechanical stress[91]. However, it is not known how biophysical forces present in lung tumor microenvironment alters oncogenic signaling and/or the response to targeted therapies/chemotherapeutics in NSCLC cells.

Myoferlin (MYOF) is a membrane vesicle trafficking protein. Knocking down MYOF have shown to reverse EMT in highly metastatic MDA-MB231 breast cancer cells and results in significant decrease in migration and invasion[22, 23]. Overexpression of MYOF expression was found in breast cancer which plays important role in controlling EGFR degradation[24]. In lung cancer, increased MYOF expression correlates with worse outcomes[25]. Although there is correlation between lung cancer and MYOF expression,

currently there is limited in understanding of how MYOF alters EMT signaling and cellar biomechanics to alter migratory potential and EGFR expression changes.

Therefore, we hypothesize that mechanical forces in lung tumor environment play a critical role in tumor progression and response to therapeutics. In this study, we will use erlotinib resistant lung cancer cell lines – A549 with K-Ras mutation and H1299 with N-Ras – to1) use computational models to characterize how the local mechanical stress and strain field change as a function of tumor stiffness, 2) develop *in-vitro* models that can capture these changes in strain field and investigate how they influence A549 and H1299 migration/proliferation and drug resistance and then 3) investigate how silencing MYOF influences migration/proliferation and drug resistance

Methods

Computational Modeling

A finite element (FE) model of the lung was generated using the COMSOL Multiphysics software package. The adult lung geometry was generated by importing Chia Shiang Lin's 3D CAD model for Solidworks (uploaded in June, 2014, www.3dcadbrowser.com/) to COMSOL. The normal lung tissue was modeled as a homogeneous, compressible Neo-Hookean hyperelastic material[82].The time-dependent equations governing tissue deformation solved in COMSOL were

$$\rho \frac{\partial^2 \boldsymbol{u}}{\partial t^2} = \nabla \cdot (FS)^T \quad F = I + \nabla \boldsymbol{u} \quad S = \frac{\partial W}{\partial \epsilon} \quad \varepsilon = \frac{1}{2}(F^T F - I) \tag{1}$$

where ρ is tissue density, **u** is the displacement field, *F* is the deformation gradient, *I* is the identity tensor, *S* is the second Piola-Kirchhoff stress tensor, *W* is the strain energy density and ε is the strain tensor. We implemented following for Neo-Hookean hyperelastic material properties

$$W = \frac{1}{2}\mu(I_1 - 3) - \mu \ln(J_{el}) + \frac{1}{2}\lambda(\ln(J_{el}))^2 \tag{2}$$

Here, I_1 is the first invariants of the isochoric elastic right Cauchy-Green tensor, *J* is the elastic volume ratio with an equivalent Young's modulus (E) of 6 kPa, poisson's ratio (ν) of 0.2 with Lamé parameters λ and μ were as follows:

$$\lambda = \frac{E}{3(1-2\nu)} \quad (3) \qquad \mu = \frac{E}{2(1+\nu)} \quad (4)$$

The tumor with diameter of 1cm was placed within the lung with varying stiffness of 3 to 36 kPa. The spherical tumor modeled as linear, elastic, isotropic material as follows:

$$\rho \frac{\partial^2 \boldsymbol{u}}{\partial t^2} = \nabla \cdot (FS)^T \quad F = I + \nabla \boldsymbol{u} \quad \varepsilon = \frac{1}{2}(F^T F - I) \tag{5}$$

Intercostal area was fixed with fixed constraint and the cyclic pressure were loaded on the outer wall of the lungs (Figure 9 A). Negative sinusoidal pressure breathing was simulated with breathing frequency of 0.2 Hz. Physics-controlled normal element size mesh was generated (Figure 9 B).

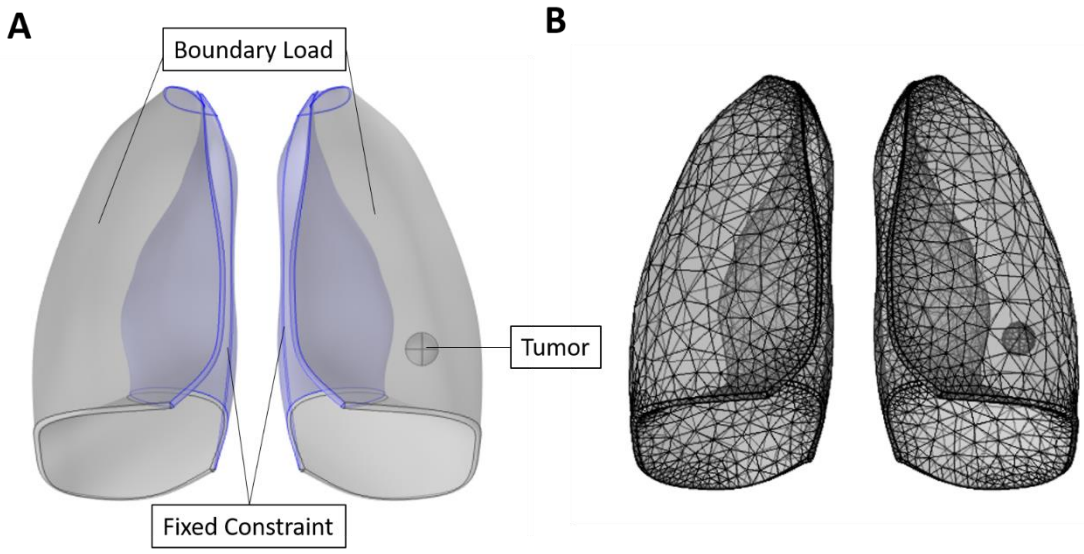

Figure 9. COMSOL idealized lung model set up. A) shows geometry and boundary conditions of the model B) shows mesh of the model

Cell culture

Human lung adenocarcinoma cell lines, A549 (ATCC® CCL-185™) and NCI-H1299 (ATCC® CRL-5803™), were used for the following studies. A549 cells were maintained in Dulbecco's Modified Eagle's Medium (DMEM) supplemented with 10% Fetal Bovine serum (FBS) and 1% antibiotic-antimycotic. NCI-H1299 cells were maintained in Roswell Park Memorial Institute (RPMI) 1640 medium supplemented with 10% Fetal Bovine serum (FBS) and 1% antibiotic-antimycotic. Knocking down MYOF expression on A549 and H1299 were performed with Lipofectamine 2000 using siRNA sequence (CCTCTACTCTTTGCCGAACTA, Sigma-Aldrich). In order to confirm transfection success, cells were also transfected with fluorescently tagged negative control siRNA (SCI001, Sigma-Aldrich) as shown in Figure 10.

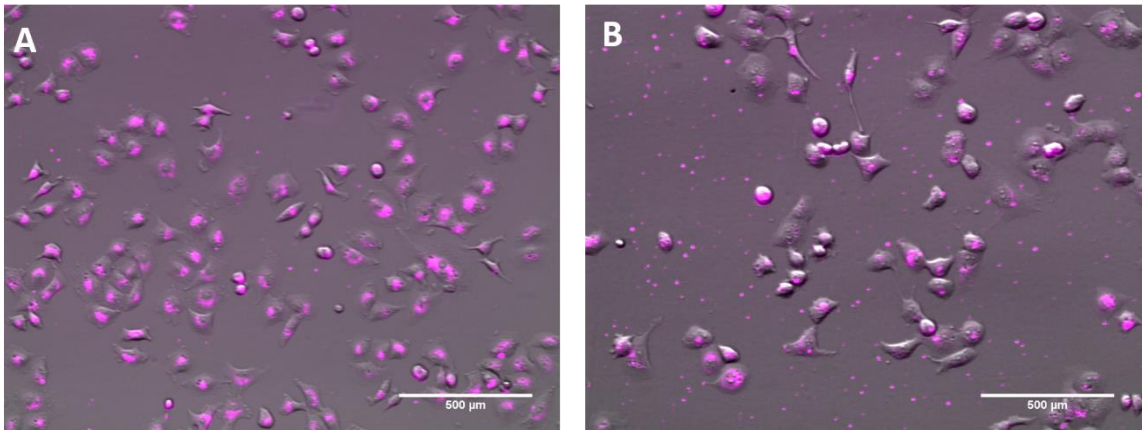

Figure 10. Florescence image of negative control siRNA A) A549 scramble negative control B) H1299 scramble negative control.

Stretching

Cells were seeded on ProNectin coated Bioflex culture plates (Flexcell) overnight. Once the cells were properly attached and seeded onto the plates, Flexcell® Tension Systems were used to stretch the plate membrane. Loading posts were placed beneath the membrane to ensure equibiaxial strain. Oscillatory stretch was implemented and applied an equibiaxial strain magnitude of 0-18% for the frequency of 0.2 Hz for 24hrs (Figure 11).

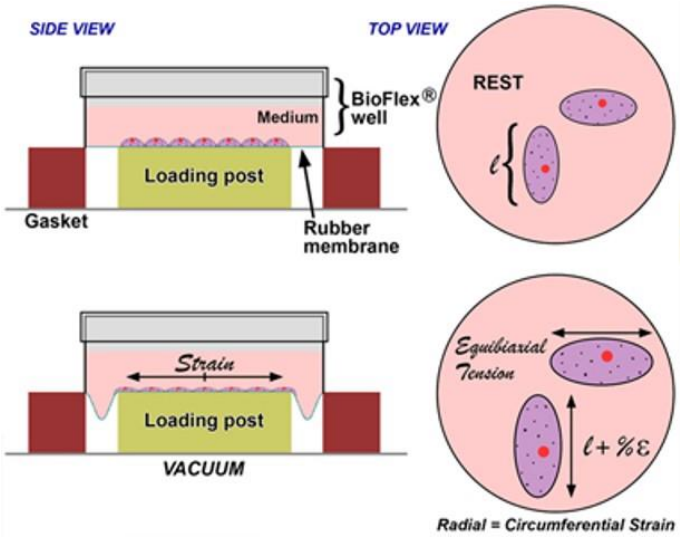

Figure 11. Schematic of Bioflex Flexcell® Tension Systems. Monolayer of cells seeded on the membrane. The vacuum pulls down on the membrane against the loading post, exerting equibiaxial strain on the cells. Adapted from http://www.flexcellint.com.

For non-uniform strain, a 12mm diameter circular glass coverslip was glued onto the bottom of the flexcell membrane with a silicone sealant (Figure 12 A). Oscillatory stretch was applied over a range of equibiaxial strain magnitudes 0-18% with a frequency of 0.2 Hz for 24hrs. In order to confirm the non-uniform strain, 2mm x 2mm dot grid was marked on Flexcell membrane (Figure 12 B). Before and after stretch image of the grid

was imported into MatLab. Custom written MatLab code that uses nearest neighbor algorithm was used to find neighboring dots and displacement between each dots were calculated for the whole grid. The following strain tensor (ε) equation was used in cylindrical coordinates to calculate the strain field:

$$\varepsilon = \frac{1}{2}[\nabla\vec{u} + (\nabla\vec{u})^T] \quad (6)\,, \qquad \frac{\partial u_r}{\partial r} = \sqrt{\left(\frac{\partial u_x}{\partial x}\right)^2 + \left(\frac{\partial u_y}{\partial y}\right)^2} \quad (7)$$

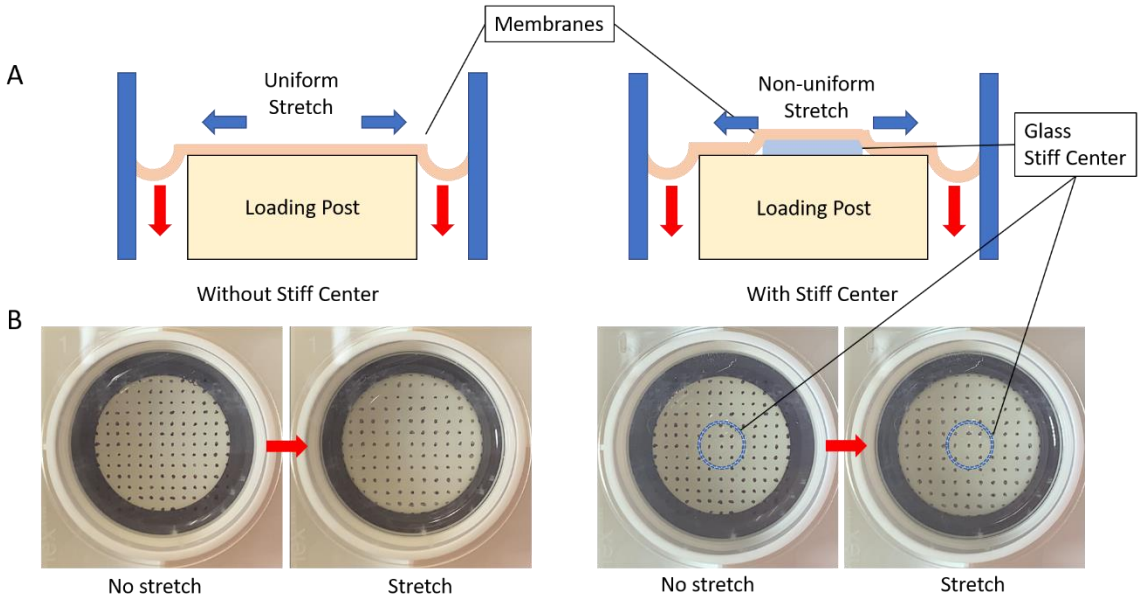

Figure 12. Non-uniform deformation system setup. A) schematic of the vacuum stretch (red arrows) pulling down on the Flexcell membrane with or without glass stiff center. B) shows representative images of the 16% cyclic strain with or without stiff center.

Cell Cluster Migration

Cells were seeded in clusters to be able to track migration dynamics over a 24 hour time period. A 10 µL droplet of cell clusters with a concentration of 2,000 cells/ µL were seeded on the ProNectin coated Bioflex culture plates (Flexcell) overnight. Once the monolayer of clusters were formed, the wells were flooded with respective media and 0 hr time point phase contrast images of the clusters were taken using an Olympus IX81 inverted microscope (Olympus Corporation, Tokyo, Japan). After the clusters were exposed to oscillatory stretch as described above, the 24hr time point phase contrast images of the were taken. The NIH image processing software ImageJ was used to manually trace the outline of the clusters to measure area (A) and perimeter (P) for both 0 and 24hr time point images. Relative area change was calculated as

$$A_{rel} = {(A_{t=24hr} - A_{t=0hr})}/{A_{t=0hr}} \tag{8}$$

and used to measure the migration of the clusters. Furthermore, the circularity (C) of the clusters were calculated as $C = {4\pi A}/{P^2}$ to measure the invasive potential of the clusters. Similar to relative area change, relative circularity change was calculated as

$$C_{rel} = {C_{t=24hr} - C_{t=0hr}}/{C_{t=0hr}}. \tag{9}$$

Live-Cell Migration Assay

A wound assay was performed on transfected A549 and H1299 cells. Cell suspensions of 400 cell/µL were seeded at 50 µL in each chambers of a wound assay insert (Ibidi®, Martinsried, Germany) which allow formation of well-defined "wound edge" (Figure 13). Once the monolayer of cells is formed within the inserts, the inserts are removed and placed on the live-cell imaging system to track cell migration patterns in real time. Phase contrast images were taken by Zeiss Axiovert 200M microscope, every 5 minutes over a time period of 24 hrs. From each image 30 individual cells migratory trajectory were traced using ImageJ. Ibidi Chemotaxis and Migration Tool (Ibidi.com/software/chemotaxis_and_migration_tool).For each data point, the total distance traveled and average velocity were analyzed to access the migration. Following equation was used to calculate velocity (v):

$$v = \frac{1}{n}\sum_{j=1}^{n}\left[\frac{1}{m}\sum_{i=1}^{m}\frac{d_{i+1}^{j}-d_{i}^{j}}{\Delta t}\right] \quad (10)$$

where n is the total number of cells per experiment (approximately 30 cells), m is the number of time intervals for each cell (for these sets of experiments, it was 289 time interval over the period of 24hrs). j is the specific cell, i is timepoint. Therefore d_i^j represents cell j at timepoint i.

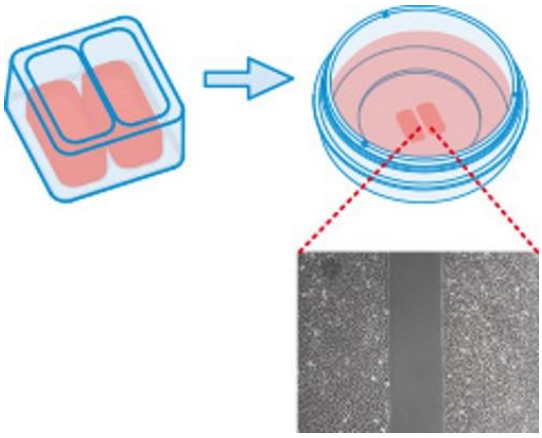

Figure 13. Schematic of Ibidi® wound assay insert and setup. Once the cells are seeded the inserts are lifted, and the wound edge is formed as shows. Adapted from www.ibidi.com.

Erlotinib and IC_{50} Study

Erlotinib hydrochloride (Sigma-Aldrich, cat#: SML2156) was used for the drug resistance study. To determine the appropriate concentration of the Erlotinib for each cell type, half maximal inhibitory concentration (IC_{50}) studies were conducted. IC_{50} is a quantitative measure of how much drug is needed to inhibit the proliferation cells by 50%. The cells were cultured and exposed to different magnitude of strain 0-15% cyclic strain over 72hrs with Erlotinib concentrations 0-20 µM. To measure the proliferation of the cells, Vybrant MTT cell proliferation assay was used to quantify cell proliferation. IC50 values were calculated by plotting logarithmic values of concentration of Erlotinib against the proliferation. Using the graph, we calculated the Erlotinib concentration at 50% proliferation. For the migration studies using Erlotinib, the 5 times and 10 times less the concentration IC_{50} for controls were used.

Western Blot Analysis

Expressions of EGFR, MYOF, EMT markers (E-cadherin, vimentin) were analyzed via western blot. Cells were seeded and exposed to 0-8% cyclic strain for 48hrs and sample were collected and prepared. After measuring the protein content using BCA assay, the samples were diluted to achieve 30µg total protein for each sample. Loading buffer (0.3M Tris-HCL-pH6.8, 25% glycerol, 10% SDS, 5% β-mercaptoethanol and 0.1% bromophenol blue) was added and loaded onto pre-cast 4-12% Bis-Trist gels from NuPAGE Novex along with Precision Plus Protein Kaleidoscope Standards (Bio-Rad, Hercules CA). Gels were run using an electrophoresis system (Invitrogen, Grand Island NY). Once gels were done running, pure Nitrocellulose Membranes (0.45µm) (Bio-Rad, Hercules CA) was used for transfer of the gels. The transferred membranes were then blocked with 5% milk in 1x tris buffered saline (TBS) with 0.1% Tween-20 (GE Healthcare, Piscataway NJ). Membranes were probed for EGFR antibody (4267, Cell Signaling Technology, 1:1,000 dilution), MYOF antibody (MABT828, Sigma Aldrich, 1:1,000 dilution), E-cadherin (EP700Y, Abcam, 1:500 dilution), vimentin (V6630, Sigma-Aldrich, 1:1,000 dilution) and as control anti-β-Actin antibody (A5316, Sigma, 1:5000 dilution).

Immunostaining

The cells were fixed with 4% paraformaldehyde and permeabilized with 0.1% Triton-X 100 in PBS. The EGFR antibody (4267, Cell Signaling Technology, 1:200 dilution) was used and incubated at room temperature for 90 minutes. Secondary

antibody anti-mouse IgG were diluted in PBS at 1:500 dilution and 4',6-diamidino-2-phenylindole (DAPI) (1:5,000) for nuclear counterstain. The images were taking using Zeiss Axiovert 200M microscope.

Statistical analysis

GraphPad Prism 9 (GraphPad Software, San Diego, CA USA) was used for statistical analysis. Normality and outliers were tested for each data set using Shapiro-Wilk test at $\alpha = 0.05$. The outliers were removed from the dataset by using ROUT at Q=5%. One-way ANOVA was performed detect statistical difference with $p \leq 0.05$.

Results

Idealized Computational Modeling

The idealized FEM model of lung inflation/deflation with an imbedded tumor that is stiffer than the surrounding tissue is shown in Figure 9A. This model indicates that the presence of a stiff tumor may dramatically alters the strain and strain gradient values within and surrounding the tumor. As shown in Figure 14, we first determined how changes in tumor stiffness (Young's modulus) influences the Von Misses stress within a cross-section of the lung. The Von Misses stress is a measure of tensile force per unit area and results indicate that under normal tidal respiration, this stress varies from 0 to 75 N/m^2 with an average value of 38 N/m^2. However, when the tumor has a low stiffness 3kPa, Von Misses stress within the tumor had average stress of 50 N/m^2. In addition, as the stiffness of tumor increases, the average Von Misses tensile stress within the tumor also increases to 100 N/m^2 when the tumor is very stiff, i.e. 36kPa. The region between the tumor and the normal lung, peritumoral region (blue highlighted region), exhibited significant spatial gradients in the stress field with spike increases that go up to 450 N/m^2 and drops down to normal stress values. The representative images show that for low tumor stiffness (Figure 14B) shows more directional stress in the direction of lung expansion whereas the tumor with high stiffness (Figure 14C) shows the disruption in the stress direction where we see normal forces pointing to the apex of the lung.

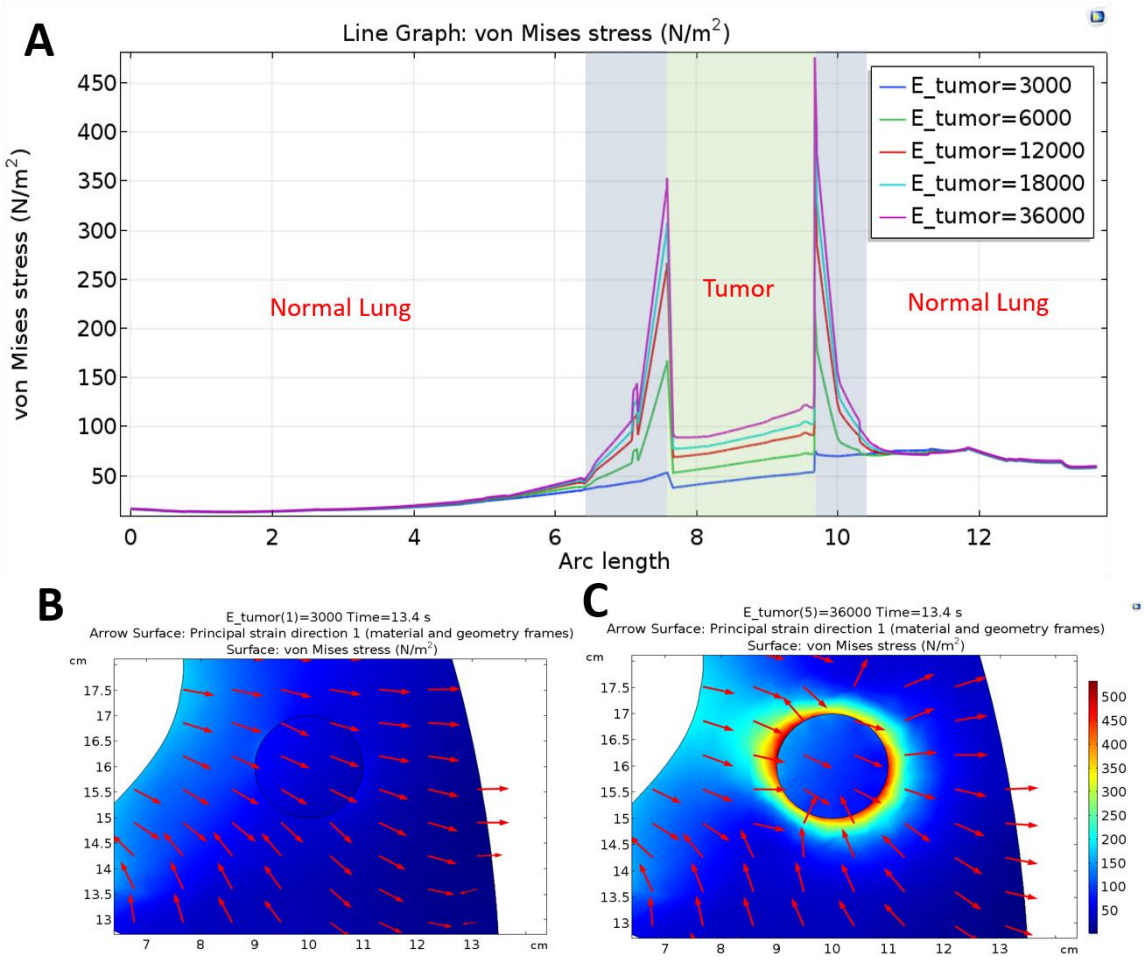

Figure 14. von mises stress in the tumor region in idealized lung model. A) The graph shows the stress cross section of the lung in normal (white) and tumor (green) region with varying tumor stiffness from 3 to 36 kPa. The bottom two images show representative images of B) low tumor stiffness of 3 kPa and of C) high tumor stiffness of 36 kPa.

As shown in Figure 15, the model also indicates that changes in tumor stiffness alters the tensile strain within a cross sectional area of the lung. Here, we plot 1st principle strain which is the strain in a plane normal to a plane in which the shear strain is zero. The 1st principle strain is related to the maximum tensile strain in the system. The strain values show that although the normal lung experiences about 6% tensile strain, these strain values deviate from this baseline significantly in the region near the tumor

(indicated by green highlighted region) as is a function of tumor stiffness. The higher the tumor stiffness, the lower the values of the strains within the tumor region. However, the most interesting part of the strain graph was that in the peritumoral region (highlighted by blue) there is a sharp increase strain over the 6% baseline value and there are very high spatial gradients in strain in the peritumoral region. As result, this idealized computational model of lung deformation during tidal ventilation indicates that the development of a stiff tumor region leads to a highly heterogenous stress and strain field. Although previous investigators have investigated how homogenous changes in tensile strain influence cancer cell migration[72, 105], to our knowledge no previous studies have investigated how heterogeneous strain fields as demonstrated by the computational model influence cancer cell migration. Therefore, the remainder of this chapter seeks to develop a novel in-vitro system that recapitulates the heterogenous strain field predicted by the computational models. Specifically, we seek to develop an in-vitro model that simulates the stiff tumor region and generate significant spatial gradients in tensile strain.

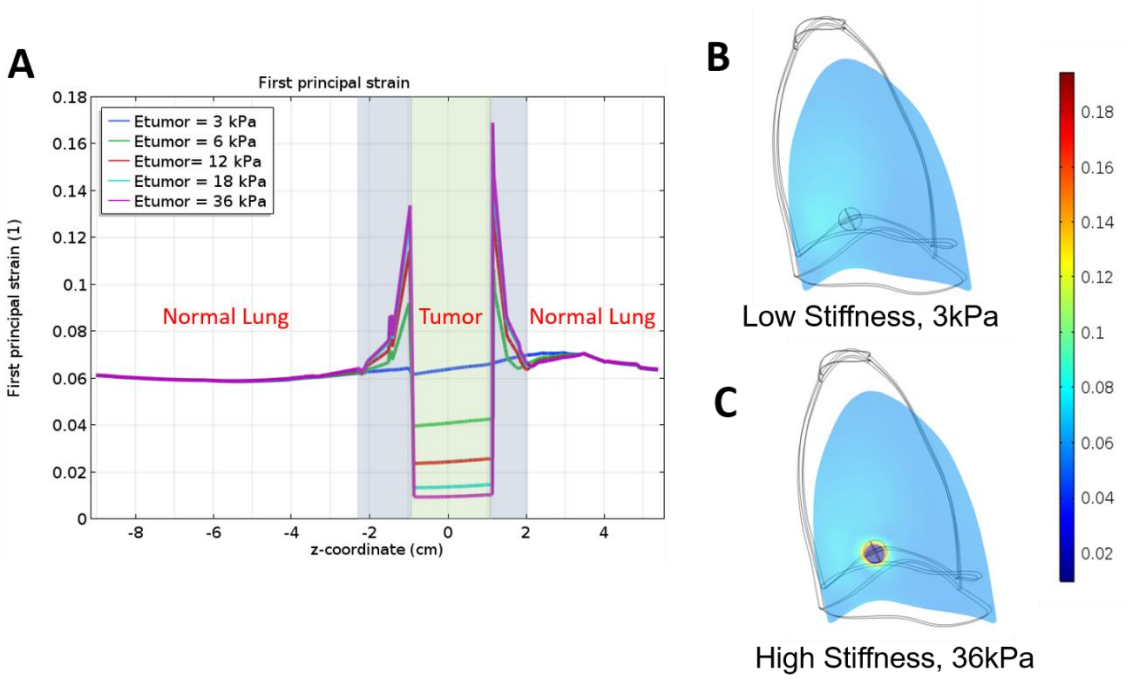

Figure 15. Idealized lung model showing A) the strain values in the cross-sectional area showing normal (white) and tumor region (green). Right images show representative image of strain of tumors at B) low stiffness, 3kPa and at C) high stiffness, 36 kPa.

Effect of Uniform Strain on Lung Cancer Cell Migration

Before investigating the effect of heterogenous strain on cancer cell migration, we used established platforms (i.e. the Flexercell Tension system) to investigate how the low strains that develop within the tumor and the high strains that develop in the peritumoral region influence lung cancer migration and proliferation. Figure 16A,B shows the effect of 0% cyclic strain (control) and uniform cyclic deformation of 8% and 18% cyclic strain on migration and circularity for A549 and H1299 cells. A549 cells shows significant increase in migration with increase in cyclic strain magnitude (Figure 16A). This indicates that for A549 increase in cyclic strain in the peritumoral region may stimulate

increased migratory and invasive potential. Figure 16C shows representative image for A549. H1299 cells on the other hand showed no significant change in migration size with 8% cyclic strain and significant decrease in migration for 18% cyclic strain (Figure 16B). For changes in circularity, the 18% cyclic strain had significant decrease in circularity in H1299. This indicates although the cyclic strain may decrease the motility of the cells, they increase the invasive potential at high strain 18% cyclic strain.

To investigate if the relative changes in cell cluster size is due to increases in cell proliferation, MTT proliferation assays were conducted on A549 and H1299 after 24 hours of 8% and 18% cyclic strain. Figure 16D shows that although there is a significant decrease in proliferation between 8% and 18% cyclic strain in A549, there is no other significant changes in proliferation. This demonstrates the increase in migration cluster size shown in Figure 16A,B are not due to increase in proliferation.

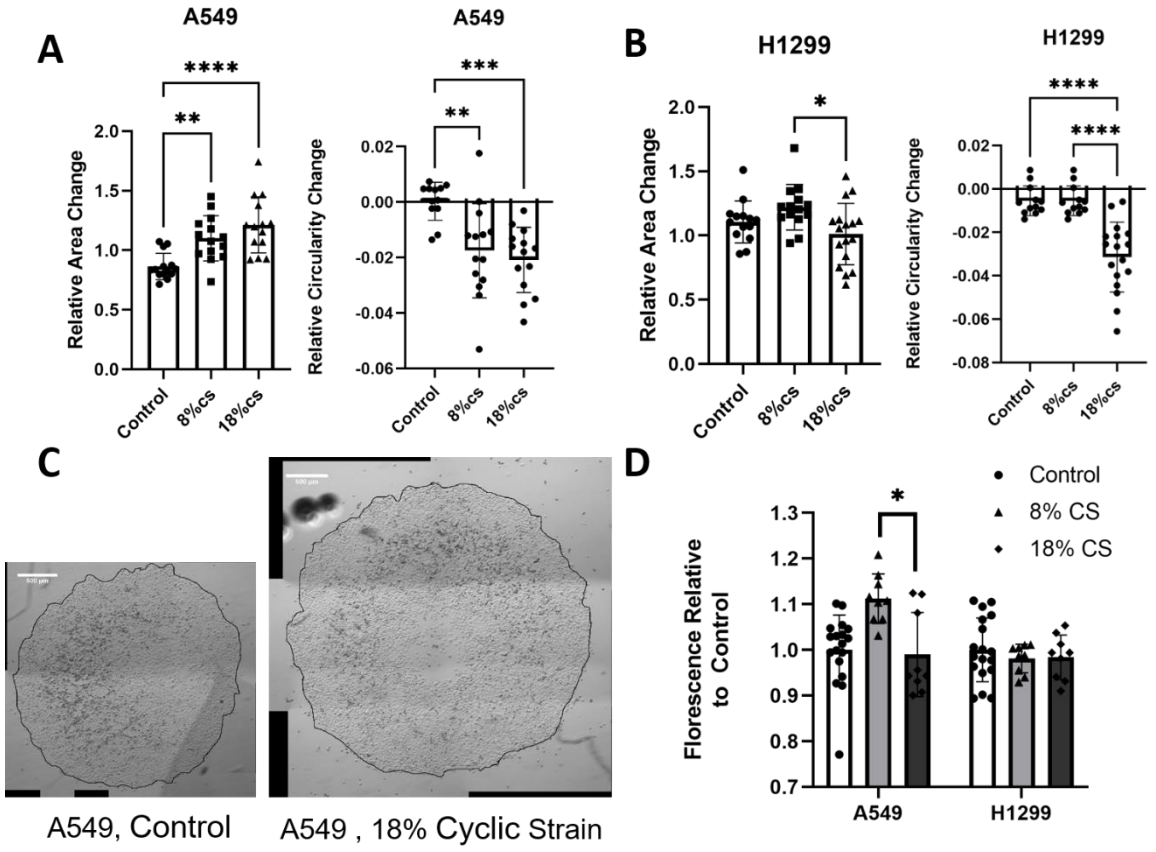

Figure 16. Study of uniform cyclic strain of 8% and 18% on migration and proliferation after 24hrs on A549 and H1299. A) Relative area change and circularity change in A549. Shows significant increase in migration and changes in circularity with 8% and 18% cyclic strain. B) Relative area change and circularity change in H1299. Significant decrease in migration and significant changes in circularity with 18% cyclic strain. C) shows representative image of cluster migration for A549. D) proliferation analysis on A549 and H1299 under 8% and 18% cyclic strain. Significant decrease in proliferation with 18% cyclic strain for A549 otherwise not significantly different. (n=14, * $p<0.05$, ** $p<0.01$, *** $p<0.001$, **** $p<0.0001$ by one-way ANOVA)

Generating Non-Uniform Deformation Strain Field

To simulate the increased stiffness with the tumor region, a glass coverslip was glued to the center of a flexcell membrane prior to the application of vacuum pressure.

As shown schematically in Figure 12A, without the glass coverslip, the membrane will theoretically deformation uniformly in the radial direction to generate a homogenous tensile strain field. However, with the glass coverslip, which is significantly less deformable, the application of vacuum pressure will theoretical generate large radial strains near the periphery of the well and very low strains in the coverslip region and thus a large spatial gradient in tensile strain. To confirm these theoretical predictions and to characterize the generated strain fields both with and without glass coverslips, a 2mm x 2mm dot grid was marked on Flexcell membrane (Figure 12 B) and displacement of the dots during the application of vacuum pressure was monitored and converted into a radial strain field as described in the Methods section. As shown in Figure 17 A,B the non-glass coverslip system shows the expected uniform strain of ~8% (Figure 17 A) and is consistent with the setting used in the flexcell program. However, the inclusion of a stiff center leads to a highly non-uniform strain field. Specifically, application of vacuum pressure that would normal produce a uniform 8% oscillatory strain field, led to a strain field in which there is very low strain in the glass coverslip region (~1%) and a gradual increase in the strain from the stiff center to outer area to reach ~8% strain (Figure 17 B). Similar homongenous and heterogenous strain field patterns were observed when the vacuum pressure was increase to producing 16% uniform strain when there is no stiff center (Figure 17 C) whereas with stiff center there is gradual increase in the strain from the stiff center to outer area to reach ~14% strain on the outer edge (Figure 17 D). It is important to note that under 16% stretch conditions, the stiff center generates higher gradient of non-uniform deformation. We also note that lower strains at the edge of the

map under 16% strain is due to edge effects associated with the movement of dots at the edge out of the field of view and are therefore consider to be measurement artifacts.

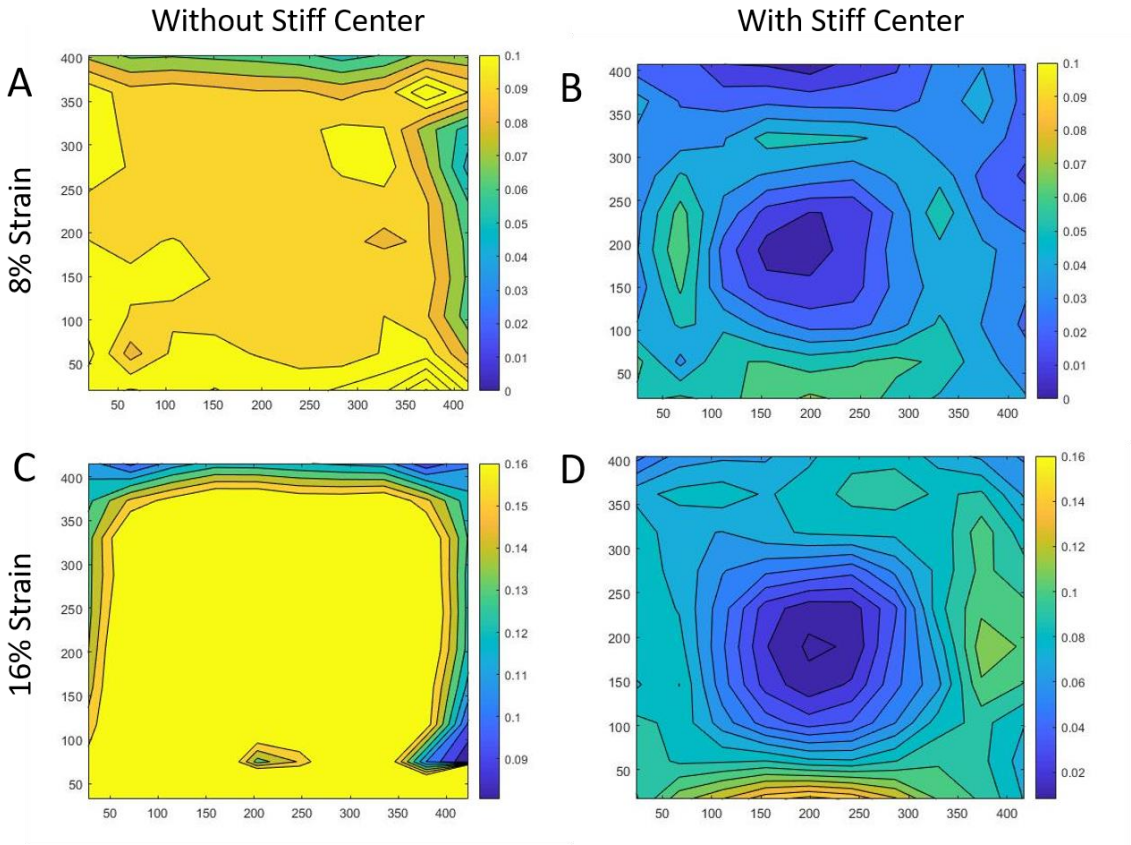

Figure 17. The top most image shows the setup of vacuum stretch (red arrows) pulling down on the Flexcell membrane with or without stiff center. Non-uniform strain deformation generated with glass coverslips. Left two images show without stiff center and right two images are with stiff center. Top two images are with 8% oscillatory strain and bottom two are with 16% oscillatory strain.

Effect of Non-uniform Deformation on Lung Cancer Cell Migration

To analyze the effect of strain gradient on the cluster migration, the clusters of cells for A549 and H1299 were seeded inside, middle (on the edge of stiff center), and

outside of stiff center as shown in Figure 18. After 24 hrs of migration we see that for 8% cyclic strain, there was significant increase in migration for A549 with clusters seeded on the middle (edge) and outside of the stiff center (Figure 19 A) but there was no significant different in circularity (Figure 19 B). This demonstrates that under low gradient cyclic strain (8%) there is increase in migratory potential (increase in cluster size) with increasing strain but cells lack invasive potential (no changes in circularity). Under 16% cyclic strain after 24 hrs we see only significant increase in migration for the outer clusters (Figure 19 C) whereas there was significant change in circularity with middle and outer clusters (Figure 19 D). Under high gradient cyclic strain (16%), there is higher gradient of strain. The cells only showed migratory potential at maximum strain on the cluster on the outside of the stiff center which showed increased cluster size but increase in strain gradient showed increase in invasive potential (decrease in circularity).

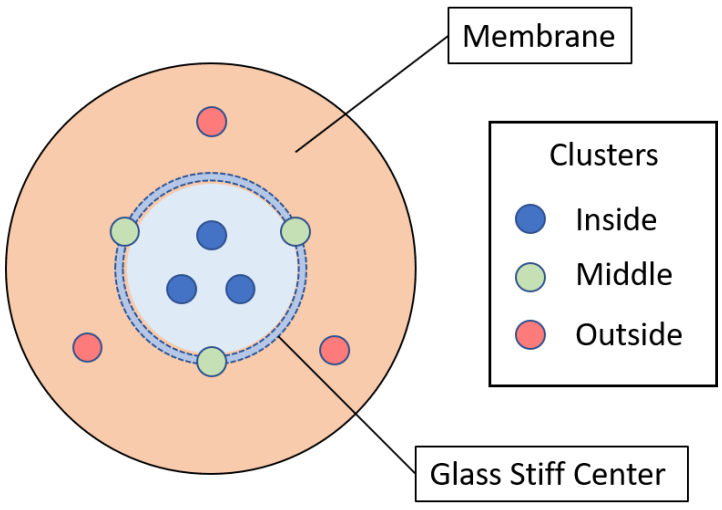

Figure 18. Schematic of non-uniform strain migration study. The clusters of cells (A549 or H1299) were seeded inside (blue dots), middle (green dots), and outside (red dots) of the glass stiff center on membrane.

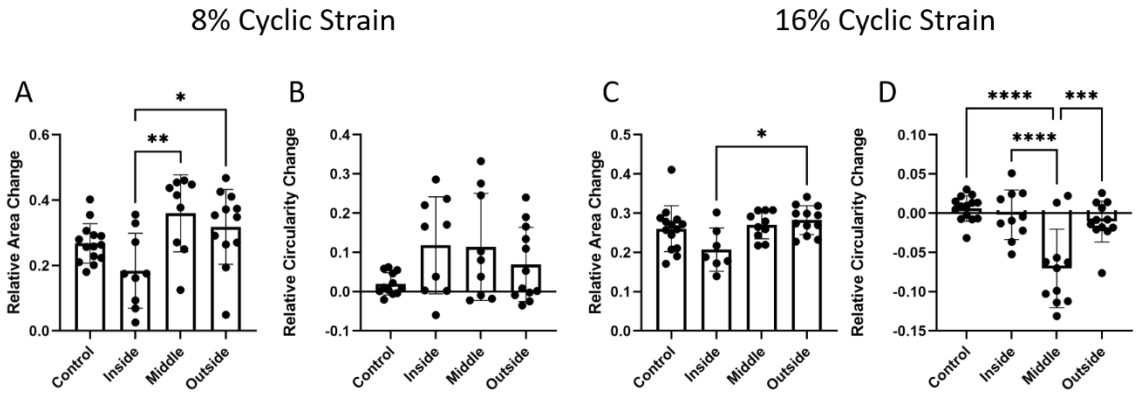

Figure 19. Effect of strain gradient on migration for A549 after 24hrs. Control for each experiment were cells that were not exposed to any strain – 0%. A) relative size change under 8% cyclic strain gradient. Significant increase in size change in clusters middle and outside B) relative circularity change under 8% cyclic strain gradient. No significant change. C) relative size change under 8% cyclic strain gradient. There is significant increase in migration for outer clusters. D) relative circularity change under 8% cyclic strain gradient shows significant changes in circularity in middle and outside clusters. (n=12, * $p<0.05$, ** $p<0.01$, *** $p<0.001$, **** $p<0.0001$ by one-way ANOVA)

The H1299 showed different migration patterns under similar conditions (Figure 20). After 24 hrs of migration we see that for 8% cyclic strain, there was no significant increase in area change (Figure 20 A) but there was significant change in circularity for clusters seeded on the outside of the stiff center (Figure 20 B). This demonstrates that under low gradient cyclic strain (8%) there is increase in invasive potential for clusters exposed to highest strain. Under 16% cyclic strain after 24 hrs we see only significant decrease in migration for clusters in the stiff center (Figure 20 C) whereas there was significant change in circularity with the outer clusters (Figure 20 D). For H1299, the cells do not show as much migratory potential with increase in strain but at high strain gradient they show increase in invasive potential.

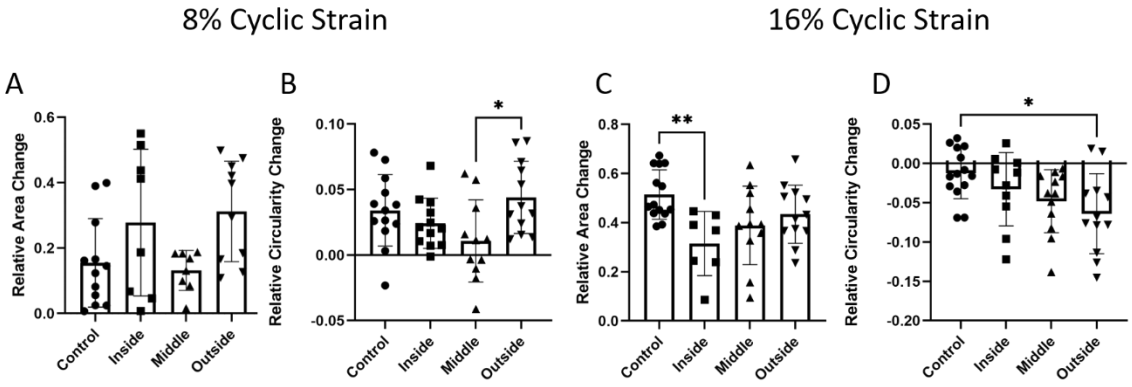

Figure 20. Effect of strain gradient on migration for H1299 after 24hrs. Control for each experiment were cells that were not exposed to any strain – 0%. A) relative size change under 8% cyclic strain gradient. No significant change. B) relative circularity changes under 8% cyclic strain gradient. Significant changes in circularity for outer clusters. C) relative size change under 8% cyclic strain gradient. There is significant decrease in migration for inner clusters. D) relative circularity change under 8% cyclic strain gradient shows significant changes in circularity in outside clusters. (n=12, * $p<0.05$, ** $p<0.01$ by one-way ANOVA)

Effect of Uniform Strain on Lung Cancer Cell Drug Resistance

In addition to cancer cell migration, we also explored how exposure to cyclic tensile strain may alter the sensitivity of lung cancer cells to targeted pharmaceuticals/drug treatment. We specifically investigate how cyclic tensile strain altered the IC_{50} of A549 and H1299 cells during Erlotinib treatment. The IC_{50} of the A549 without strains is 7.32 µM and H1299 without strain is 12.27 µM. Figure 21A shows that with increase in cyclic strain, there is significant decrease in the IC_{50} concentration for both A549 and H1299. Decrease in IC_{50} means that the cells are becoming more sensitive to the drug treatment. Expression of EGFR was quantified using western blot to understand why cyclic strain might be making the cells more sensitive to

Erlotinib. We observed an increase in EGFR expression with increasing cyclic strain as shown in Figure 21 B. The immunostaining was done to probe for EGFR localization changes with cyclic strain as shown in Figure 21C. The immunostaining shows that without cyclic strain the EGFR expression is more localized to the cell membrane where we see increased florescence in the periphery of the cells. With 18% cyclic strain there is more increased localization of EGFR to cytoplasm area of the cells where we see increased florescence within the cells. Localization of EGFR in cytoplasm may indicate that there is decrease in EGFR recycling where the receptors end up in endosomes within the cytoplasm. Furthermore, the cluster migration studies under cyclic strain were repeated with addition of 5x and 10x less of IC_{50} concentration. Figure 21D although 8% cyclic tensile strain increased cell migration and cluster size, 5x and 10x Erlotinib IC_{50} treatment was effective at preventing this increase in cell migration.

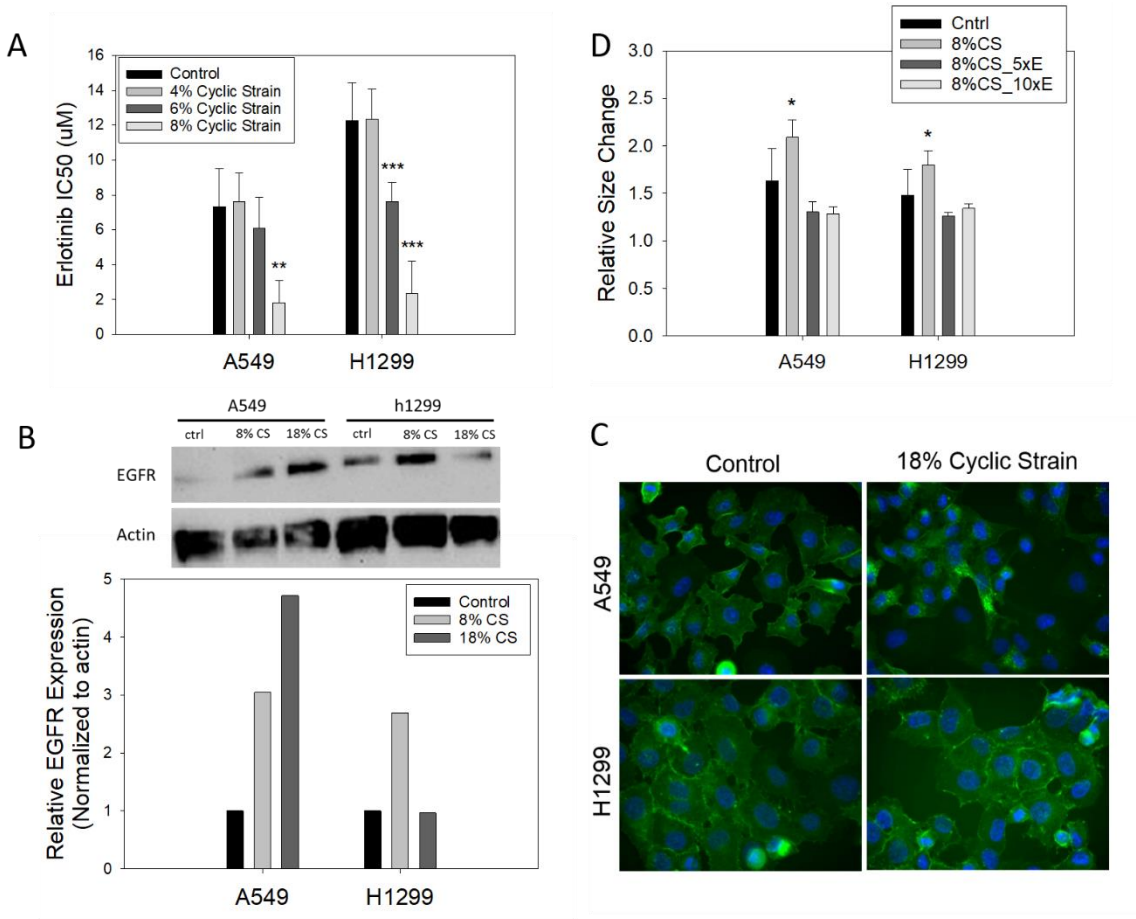

Figure 21. Effect of uniform cyclic strain on Erlotinib A) IC_{50} study under 0-8% cyclic strain shows significant decrease in IC_{50} concentration with increase in strain. B) western blot analysis shows increase in EGFR expression with increase in strain C) immunostaining for EGFR with control (no stretch) and 18% cyclic strain. At high cyclic strain, the EGFR are more localized in the cytoplasm. D) migration study shows significant increase with cyclic strain that is inhibited by addition of Erlotinib. (n=6, * $p<0.05$, ** $p<0.01$, *** $p<0.001$ by one-way ANOVA)

Effect of Myoferlin (MYOF) on Lung Cancer Cell Migration

Although it is clear that mechanical factors such as cyclic tensile strain can alter lung cancer cell migration and resistance to therapy, we also sought to determine how novel treatment that alter cellular biomechanics may alter lung cancer cell migration and

resistance to therapy. Specifically, previous investigators have demonstrated that silencing a membrane repair protein known as Myoferlin (MYOF) alters the biomechanical properties of breast cancer cells and results in a significant change in triple negative breast cancer cell migration. Here, we sought to determine if silencing MYOF can also alter lung cancer cell migration. We first determine the effectiveness of the knocking down Myoferlin (MYOF) expression in A549 and H1299 using standard western blot techniques and specifically probed for both MYOF expression level as well as epithelial-to-mesenchymal marker (EMT) E-cadherin. As shown in Figure 22, there is no changes in MYOF expression in negative controls (A549/H1299 scrambles) but we see about 2-fold decrease in MYOF expression with si-RNA MYOF (siMYOF). Furthermore, we see marked increase in E-cadherin for siMYOF.

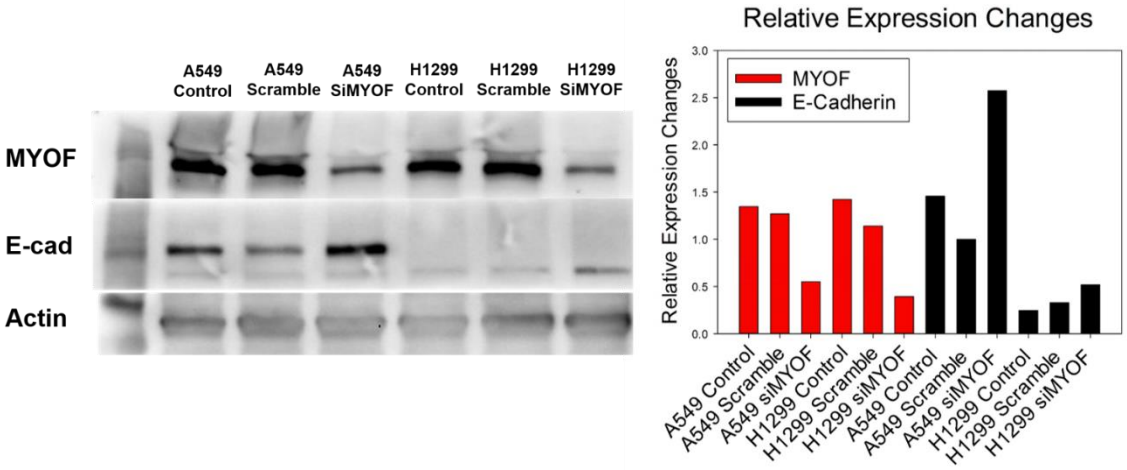

Figure 22. Western Blot analysis of myoferlin (MYOF), and E-Cadherin expression on control, scramble, siMYOF A549 and H1299 cells. There is a significant decrease in MYOF expression with siRNA knockdown which resulted in two-fold increase in E-Cadherin levels.

Once the effectiveness of siRNA MYOF transfection has been confirmed the cells were used to study effect of MYOF on migration for A549 and H1299. The Ibidi wound scratch assays were performed and individual cells were tracked over 24 hr period. Figure 23 A, B shows that both A549 and H1299 with MYOF expression knocked down there is significant decrease in distance that they traveled and velocity. The representative image of the cell tracks (Figure 23 C) show that H1299 control has wider range of movements compared to H1299 siMYOF tracks that show reduced range of cell tracks. This confirms that in lung cancer cells MYOF protein plays important function in migration of the cells.

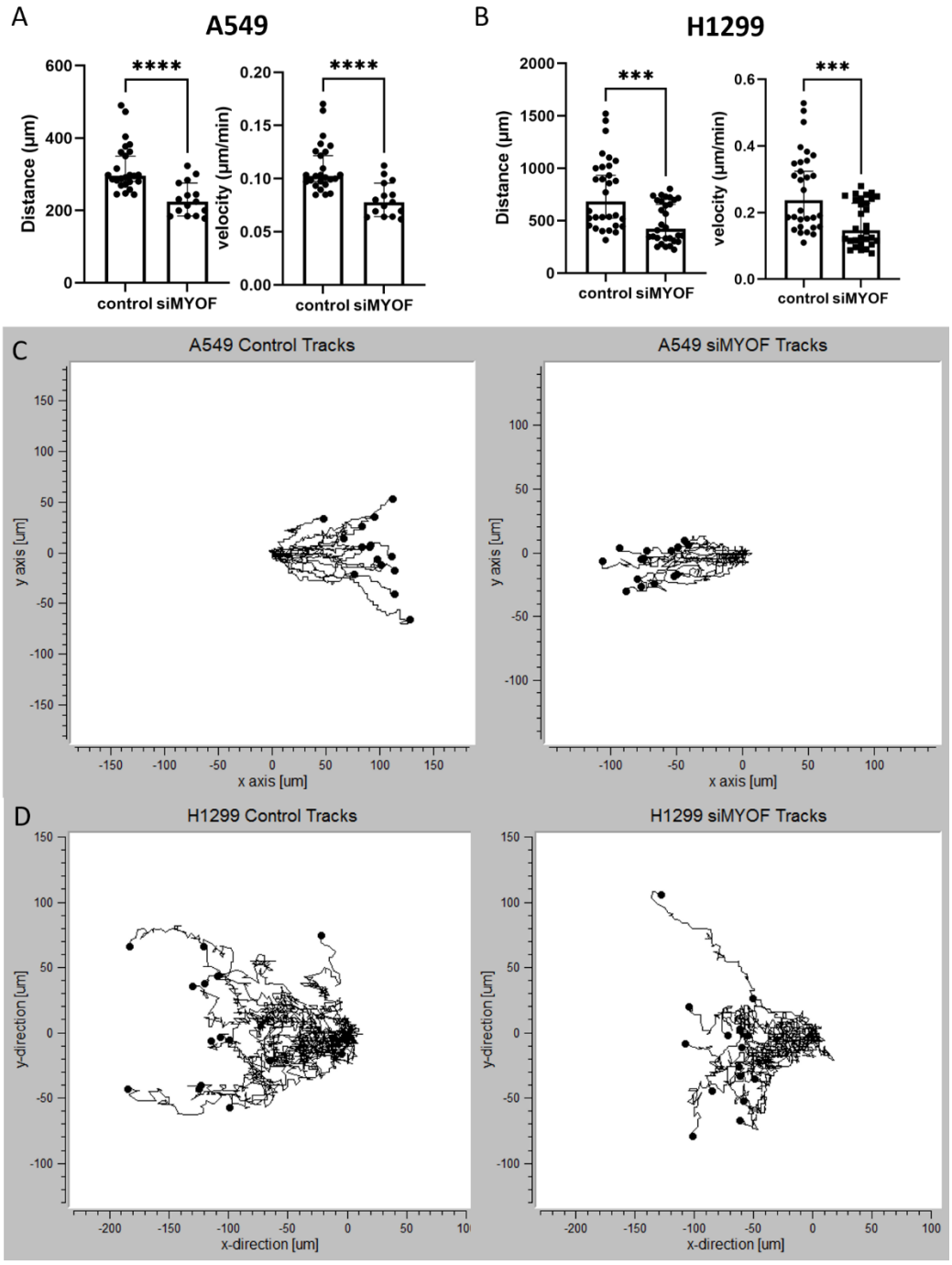

Figure 23. Migration distance and velocity for n = 30 control and siMYOF A) A549 and B) H1299 cells. There is significant decrease in migration distance and velocity with MYOF expression knockdown. C) These are representative images of the individual cell tracking for A549 control and siMYOF. D) These are representative images of the individual cell tracking for H1299 control and siMYOF. (n=30, *** $p<0.001$, **** $p<0.0001$ by t-test)

Effect of MYOF on Erlotinib Resistance

In addition to migration, we also sought to determine if siliencing MYOF alters resistance to erlotinib therapy. As confirmation of the previous erlotinib studies done in cyclic strain studies, the erlotinib IC_{50} of the A549 and H1299 controls were caculated in the separate experiment. For this A549 control is 6.76 µM and H1299 control is 14.00 µM which is similar to IC_{50} values conducted previously (Figure 21 A). When MYOF expressions were knocked down, there is significant decrease in IC_{50}. For A549, IC50 dropped to 4.19 µM and for H1299 it dropped to 9.56 µM as shown in Figure 24A. There was no significant difference with negative controls, A549 and H1299 scrambles, meaning that the changes in sensitivity is not due to transfection process.

The Figure 24 C shows western blot analysis of EGFR expression changes. Quantification of MYOF proteins show that transfection process was successful at knocking down the MYOF expressions in both A549 and H1299. Compared to controls, there was increase in EGFR expression in siMYOF cells. Looking at localization of the EGFR, EGFR expressions are on the cell membrane in controls for both A549 and H1299. When the MYOF protein is knocked down, the EGFR are more localized in the cytoplasm (Figure 24 D).

Using the IC50 concentrations from Figure 24 A were used to determine the concentration of erlotinib for the migration study. The erlotinib concentrations of 10 times and 5 times less than the IC50 values were used for the study. Figure 25 shows that the similar to the migration studies observed from before, siMYOF A549 and H1299 showed decreased migration. With lower concentration of erlotinib, there is no significant

difference in migration. With higher concentration of erlotinib, we see significant decrease migration. However, knockdown MYOF expression in addition to erlotinib treatment does not in further decreases in cell migration.

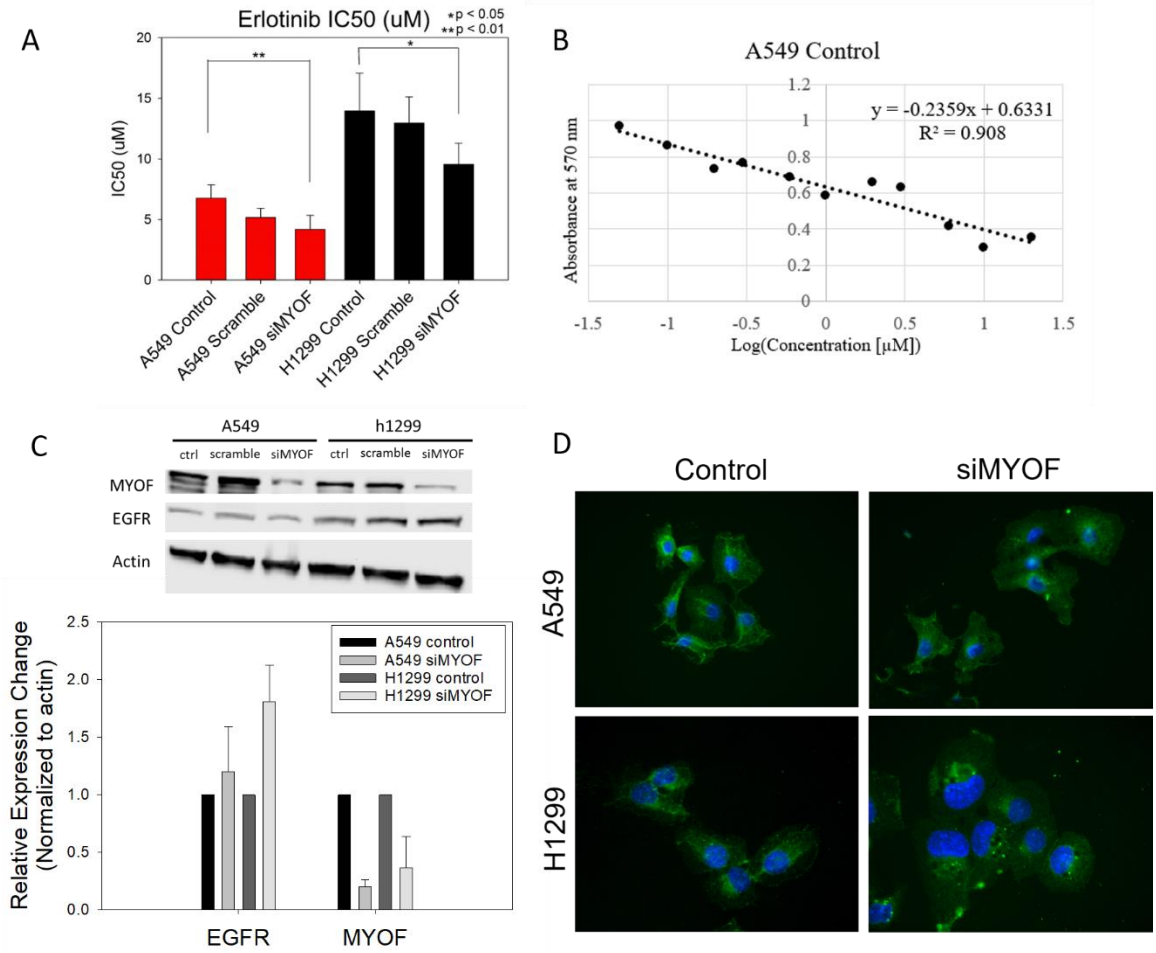

Figure 24. IC_{50} and EGFR expression analysis on control and siMYOF A549 and H1299 cells. A) IC_{50} study shows there is significant decrease in IC50 (μM) with decrease in MYOF expression for both A549 and H1299 cells. B) shows representative IC_{50} curve of A549 control. C) western blot of EGFR and MYOF expression. The graph shows that knocking down MYOF expression leads to increase in EGFR expression.
D) immunostaining for EGFR with control and siMYOF. When the MYOF protein is knocked down, the EGFR are more localized in the cytoplasm. (* $p<0.05$, ** $p<0.01$ one-way ANOVA).

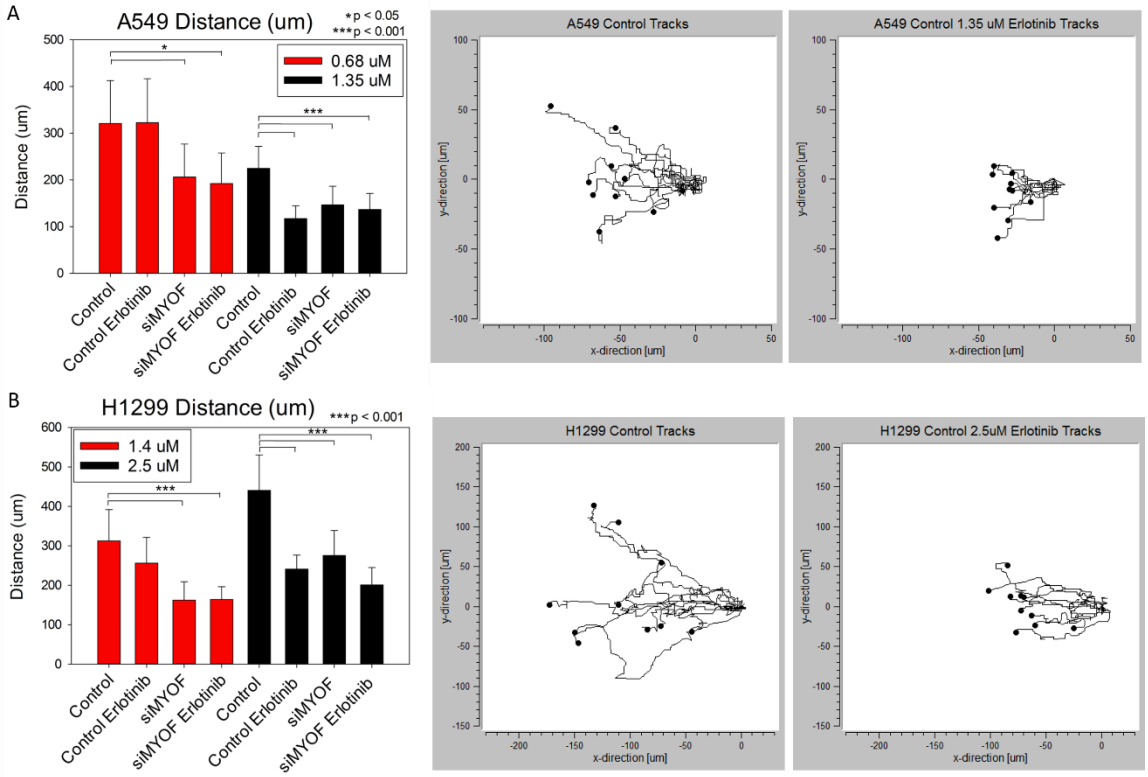

Figure 25. Effect of MYOF and Erlotinib on A549, H1299 migration. A) Migration distance and velocity for control and siMYOF A549 cells with two different concentrations of erlotinib (0.68 µM, 1.35 µM). B) Migration distance and velocity control and siMYOF H1299 cells with two different concentrations of Erlotinib (1.4 µM, 2.5 µM). (n=20, * $p<0.05$, *** $p<0.001$ one-way ANOVA).

Discussion

Cancer metastasis is cause of 90% of cancer-related fatalities. It is marked by detachment of cancer cells from primary tumor site and invasion into blood circulation[12]. The cells survive in the circulatory system and extravasate into different location for tumor growth. Epithelial-mesenchymal transition (EMT) where the cells lose the epithelial-like characteristics and become more motile has been one of the theories as to why cancer cells in primary site gain invasive potential[13-16]. Furthermore, recent studies have shown evidence that biophysical forces present in tumor microenvironment causes cancer cells to become more motile[17-21]. Studies have shown that increased solid stress in lung cancer causes increased migration in 2D[34, 35]. Another study has shown that there is increase in contractility and force generation in breast, prostate and lung cancer with increase in stiffness[38]. Collectively, these previous studies show that there are various biophysical mechanical forces that are present in tumor microenvironment that plays important role in tumor motility and drive metastasis. However, these studies have not looked at non-uniform deformation their role in migration.

Our study has used combination of computation modeling and *in-vitro* system to understand mechanical forces present in the lung tumor environment and analyze those stress in migration and drug resistance. Idealized lung modeling (Figure 14, Figure 15) demonstrated that there are numerous forces present in lung tumor microenvironment. Figure 26 shows the summary, where the within the stiff center of the tumor there is low cyclic strain. On the edge of the tumor there is high cyclic strain that gradients down to normal cyclic strain experienced by the normal lung tissues. There have been studies

done looking at different magnitudes of cyclic strain on lung cancer cell and how they influence cellular processes[106, 107]. Furthermore, it has been recently recognized that changes in tensile strain magnitude may also influence the cellular mechanobiology processes[108, 109]. However, to our knowledge people have not looked at the effect of strain gradient in lung cancer.

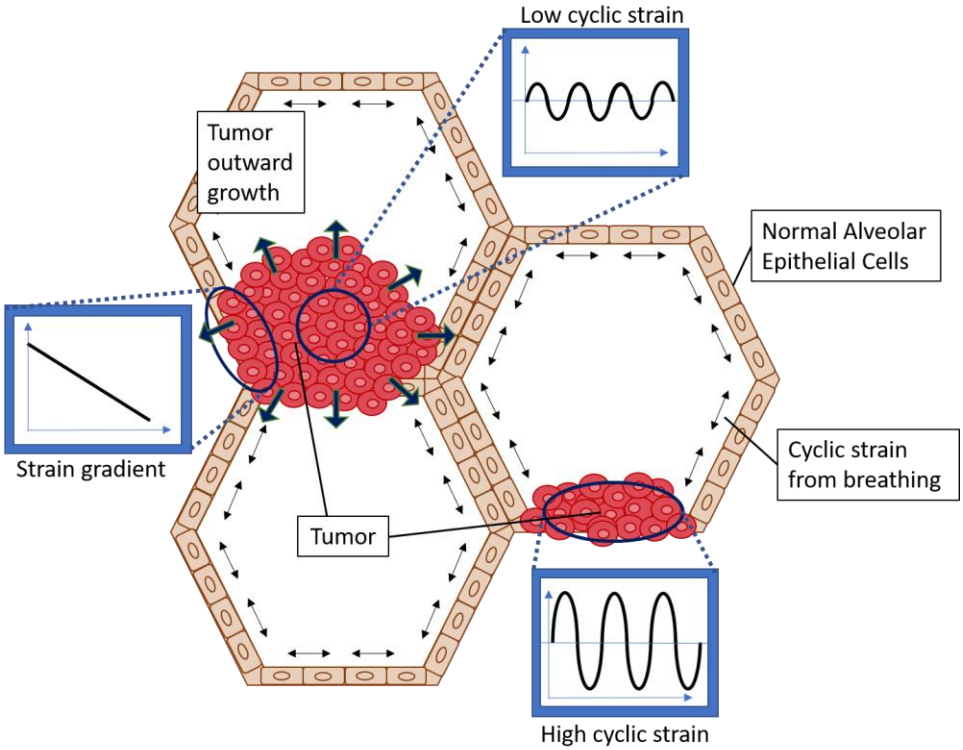

Figure 26. Schematic of biomechanical forces present in lung tumor microenvironment. There is low cyclic strain the stiff center of the tumor and high cyclic strain on the edge. There is strain gradient from the edge of the tumor to normal lung tissue.

Overall A549 and H1299 showed different migration patterns. For A549, there was increase in cluster size and decrease in circularity with increase in strain (Figure 16A). This indicates the cells are becoming more motile and invasive with higher strain.

The pattern for migration and invasiveness were similar when the non-uniform deformation was applied. With the addition of the stiff center, there is a gradual increase in strain (from inside clusters to outside clusters). We see similar pattern as we have seen in the uniform strain migration study, where we see increase in cluster size and decrease in circularity with gradual increase in strain (Figure 19). On the other hand, H1299 showed different pattern where with increase in strain applied, there was decrease in size change. The circularity of H1299 decreased at higher magnitude of uniform strain (Figure 16B), indicating that the cyclic strain does not affect the motility of the H1299 but increases the invasive potential of the cells. Similar pattern was observed with H1299 under non-uniform deformation where you see decrease in migration and circularity with high cyclic strain (Figure 20).

The mechanism of why these two cell lines exhibits different migration in response to uniform and non-uniform cyclic strain are unknown. However, the differences between the two cell lines may be due to the fact that they carry different Ras mutations. Different Ras isoforms have known to have different cellular functional properties[110]. Studies have demonstrated that the K-Ras mutation was more effective in stimulating cell motility compared to other Ras isoforms[111, 112]. This is consistent with our study where A549 which carries K-Ras mutation had higher increase in cell motility with increase in cyclic strain compared to H1299 with N-Ras mutation.

Interestingly, the EGFR expression changes with cyclic strain demonstrated similar pattern for both A549 and H1299. With increase in cyclic strain magnitude both cell types expressed more EGFR and became more sensitive to erlotinib treatment

(Figure 21). This means that the high tumor stiffness leads to increased drug resistance and as the cancer cells experience more cyclic strain, they become more sensitive to the treatment.

In-vivo it is hard to induce mechanical strain in localized area in the lung as a therapeutic approach. Therefore, as a therapeutic approach we have investigated the role of Myoferlin (MYOF) in EGFR regulation. MYOF is a membrane vesicle trafficking protein that have shown to decrease migration and invasion in in highly metastatic MDA-MB231 breast cancer cells[22, 23]. Overexpression of MYOF expression was found in breast cancer which plays important role in controlling EGFR degradation[24]. In lung cancer, increased MYOF expression correlates with worse outcomes[25]. Similar to findings in breast cancer, knocking down MYOF expression resulted in decreased migration (Figure 23). In addition, reduced MYOF expression showed similar trend with cells exposed to high cyclic strain where there was increased expression of EGFR and therefore became more sensitive to erlotinib treatment (Figure 24).

The effect of cyclic strain and MYOF expression have effect on erlotinib sensitivity, EGFR expression and localization for both A549 and H1299. Figure 27 shows possible downstream mechanisms that are being affected that leads cyclic strain and MYOF expression to have similar effect in EGFR regulation. Studies have shown that increased EGFR trafficking leads to more resistance to drug therapy[113]. Increased cyclic strain or decreased MYOF expression may decrease EGFR recycling that increases the

number of activated endosomal EGFR. Increased phosphorylated EGFR leads to higher erlotinib response. Further investigation needs to be done to confirm the theory.

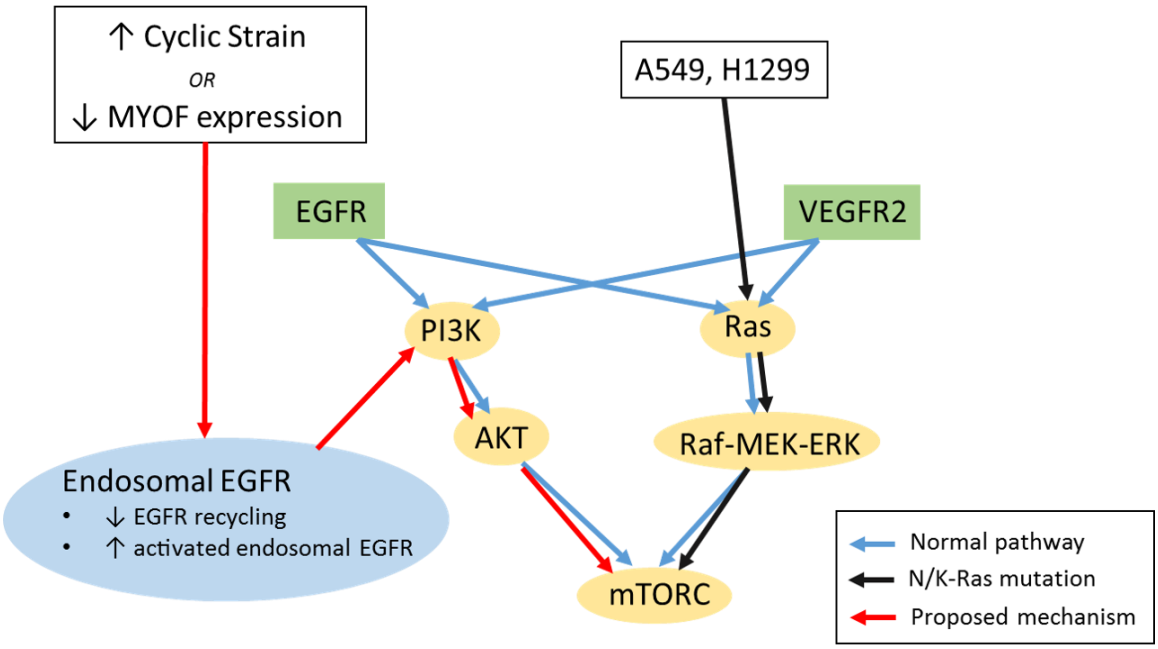

Figure 27. Relationship with cyclic strain, MYOF and EGFR pathway. The pathway shows the effect of cyclic strain and MYOF expression on EGFR trafficking that could affect the effectiveness of Erlotinib.

Through this study we have demonstrated there are heterogenous strain present in lung tumor microenvironment using computational modeling 1) low strain in stiff tumor center 2) high strain at the edge of tumor 3) strain gradient in the peritumoral region. We have created 2D *in-vitro* system to assess how heterogeneous strains affect lung cancer cell migration and drug resistance. We have found that high cyclic strain results in more migratory potential in lung cancer cell lines and they become more responsive to drug

therapy. Studies on MYOF expression have shown that knocking down MYOF expression in lung cancer cells can be a therapeutic approach by increasing sensitivity of the lung cancer cells to treatment. This chapter showed importance of heterogeneous mechanical properties in cancer cell migration and drug resistance. For the rest of the dissertation, we aim to develop imaging protocols that could detect these heterogenous strain fields as a biomarker or maybe early indicator of cancer development.

Chapter 3. Using Magnetic Resonance Elastography and Computational Modeling to Evaluate Heterogeneous Lung Biomechanical Properties during Cystic Fibrosis

The results of this study is under manuscript preparation and to be submitted in *NMR in Biomedicine*. Reference:

Cho, Y., Fakhouri, F., Englert, J., Kolipaka, A. & Ghadiali, S.N. Computational Using Magnetic Resonance Elastography and Computational Modeling to Evaluate Heterogeneous Lung Biomechanical Properties during Cystic Fibrosis. *NMR in Biomedicine*. (2021).

Introduction

Respiratory disease is a leading cause of death worldwide where lower respiratory tract infections, chronic obstructive pulmonary disease (COPD), lung cancer, and tuberculosis accounts for 9.5 million deaths annually[114]. In addition, the total number of deaths due to chronic respiratory diseases has increased 18% in the last three decades (1990-2017) and mortality rates for interstitial lung disease and pulmonary sarcoidosis has also increased[115]. The lung is a dynamic mechanical organ and under normal physiological conditions, contraction of diaphragmatic muscles during inspiration and chest wall relaxation during expiration results in cyclic inflation/deflation and deformation of lung tissue[41]. In healthy subjects, expansion of lung tissue during inspiration exposes cells in the lung microenvironment to cyclic tensile strains (i.e. stretching deformations) and several investigators have demonstrated that these normal

physiological strains (~5-10% magnitude) promote homeostatic cellular responses including surfactant production, epithelial cell proliferation and differentiation and prostacyclin production[44-47]. However, the degree of tissue deformation and tensile strain is highly dependent on the local stiffness of lung tissue and altered tissue stiffness and/or lung compliance during several pulmonary disorders may significantly alter the degree of tensile strain in the lung. As a result, developing non-invasive tools that can monitor changes in the lung's biomechanical properties during disease is a major area of research.

Several respiratory diseases involve changes in the lung's extracellular matrix (ECM) composition/structure results which alters lung tissue stiffness and inhibits normal lung function. For example, degradation of the ECM during COPD leads to parenchymal destruction, enlarged alveoli, decreased lung stiffness and reduced elastic recoil during exhalation[48]. Conversely, excessive matrix production and deposition during pulmonary fibrosis leads to increased lung stiffness and reduced lung expansion during inhalation[49]. Modulation of the ECM during lung cancer can also lead to increased lung stiffness[50] while excessive mucus production can elevate lung stiffness during cystic fibrosis [51]. Importantly, at the cellular level, altered substrate/tissue stiffness has been shown to directly modulate cellular function[52-54] and regulate the mechano-transduction processes that lead to fibrosis[55]. Therefore, developing non-invasive tools that can quantify regional lung stiffness is an important clinical need.

In addition to changes in tissue stiffness, it has been recently recognized that changes in tensile strain magnitude and the development of spatial gradients in strain may also influence the cellular mechanobiology processes that contribute to lung disease. For

example, excessive mechanical strain during artificial ventilation and during impaired alveolarization can exacerbate lung injury and inflammation[56] and can cause epithelial and endothelial cell injury and dysfunction[42, 57]. Furthermore, the heterogenous spatial distribution of strain within the deforming lung[58, 59] will lead to significant spatial gradients in strain and these spatial strain gradients have been shown to alter fibroblast orientation and contractility[60, 61]. Interestingly, although CT-based techniques have been used to document heterogenous lung deformation *in-vivo*[58], the heterogenous stiffness profiles that may lead to these spatial strain gradients has not been well quantified. In addition, most computational models of lung deformation assume homogenous stiffness distributions[82-84] and therefore cannot capture the spatial variations in lung deformation observed *in-vivo*. In this study, we develop a novel technique that uses Magnetic Resonance Elastography (MRE) and Finite Element Modeling (FEM) to non-invasively assess regional lung stiffness (i.e. shear modulus), strain magnitude and spatial strain gradients and then apply this technique to assess biomechanical properties in healthy and Cystic Fibrosis (CF) human subjects.

MRE is noninvasive imaging method that uses phase-contract (PC) magnetic resonance imaging (MRI) to measure shear stiffness in various organs such as lungs, pancreas, liver, and breast [95-99]. Our group has previously used MRE to quantify lung stiffness in human subjects and have demonstrated that mean lung stiffness at total lung capacity (TLC) was significantly higher than the mean lung stiffness at residual volume (RV)[95]. Unlike previous studies which used inverse techniques to estimate lung stiffness from CT-based measurements of lung deformation[92, 116], MRE is a direct measure of lung

tissue stiffness and can also resolve spatial and temporal variations in lung stiffness. Cystic fibrosis (CF) is autosomal recessive disease that is due to mutation of the cystic fibrosis transmembrane conductance regulator (CFTR) which leads to dysregulated chloride transport[117]. CF manifests in multiple organs and in the lungs leads to mucus accumulation, persistent bacterial and viral infection and scar tissue/cyst formation[118]. Since mucus accumulation and scar tissue formation likely lead to altered tissue stiffness, the first goal of this study is to use MRE to non-invasively measure heterogenous distributions of lung tissue stiffness in human CF patients. We then integrate these MRE stiffness measurements to into a novel FEM of lung deformation during the respiratory cycle and quantify heterogenous strain and strain gradient distributions. We hypothesize that accounting for spatial stiffness patterns will lead to higher strain gradients and that computational models which use homogenous properties underestimate these strain gradients. We also hypothesize that CF patients will exhibit higher stiffness/shear moduli, reduced strain magnitude and reduced strain gradients compared to measurements obtained in normal human adult volunteers.

Methods

Magnetic Resonance Elastography

Six normal adult volunteers n = 6 (age 24-29 yrs, 3 male, 3 female) and three cystic fibrosis patients (1 male and 2 females; 21-35 years old) were scanned after obtaining written informed consent and this study was approved by the Ohio State University Institutional Review Board (IRB). All images were obtained on a 1.5 T MRI scanner (Avanto, Siemens Healthcare, Erlangen, Germany) and all subjects were positioned supine and headfirst into the scanner. For MRE scans, mechanical vibrations at a frequency of 50 Hz were introduced separately into the right and left lungs using an acoustic speaker system. The passive driver was placed anteriorly on the apex of the right lung once and then on the left lung in a second scan. The mechanical driver system also consists of an active speaker which was placed outside the scanner room. The active and passive drivers were connected via a plastic tube.

Image Acquisition

MRE: A modified spin echo-echo planar imaging (SE-EPI) MRE sequence was used to acquire five axial slices of the lung. To minimize T2* effects and to achieve a relatively adequate MRE signal in the lungs, a SE based sequence was used. Additionally, to achieve a good signal in the lung, the shortest achievable TE of 11.6 ms was used. The sequence parameters are: field of view (FOV): 40x40cm^2; repetition time (TR): 400ms; acquisition matrix: 128x64 interpolated to 256x256; slice thickness: 10mm;

voxel size 1.56x1.56x10mm; echo train length: 9 (i.e. 7 shots to fully cover a single k-space); and 4 MRE phase offsets. For MRE, a 1:1 motion encoding gradient (MEG) was split into two unipolar lobes around the 180° refocusing pulse to achieve the minimum possible TE. Each Motion Encoding Gradient (MEG) lobe has a period of 2 ms (i.e. 250 Hz combined). In-plane and through plane mechanical motion were encoded with a 26 second breath hold for each. Scans were collected in two different breath hold states, residual volume (RV) and total lung capacity (TLC).

Lung Density: The lung's density (LD) changes during respiratory cycle as described previously[95, 96, 119-121] and quantifying lung density is essential for accurately estimating lung stiffness. In this study, lung density scans were performed using a fast GRE sequence[119, 120] with TR of 10 ms. To calculate T2* for RV, four different TEs of 1.07 (minimum TE achievable by the sequence), 1.5, 2, and 2.5ms were selected. Due to the low density of the lung at TLC relative to RV, the two shortest TEs were selected (i.e. 1.07 and 1.5ms) because of the rapid decay of the signal at TLC[119, 120]. This scan involved a single breath hold for each, RV and TLC. A whole-body coil was used with the following parameters: FOV: 50x50cm2, slice thickness: 10mm, acquisition matrix: 64x64, and number of averages: 4.

Image Analysis

Shear Stiffness: Both left and right lungs were included in this study by first drawing a region of interest (ROI) on each one of the 5 slices. Second, to eliminate

longitudinal and reflected waves, a 4th order Butterworth bandpass directional filter was applied in 8 directions with cutoff values of 4-40 waves/FOV at RV and 4-40 waves/FOV at TLC[122]. Filter cutoff values were selected based on the number of pixels manually measured in a wavelength. Third, lung shear stiffness was calculated for each slice individually by using 2D direct inversion[123] implemented in MRElab (Mayo Clinic, Rochester, Minnesota, USA). Finally, the resultant stiffness maps were median filtered (3x3 kernel)[124, 125] and 95th percentile[126] outliers were eliminated to remove noise imbedded in the lung's stiffness maps.

Lung Density: Lung density was estimated relative to a Gadolinium-doped water phantom that was placed on the volunteers' chest during lung density scans[119, 120]. The MR signal received from the phantom, which is mostly water, was considered as a good representation of lung's signal without any air. Therefore, an absolute measure of lung's density can be estimated relative to the Gadolinium-doped water phantom. First, the mean signal of the lungs (S) at a given TE (i.e. 1.07, 1.5, 2, 2.5 ms) was measured and the initial signal (I_0) of the lung for each pixel in the ROI of the whole lung

$$S = I_0 e^{TE*T2^*} \quad (1)$$

The resultant initial signal of the lung (I_0) was then used to calculated lung density in each pixel by

$$LD = I_0 * CF * I_{ph} \quad (2)$$

where Iph is the mean signal of the Gadolinium-doped water phantom, and CF is a correction factor. Due to the long decay constants of the phantom in comparison to the lung, a correction factor (CF) had to be determined to correct for the steady state signal that the phantom might reach at a TR of 10ms. By using the same fast GRE sequence, the CF was obtained by scanning the phantom twice with two different TRs of 10ms and 6 seconds. Then the CF was obtained by dividing mean phantom signal at TR = 6 seconds by mean phantom signal at TR = 10ms which resulted in a CF of 1.873[119-121].

Finite Element Modeling

MRE measurements of shear stiffness at RV were used to develop n=6 normal and n=3 cystic fibrosis patient-specific 3D FEM of lung deformation during normal tidal volume breathing. First, for each normal and CF subject, an outline of the lung in each axial MR scan was obtained using ImageJ and a custom written MatLab code that uses the non-uniform rational basis splines (NURBS) Toolbox[127] was used to create a 3D geometry of the lung section scanned during the MRI protocol (Figure 29 A). Due to processing of the stiffness maps as described in MRE methods, the size of the MRE shear stiffness maps were smaller than the lung geometry outlines. As a result, separate inner outlines were drawn using the MRE measurements (Figure 29 B) and used to create an inner 3D geometry using NURBS. The outer and inner 3D geometries were imported into

the COMSOL multi-physics finite element package where the outer geometry was used for boundary conditions specification while the inner geometry allowed for (Figure 29 C) for direct specification of spatial distributions in shear modulus (G). Specifically, the MRE measurements of shear modulus obtained in each plane (Figure 1B) were interpolated using a 3D linear interpolation function and this function was used to directly specify shear modulus in the inner region. For these studies, the shear modulus in the outer region was assumed to be equal to the average shear modulus within the entire model. The resulting model was then meshed with quadratic tetrahedral elements (Figure 29 C) and the Solid Mechanics module in COMSOL was used simulate lung tissue deformation during normal tidal volume respiration by specifying appropriate material models and boundary conditions.

The time-dependent equations governing tissue deformation solved in COMSOL were:

$$\rho \frac{\partial^2 \boldsymbol{u}}{\partial t^2} = \nabla \cdot (FS)^T \quad F = I + \nabla \boldsymbol{u} \quad S = \frac{\partial W}{\partial \epsilon} \quad \varepsilon = \frac{1}{2}(F^T F - I) \tag{3}$$

where ρ is tissue density, **u** is the displacement field, *F* is the deformation gradient, *I* is the identity tensor, *S* is the second Piola-Kirchhoff stress tensor, *W* is the strain energy density and ε is the strain tensor. Previous studies indicate that finite element models of lung deformation that utilize a two-parameter Mooney-Rivlin hyperelastic material model yielded the highest accuracy in capturing experimentally measured motion of lung tumors [82]. Therefore, in this study we implemented this material model by specifying:

$$W = c_1(I_1 - 3) + c_2(I_2 - 3) + \kappa(J-1)^2 \quad c_1 = c_2 = \frac{G}{4} \quad \kappa = \frac{2G(1+\nu)}{3(1-2\nu)} \tag{4}$$

Here, I_1 and I_2 are the first and second invariants of the isochoric elastic right Cauchy-Green tensor, κ is the bulk modulus and J is the elastic volume ratio. The shear modulus, G, was either specified as a constant value or specified based on MRE measurements as described above. Since the lung has been modeled with a range of Poisson's ratios, 0.2 – 0.5 [82, 85, 86, 128], we conducted a sensitivity analysis using values from Table 1 to determine how varying ν in this range influenced strain and strain gradient magnitudes. Figure 28 indicate that strain/strain gradients magnitudes are insensitive to changes in ν and therefore for all models in this study we specified ν=0.2 since that is the most common value used in the literature[82].

Parameter	Description	Value Range	Baseline Parameter Value
v	Poisson's Ratio	0.2 to 0.5	0.2
Es	Spring Stiffness	800 to 8e10 Pa	8 kPa
Go	Outer Lung Shear Stiffness	500 to 10000 Pa	3000 Pa
P	Boundary Load	100 to 1000 Pa	1000 Pa

Table 1. Biomechanical parameter values used for sensitivity analysis.

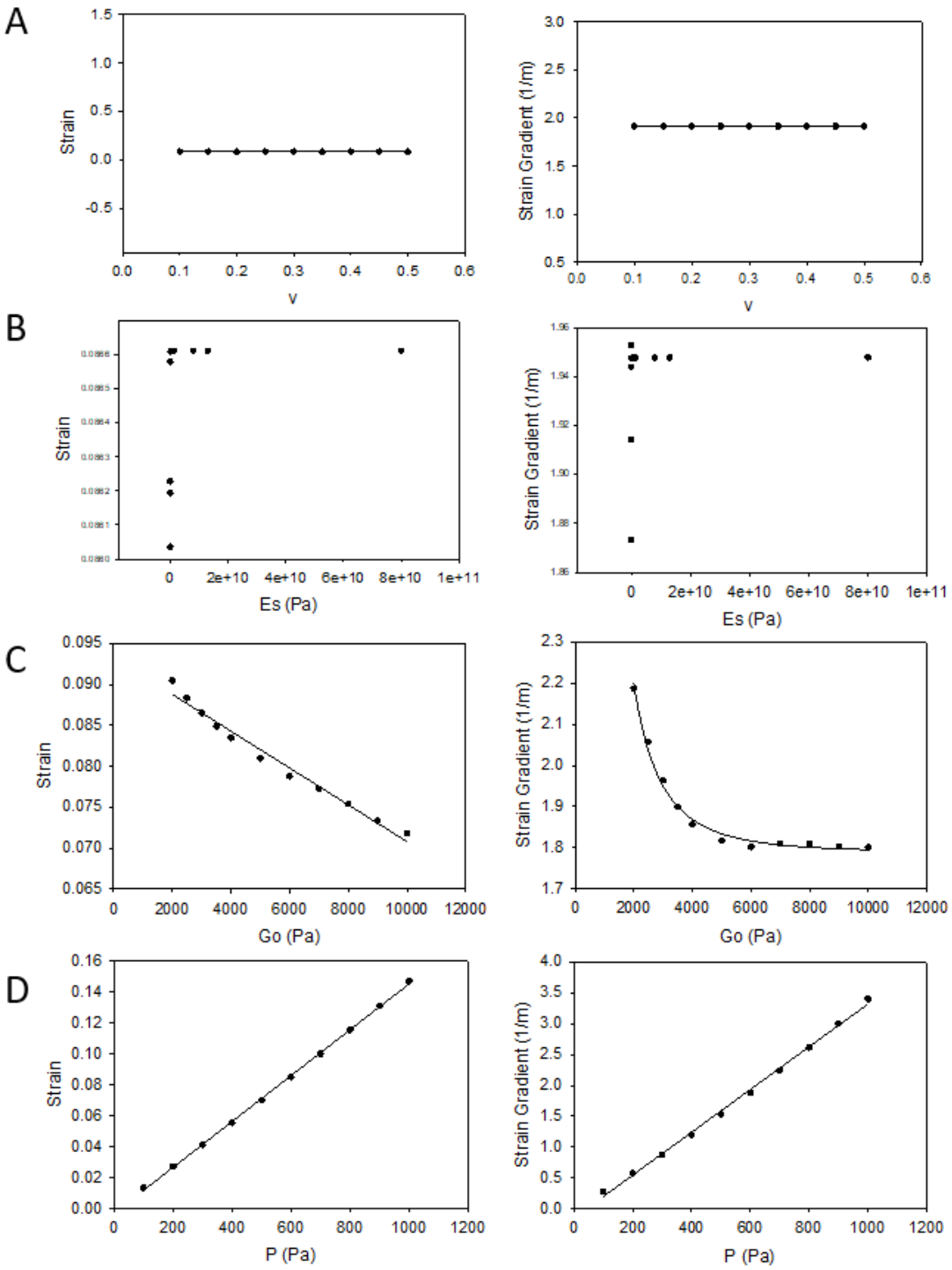

Figure 28. Sensitivity analysis using the values from Table 1 looking at strain and strain gradient. A) Poisson's ratio (ν) B) spring stiffness (E_s) C) outer lung shear stiffness (G_o) D) boundary load (P).

To simulate lung deformation during the respiratory cycle, several boundary conditions and loads were applied to the model (Figure 29 D). Because the patient specific geometries only represent the section of the lung scanned during the MRE protocol, a rolling/sliding boundary condition was applied to the upper and lower surfaces to restrict apical/basal movement to be in-plane only. To account for the restriction of lung deformation due to organs/tissues in the mediastinum cavity, we applied a spring foundation boundary condition to the mediastinal surfaces of the lung. Specifically, a restoring force that is linearly related to the local deformation field was applied and the spring constant in the normal and shear/tangential directions was specified as

$$k_n = \frac{E(1-v_t)}{d_s(1+v_t)(1-2v_t)} \quad k_s = \frac{G_t}{d_s} \quad G_t = \frac{E}{2(1+v_t)} \tag{5}$$

Where tissue stiffness was set to E=800kPa, Poisson's ratio to v_t=0.4 and tissue thickness to d_s=10 cm. These values allowed for medial movement of the lungs without affecting the strain magnitudes within the inner region of interest. To simulate negative pressure ventilation, a sinusoidal vacuum pressure was applied to the outer surfaces of the lung section and in this study, we used a vacuum pressure that ranged from 0 to a maximum vacuum pressure of -Π with a sinusoidal wave with frequency of 0.2 Hz. The maximum vacuum pressure Π was determined for each patient specific model and was based on the resultant volume ratio. Specifically, for an average normal adult, inspiration leads to an increased lung volume of ~0.5L (i.e. the tidal volume) about a the functional

residual capacity which is ~3L[129]. As a result, normal tidal ventilation results in a volume ratio change of 3.5L/3L= 1.167. As a result, Π was determined for in each patient specific model to give a volume ratio change of 1.167 and the average maximum vacuum pressure in normal adults was for uniform models were 751.8 $\pm$ 47.3 Pa and for heterogeneous models were 7338.5 $\pm$ 38.1 Pa. Since, CF patients have a 50% decreased tidal volume as compared to normal subjects[130], Π was set in these models to achieve a volume ratio change of 1.083 and this resulted in an average maximum vacuum pressure in CF subjects of 467.7 $\pm$ 29.0 Pa.

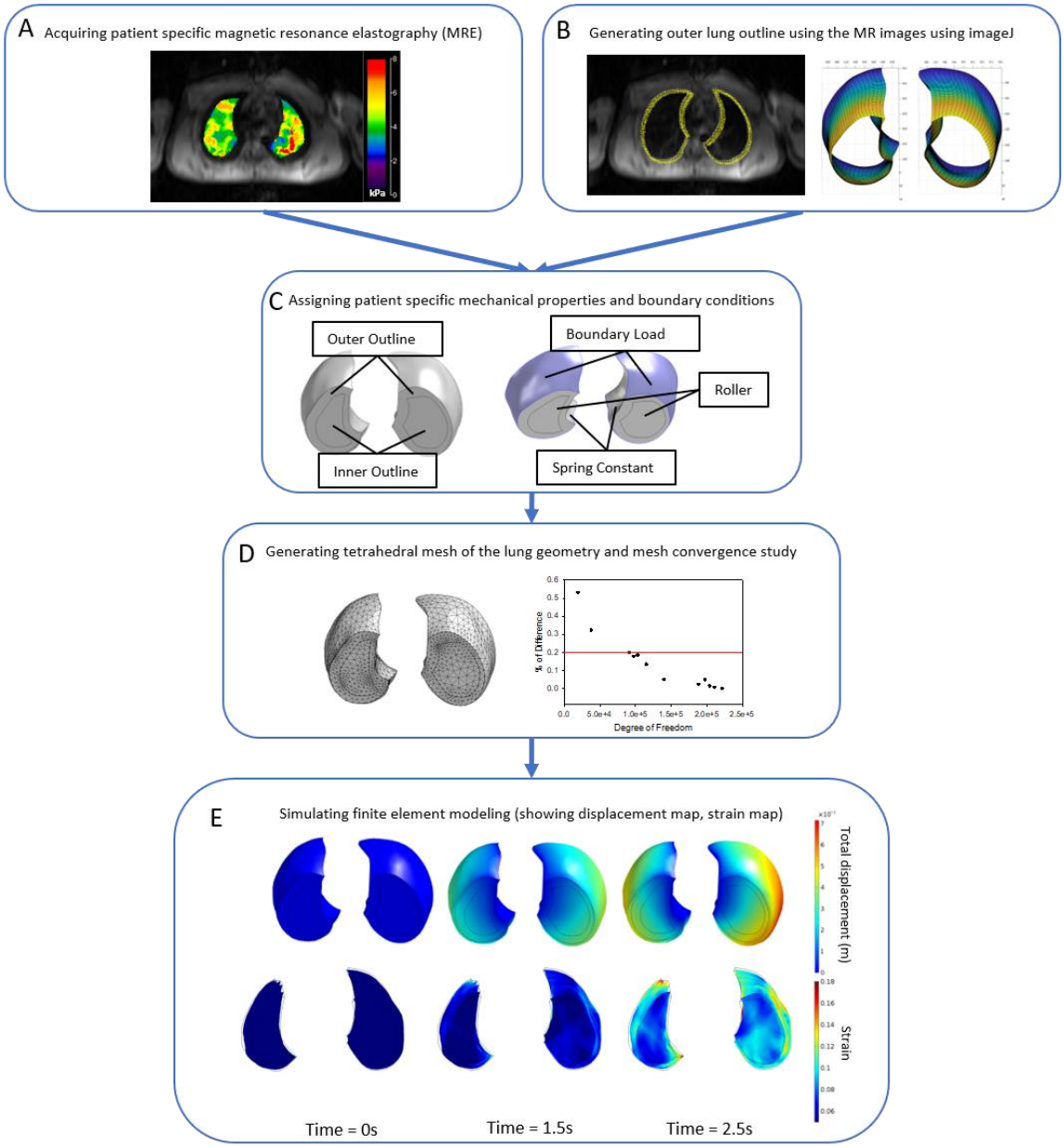

Figure 29. Flowchart of the lung finite element simulation. A) acquiring patient specific heterogeneous MRE stiffness maps B) reconstructing lung geometry using imageJ and MatLab C) outlines and stiffness maps are imported in to COMOSL Multiphysics and following boundary conditions are added D) Meshing of the lungs and the mesh convergence study E) representative simulated model showing displacement map and strain map.

Results

MRE Assessment of Stiffness in Normal and CF Patients

The magnitude image shows four snapshots of wave propagation for healthy volunteer and CF patient at RV (Figure 30A). Shorter wavelengths (distance from red to blue region) demonstrated in the healthy volunteer subjects compared to CF patients indicate that the normal volunteers have lower stiffness lungs. The calculated shear stiffness maps of the normal and CF volunteers further show the stiffness differences. Further analysis of the shear stiffness calculation shows that there is no significant difference between the normal and CF volunteers in both RV and TLC (Figure 30B). However, the CF consolidation regions are significantly stiffer than the normal lung. Figure 2C shows the representative distribution of the shear stiffness data calculated from the MRE measurement. The shear stiffness MRE measurements offer mechanical information of the normal and CF volunteer lungs however we do not clearly see the difference in stiffness values.

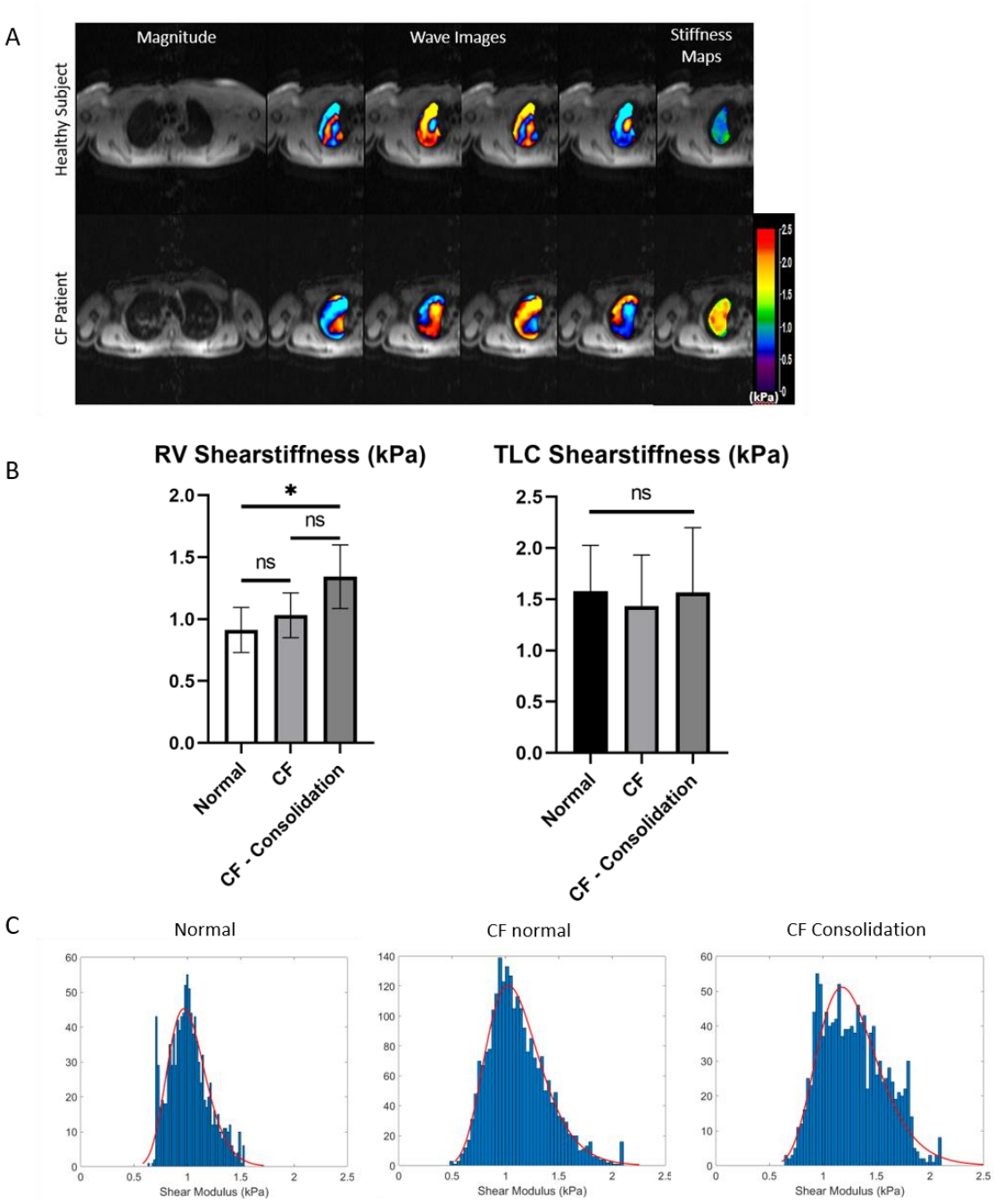

Figure 30. Magnetic resonance elastography data A) Wave image and shear stiffness map of normal and CF patient B) Shear stiffness (kPa) of normal, CF patients whole lung and CF region during residual volume and total lung capacity C) Shear stiffness (Pa) histogram distribution of normal and CF patient CF patients whole lung and CF consolidation.

Influence of Heterogenous Mechanical Properties on Computational Simulations and Tensile Strain Magnitude and Distribution

In this study, we sought to determine the relative importance of incorporating heterogenous mechanical properties into computational models of lung deformation and specifical sought to investigate if the assumption of homogeneous mechanical properties significantly influences the magnitude and distribution of tensile strain and spatial gradients of strain within the lung. Prior to simulating lung deformation with either homogeneous and heterogenous mechanical properties in all adult subjects, a mesh convergence study was conducted to determine an adequate mesh density/size. For this study, a representative adult geometry was meshed with different sized and therefore number of quadratic elements and the output of strain was plotted as a function of the number of elements and the degrees of freedom (**Figure 29** D). Results indicate that an average of 22,799 elements with 115,00 degrees of freedom yields a sufficiently accurate solution. Therefore, all models in this study were meshed with a similar number of elements and the average number of degrees of freedom used in the adult models was 115,520$\pm$15,538.76.

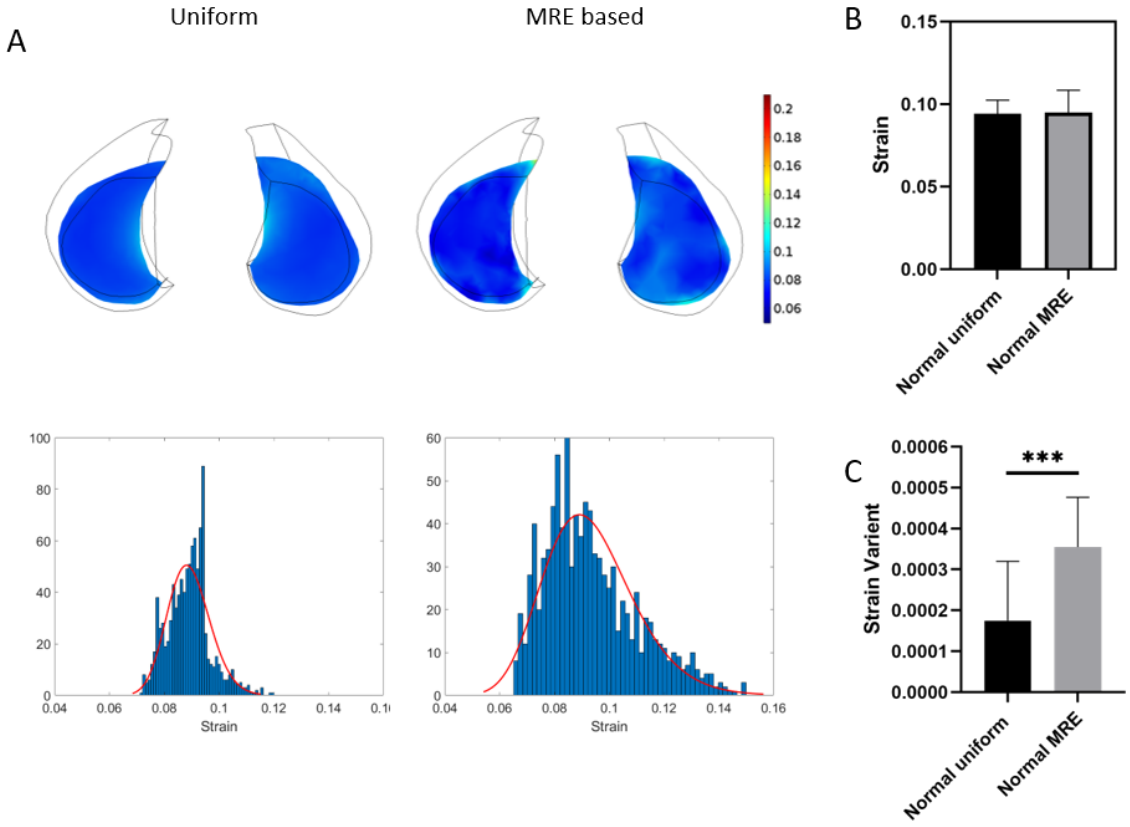

Figure 31. Comparing strain of uniform and MRE based normal lung models. A) sample strain map and histogram distribution of uniform and MRE based normal lung models. B) Graph of mean value of strain. There is no significance difference in mean of strain. C) Graph of variance of strain. MRE based lung models have significantly higher variance than uniform lung models by one-way repeated measures ANOVA *** $p<0.001$.

Figure 31 shows the strain of the lung models created by using average uniform stiffness and MRE calculated stiffness. As expected, the uniform stiffness lung model showed even distribution map and unimodal histogram (Figure 31 A) compared to MRE based models where there is wider distribution of strain. The average strain of uniform and MRE stiffness-based lung model were not significantly different (Figure 31 B). However, comparing the strain variance across the normal volunteers, there is significant

difference in strain variance between the normal and MRE based stiffness models. Further analyzing the strain gradient of the two different models of the normal volunteers there is distinctive difference between uniform and MRE based models (Figure 32). The color map of strain gradient shows that the model with MRE based stiffness have more diverse distribution of strain gradient as is evident in the histogram distribution (Figure 32 A). The Figure 32 B shows the average strain gradient of normal uniform lung models were significantly lower than that of lung models with MRE stiffness. The variance of the strain gradient across the different normal volunteers demonstrated that models with MRE stiffness measurements had more variability between the patient population. The normal models made with uniform stiffness and MRE based stiffness demonstrated that the mechanical characteristics are more prominent with spatial accuracy in stiffness.

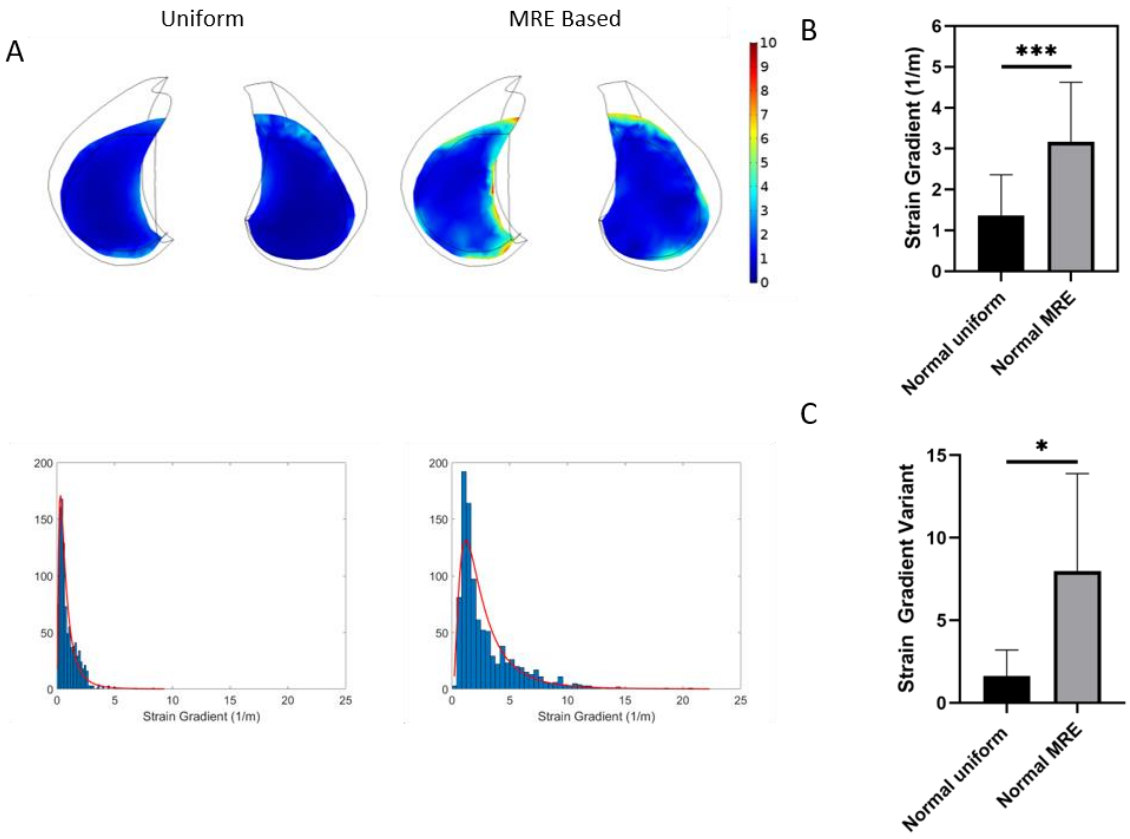

Figure 32. Comparing strain gradient of uniform and MRE based normal lung models. A) sample strain gradient map and histogram distribution of uniform and MRE based normal lung models. B) Graph of mean strain gradient. There is significance difference in strain gradient by one way repeated measures ANOVA ***$p<0.001$. C) Graph of variance of strain gradient. MRE based lung models have significantly higher variance than uniform lung models by one way repeated measures ANOVA * $p<0.05$.

Computational Analysis of Strain Magnitude in Normal and Cystic Fibrosis Lungs

The comparison of average values of strain and strain gradient between normal and CF patients showed more distinctive differences. Figure 33 shows the strain measurements of the normal and CF volunteers. The strain of the normal volunteers were significantly higher than CF volunteer lungs (Figure 33 A,D). The variability of the strain measurements were significantly higher in normal volunteers as shown in Figure 33 B,C.

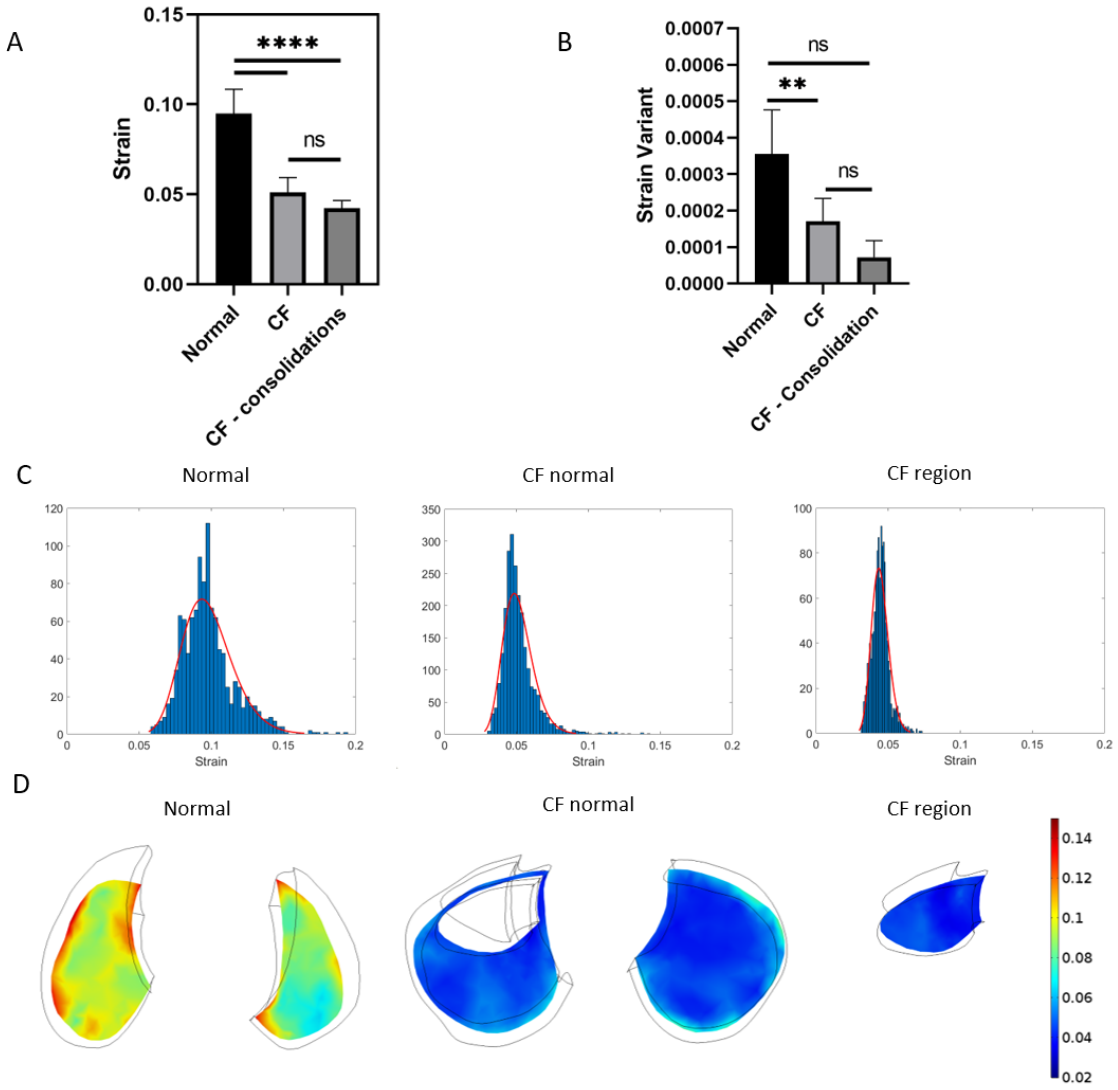

Figure 33. Comparing strain of normal and CF lung models A) Graph of mean of log value of strain. There is significance in strain by nested 1-way ANOVA ***p<0.0001. B) The graph of variance shows that there is higher variation in normal compared CF patients by ANOVA *p<0.001. C) Sample histograms of strain D) sample strain map of normal and CF lung models.

Computational Analysis of Strain Gradients in Normal and Cystic Fibrosis Lungs

The strain gradient measurement further characterized the CF consolidation regions within the lungs. The strain gradient was significantly different between normal and CF patients as expected but furthermore, the strain gradient values were significantly smaller in the region of CF consolidation (Figure 34 A, D). The variability between the patients in normal and CF volunteers were not significantly different (Figure 34 B,C).

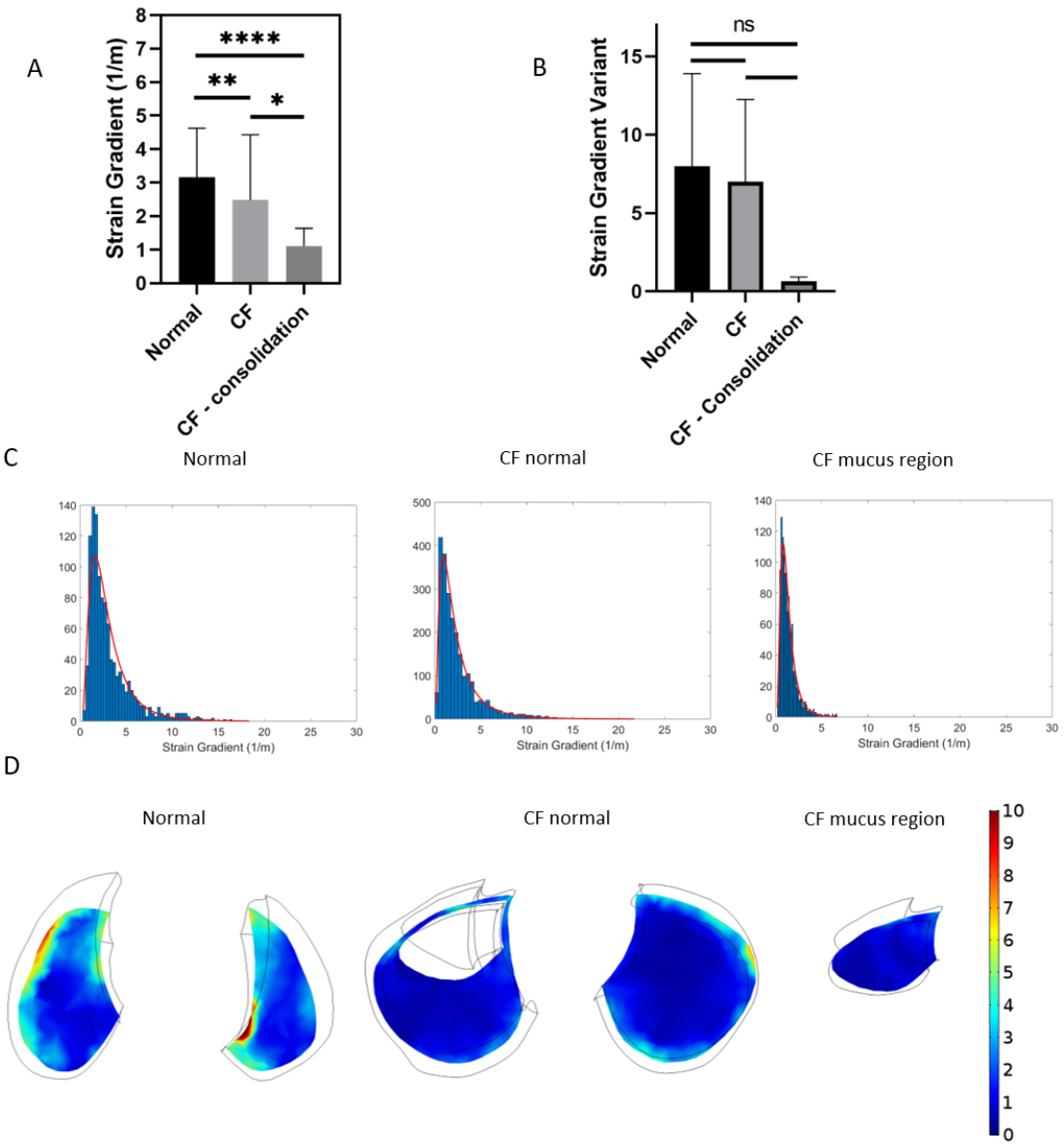

Figure 34. Comparing strain of normal and CF lung models A) Graph of mean of log value of strain gradient. There is significance in strain gradient by by nested 1-way ANOVA ***p<0.001, ** p<0.01, * p<0.05. B) The graph of variance shows that there is no significant difference. C) Sample histograms of strain gradient D) sample strain gradient map of normal and CF lung models.

Discussion

Respiratory disease is a leading cause of death worldwide it accounts for 9.5 million deaths[114]. The lung is a dynamic mechanical organ undergoing constant cyclic inflation/deflation and deformation of lung tissue during normal physiology of breathing[41]. The degree of tissue deformation and tensile strain is highly dependent on the local stiffness of lung tissue and altered tissue stiffness and/or lung compliance during several pulmonary disorders may significantly alter the degree of tensile strain in the lung. CT-based techniques have been used to document heterogenous lung deformation *in-vivo*[58], the heterogenous stiffness profiles that may lead to these spatial strain gradients has not been well quantified. In addition, most computational models of lung deformation assume homogenous stiffness distributions[82-84] and therefore cannot capture the spatial variations in lung deformation observed *in-vivo*. In our study, we have developed a novel technique that uses MRE and FEM to non-invasively assess regional lung stiffness (i.e. shear modulus), strain magnitude and spatial strain gradients.

Comparing FEM models ran with uniform stiffness and MRE heterogeneous stiffness demonstrated that there is more variation in values with the latter models. The uniform stiffness FEM models were able to closely predict the strain values (Figure 31) where there was no significant difference in strain values compared to the models with heterogeneous MRE stiffness. However, it was clear that variation between different normal volunteers were more apparent in FEM models with heterogeneous stiffness (Figure 31). This highlights importance in having heterogeneous stiffness in FEM to properly understand patient to patient difference. Furthermore, strain gradient analysis

further highlights the importance of the heterogeneous stiffness properties. There was significant difference in strain gradient and variation in strain gradient (Figure 32). The heterogeneous stiffness properties are able to capture patient to patient variability more than the average uniform stiffness FEM models. Current *in-vitro* models are limited to studying uniform oscillatory strain[45, 46, 62-66]. However, this FEM study suggests to understand the heterogeneous properties of the lung environment, investigating the effect of strain gradient is important.

There was no significant difference in MRE shear stiffness between normal and the CF patient lungs without consolidation. However, the MRE shear stiffness was able to detect the difference in CF consolidated regions (Figure 30B). The increased stiffness in the CF consolidation area suggest that the regions of mucus accumulation, persistent bacterial and viral infection and scar tissue/cyst formation[118] alter regional tissue stiffness. The further analysis of CF using FEM further confirms the finding from MRE shear stiffness. The CF consolidation higher stiffness with uniform distribution. The CF consolidation resulted in low strain and strain gradient values with very low variation (Figure 33, Figure 34) compared to normal volunteer lungs and CF lungs without consolidation. This study demonstrated that we are able to assess different mechanical characteristics in CF.

Through this study we have developed a novel technique that uses MRE and FEM to non-invasively assess regional lung stiffness (i.e. shear modulus), strain magnitude and spatial strain gradients. We were able to confirm that integrating heterogeneity MRE stiffness into FEM gives us more patient to patient variability and further gives us

information of strain magnitude and spatial strain gradients. Using the technique to study CF patients gave further validation that heterogeneity stiffness is important in characterizing and studying mechanical properties in lung disease. Furthermore, this study highlights limitation of current *in-vitro* systems studying only uniform deformation and calls for need of investigating the strain gradient in *in-vitro* studies.

Chapter 4: Development of Novel Screening Tool for Indeterminate Pulmonary Nodules Using Magnetic Resonance Elastography and Finite Element Modeling

The results of this study is under manuscript preparation and to be submitted in the *NMR in Biomedicine*, Reference:

Cho, Y., Fakhouri, F., Englert, J., Kolipaka, A. & Ghadiali, S.N. Using Mechanical Properties for Early Diagnosis for Indeterminate Pulmonary Nodules. *NMR in Biomedicine*. (2021).

Introduction

Lung cancer is the leading cause of cancer related deaths in the United States. In 2018, there was estimated to be 234,030 newly diagnosed lung cancer and 154,050 estimated deaths[1]. Lung cancer's five-year survival rate is 18.6% which is very low compared to other types of leading cancers such as colorectal (64.5%), breast (89.6%) and prostate (98.2%)[2]. This low survival rate is due to late detection from lack of proper screening – only 16% of lung cancer cases are diagnosed at early stage when the cancer is pre-metastatic and localized within the lungs[2]. Although, early detection through screening could increase the lung cancer survival rate, there is currently an ongoing debate regarding the cost-effectiveness and risks associated with lung cancer screening.

The American Cancer Society recommends yearly screening for individuals between 55 to 74 years old with smoking history of 30 pack year. Lung cancer screening

is done through low dose computed tomography (LDCT) where early detection can reduce lung cancer mortality by 14 to 20% in high-risk populations[3]. Although early screening reduces mortality rate for lung cancer, repetitive scans through LDCT has risks for radiation exposure, false positive and false negative findings and overdiagnosis[3].

Problem with early detection is mainly with small pulmonary nodules that are hard to diagnose. Indeterminate pulmonary nodules (IPN) are small lung nodules with diameter between 6-20mm in size that are found incidentally through computed tomography (CT) scans. 90% of IPN are incidentally found when patients are undergoing CT scans. Although majority of the IPNs are benign, current diagnosing tools are not optimal[4]. Current Fleischner Society 2017 Guidelines[5] look at the nodule size and risk factors (i.e. age, gender, family/smoking history) to determine if the patients need further follow-up. If there is increase in risk for lung cancer, patients undergo further imaging through PET scan and/or biopsy through bronchoscopy or fine needle biopsy[5]. Not only repetitive imaging methods will expose patients to high radiation but also biopsy methods are highly invasive and can lead to complications.

Lung is dynamically biophysical organ where normal alveolar epithelial cells experience ~4-10% cyclic strain[42, 43] and ultrasound elastography (UE) has shown that there is 40-fold decrease in cyclic strain in primary lung tumor[91]. Although biomechanical factors are significant part of the lung, there is limited information about different mechanical characteristics in lung tumor. Magnetic resonance electrography (MRE) is a non-invasive imaging technique that uses shear wave propagation to measure mechanical stiffness of soft tissues. Goal of the study was to: 1) characterize lung nodule

stiffness profiles using magnetic resonance and elastography (MRE) 2) develop finite element modeling incorporating heterogeneous stiffness maps to further investigate strain magnitude and spatial strain gradients of benign and malignant pulmonary nodules.

Methods

Patient Recruitment

Seven patients with 10 indeterminate pulmonary nodules (IPN) were recruited for this study (6 males and a female; 54.5±16.8 years old). All the 10 IPN have undergone PET scan or biopsy, three were malignant and 7 were benign nodules. Following criteria was used for recruitment of the IPN patients: 1) **Size:** > 1 cm in diameter, 2) **Location:** nodules located close to heart, large blood vessels were excluded from the study, 3) **Status:** patients have not undergone chemotherapy/radiation therapy. The exclusions were based on the resolution of the current magnetic resonance (MRE) technique and reduce any disturbance in the mechanical properties of the tumor. The IPN patients were scanned after obtaining written informed consent approved by The Ohio State University Institutional Review Board (IRB).

Magnetic Resonance Elastography

MRE was performed using a single shot spin echo-EPI (SE-EPI) sequence on a1.5T MRI scanner (MAGNETOM Aera, Siemens Healthcare, Erlangen, Germany). Two active speaker systems with three passive drivers were used to generate adequate vibration at a frequency of 50 Hz to both lungs. Single shot SE-EPI sequence was used for this study to eliminated heart and lung motion artifacts to allow wider range of detection for the lung nodules. The shortest possible TE of 15ms was used where the sequence parameters were: field of view (FOV) 450 x 450 mm^2, repetition time (TR) 1020ms, slice thickness 10mm, acquisition matrix 64 x 64 interpolated to 256 x 256,

voxel size 1.76 x1.76x10 mm^3, and 4 MRE phase offsets. As shown in (Figure 35), the sequence had two unipolar Motion Encoding Gradient (MEG) lobes around the 180° refocusing pulse to further reduce TE. Each MEG lobe has a period of 2.27 ms and both lobes were applied to read, phase, and slice gradients to encode in-plane and through plane motion in separate breath holds at residual volume (RV).

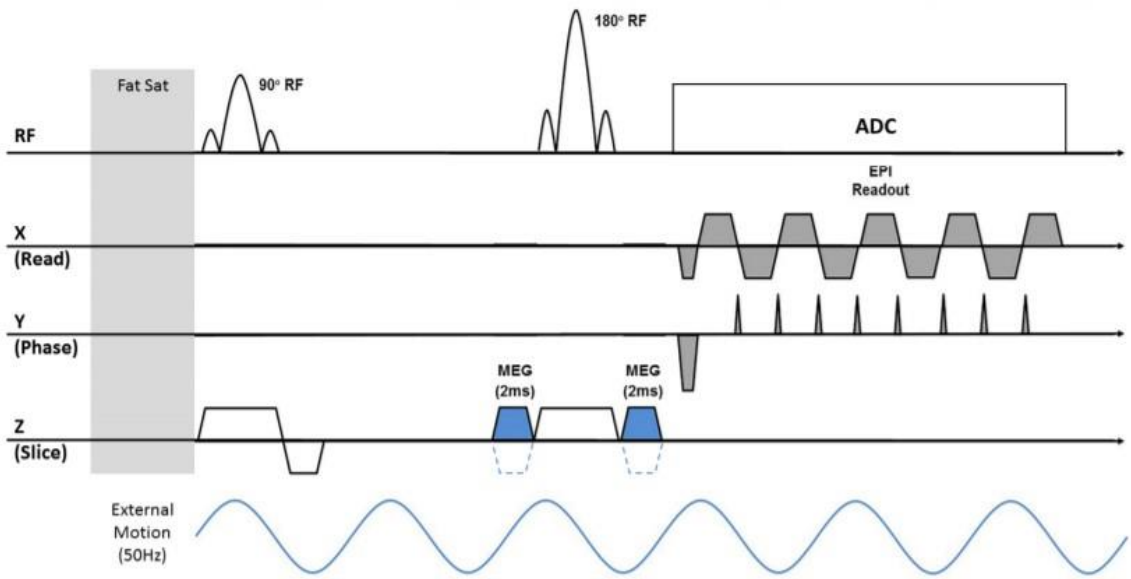

Figure 35. Pulse sequence diagram of SE-EPI MRE sequence. The unipolar MEGs (shaded in blue), which have 2 ms duration, are placed around the 180º refocusing pulse. They are also used as crushers to ensure minimum possible TE (i.e. 11.6 ms) and to avoid stimulated echoes. The MEGs alternate in polarity every TR, in which positive MEGs are shaded in blue and negative MEGs are the blue dashed lines.

Lung Density

The lung's density (LD) changes during respiratory cycle as described previously[95, 96, 119-121] and quantifying lung density is crucial for accurately estimating lung stiffness. In this study, lung density scans were performed using a fast GRE sequence[119, 120] with TR of 10 ms. To calculate T2* for RV, four different TEs of 1.07 (minimum TE achievable by the sequence), 1.5, 2, and 2.5ms were selected. Due to the low density of the lung at TLC relative to RV, the two shortest TEs were selected (i.e. 1.07 and 1.5ms) because of the rapid decay of the signal at TLC[119, 120]. This scan involved a single breath hold for each, RV and TLC. A whole-body coil was used with the following parameters: FOV: 50x50cm2, slice thickness: 10mm, acquisition matrix: 64x64, and number of averages: 4.

Shear Stiffness Calculation

Region of interest (ROI) were drawn on the whole lung for each slices of the lung and to eliminate longitudinal and reflected waves, 4th order Butterworth bandpass directional filter was applied in 8 directions with cut off values of 4-20waves/FOV[95, 122]. Shear stiffness was then calculated by using 2D direct inversion[123] implemented in MRElab (Mayo Clinic, Rochester, Minnesota, USA). The stiffness maps were median filtered (3x3 kernel)[124, 125] to remove noise embedded in the lung stiffness maps. To compare the shear stiffness between IPN and contralateral healthy lung tissue within a patient, an ROI was drawn on the IPN. Then the ROI of the same size was used to select region in the contralateral lung control. The ROI in contralateral lungs were equidistance

away from the outer lung. The location of the ROI on the contralateral lung was calculated by calculating relative distance ratio of the nodule relative to the outer lung and taking the same ratio on the contralateral lung.

Finite Element Modeling

Similar method was carried out for FEM of the IPN patients as the FEM models from chapter 3. First, for each normal and IPN subject, an outline of the lung in each axial MR scan was obtained using ImageJ and a custom written MatLab code that uses the non-uniform rational basis splines (NURBS) Toolbox[127] was used to create a 3D geometry of the lung section scanned during the MRI protocol. The MRE measurements of shear modulus obtained in each plane were interpolated using a 3D linear interpolation function and this function was used to directly specify shear modulus in the inner region. The sphere size equal to that if each IPN were drawn in each of the lungs (Figure 36). Similar to the ROI drawn for the MRE studies, identical spheres were drawn on the contralateral lung equidistance away from the outer wall of the lungs (Figure 36). The model was then meshed with quadratic tetrahedral elements and the Solid Mechanics module in COMSOL was used simulate lung tissue deformation during normal tidal volume respiration by specifying appropriate material models and boundary conditions.

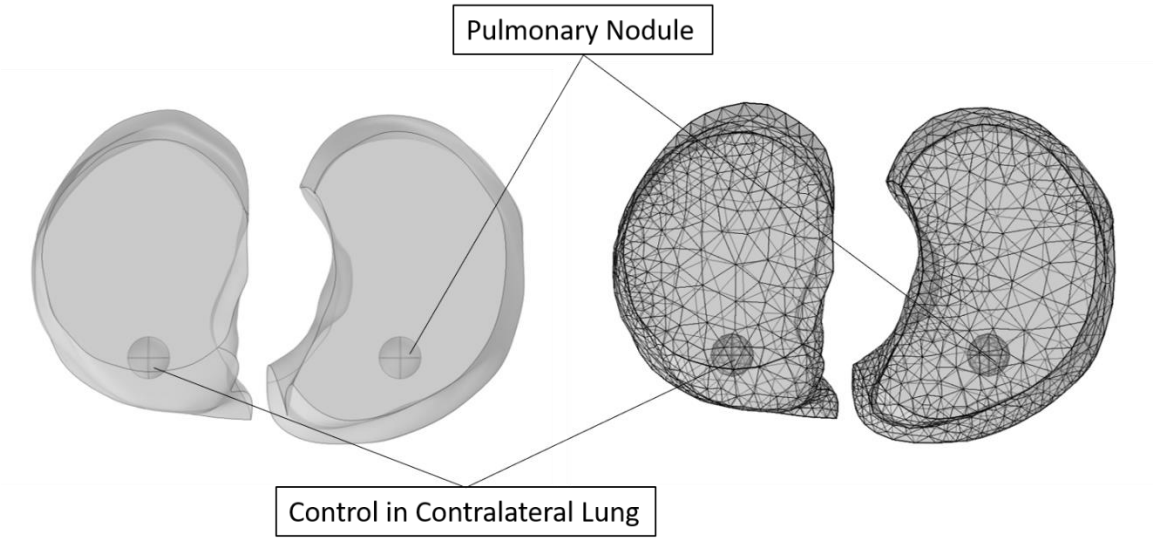

Figure 36. Image of representative indeterminate pulmonary nodule FEM model. Showing the location of the IPN and control region area in the contralateral lung.

The time-dependent equations governing tissue deformation solved in COMSOL were:

$$\rho \frac{\partial^2 \boldsymbol{u}}{\partial t^2} = \nabla \cdot (FS)^T \quad F = I + \nabla \boldsymbol{u} \quad S = \frac{\partial W}{\partial \epsilon} \quad \varepsilon = \frac{1}{2}(F^T F - I) \tag{1}$$

where ρ is tissue density, **u** is the displacement field, *F* is the deformation gradient, *I* is the identity tensor, *S* is the second Piola-Kirchhoff stress tensor, *W* is the strain energy density and ε is the strain tensor. Previous studies indicate that finite element models of lung deformation that utilize a two-parameter Mooney-Rivlin hyperelastic material model yielded the highest accuracy in capturing experimentally measured motion of lung tumors [82]. Therefore, in this study we implemented this material model by specifying:

$$W = c_1(I_1 - 3) + c_2(I_2 - 3) + \kappa(J - 1)^2 \quad c_1 = c_2 = \frac{G}{4} \quad \kappa = \frac{2G(1+\nu)}{3(1-2\nu)} \tag{2}$$

I_1 and I_2 are the first and second invariants of the isochoric elastic right Cauchy-Green tensor, κ is the bulk modulus and J is the elastic volume ratio. The shear modulus, G, was either specified as a constant value or specified based on MRE measurements as described above. As indicated in chapter 3, for Poisson's ratio ν=0.2 was used since these FEM lung models were independent of Poisson's ratio and that is the most common value used in the literature[82].

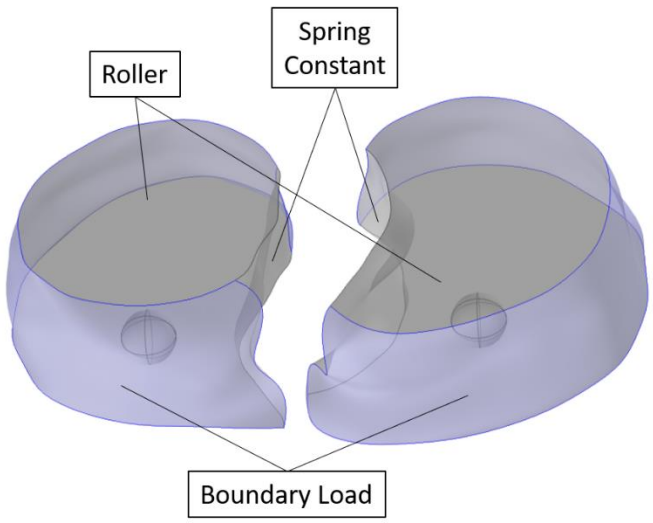

Figure 37. Boundary conditions of the FEM set up for IPN. Boundary load was applied on the outer lung boundary. Spring constant in the mediastinum cavity to restrict lung movement. Roller condition on top and bottom of the lung.

To simulate lung deformation during the respiratory cycle, several boundary conditions and loads were applied to the model (Figure 37). Because the patient specific geometries only represent the section of the lung scanned during the MRE protocol, a rolling/sliding boundary condition was applied to the upper and lower surfaces to restrict apical/basal movement to be in-plane only. To account for the restriction of lung deformation due to organs/tissues in the mediastinum cavity, we applied a spring foundation boundary condition to the mediastinal surfaces of the lung. Specifically, a restoring force that is linearly related to the local deformation field was applied and the spring constant in the normal and shear/tangential directions was specified as

$$k_n = \frac{E(1-v_t)}{d_s(1+v_t)(1-2v_t)} \quad k_s = \frac{G_t}{d_s} \quad G_t = \frac{E}{2(1+v_t)} \tag{3}$$

Where tissue stiffness was set to E = 800kPa, Poisson's ratio to v_t = 0.4 and tissue thickness to d_s=10 cm. These values allowed for medial movement of the lungs without affecting the strain magnitudes within the inner region of interest. To simulate negative pressure ventilation, a sinusoidal vacuum pressure was applied to the outer surfaces of the lung section and in this study, we used a vacuum pressure that ranged from 0 to a maximum vacuum pressure of -Π with a sinusoidal wave with frequency of 0.2 Hz. The maximum vacuum pressure Π was determined for each patient specific model and was based on the resultant volume ratio. Specifically, for an average normal adult, inspiration leads to an increased lung volume of ~0.5L (i.e. the tidal volume) about a the functional

residual capacity which is ~3L[129]. As a result, normal tidal ventilation results in a volume ratio change of 3.5L/3L= 1.167. As a result, Π was determined for in each patient specific model to give a volume ratio change of 1.167 and the average maximum vacuum pressure were 696.7 $\pm$ 144 Pa.

Post Data Analysis

The data analysis was down in three ways. First, the data were analyzed by looking at the average value of shear modulus (G), strain (ε) and strain gradient ($\nabla\varepsilon$) of IPN and control (contralateral side). Second, the average value of shear modulus (G), strain (ε) and strain gradient ($\nabla\varepsilon$) were calculated for malignant and benign nodules. Third, to account for patient-to-patient differences, relative difference in shear modulus (G), strain (ε) and strain gradient ($\nabla\varepsilon$) of pulmonary nodules were normalized to contralateral region of the lung.

$$G_{rel} = \frac{G_{cont} - G_{IPN}}{G_{cont}} \quad (4)$$

$$\varepsilon_{rel} = \frac{\varepsilon_{cont} - \varepsilon_{IPN}}{\varepsilon_{cont}} \quad (5)$$

$$\nabla\varepsilon_{rel} = \frac{\nabla\varepsilon_{cont} - \nabla\varepsilon_{IPN}}{\nabla\varepsilon_{cont}} \quad (6)$$

Statistical Analysis

GraphPad Prism 9 (GraphPad Software, San Diego, CA USA) was used for statistical analysis. Normality and outliers were tested for each data set using Shapiro-Wilk test at $\alpha = 0.05$. Non -parametric t-test was conducted to test the difference.

Results

Comparison of IPN and Control

The comparison between the indeterminate pulmonary nodules and controls (region in contralateral lung) of shear stiffness, strain and strain gradient show there is no significant difference (Figure 38). Figure 38A shows the median of the shear stiffness of the IPN is not significantly different than that of control. Similarly, for strain (Figure 38 B) and strain gradient (Figure 38 C) there were no significant difference value of strain and strain gradient between IPN and their contralateral lungs. This may be partially due to low sample size of each patient population. Furthermore, grouping malignant nodules and benign nodules together may be diluting the difference between the nodules and controls. Therefore, we carried out further analysis on comparing properties of the malignant and benign nodules.

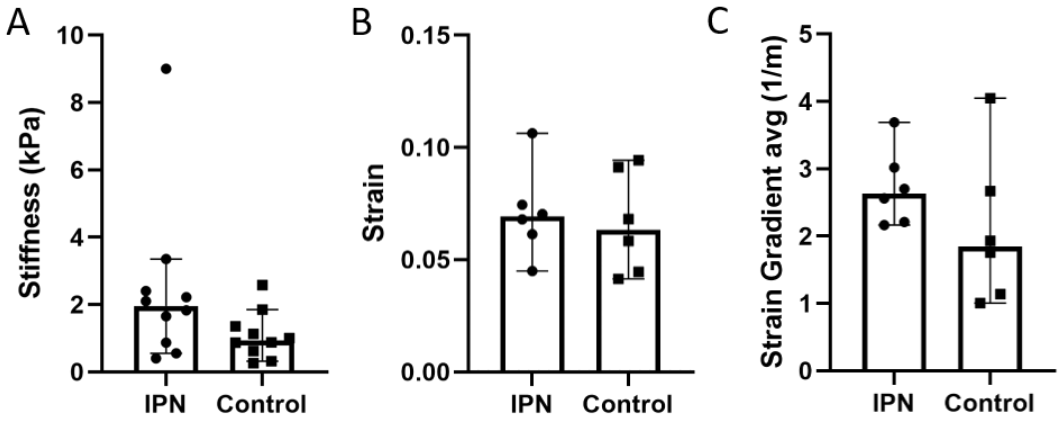

Figure 38. Comparison median values of IPN and control (region in contralateral lungs) of A) shear stiffness, B) strain, and C) strain gradient.

Comparison of the Malignant and Benign Nodules

Further analysis was conducted to compare the differences of mechanical properties (ie. stiffness, strain and strain gradient) in malignant and benign nodules. Figure 39 show representative image of the MRE stiffness and density map of the malignant and benign nodules. There is marked high stiffness in the malignant nodule (Figure 39 A) compared to benign nodules (Figure 39 B). Similarly, these representative images show there is high density in the malignant nodule (Figure 39 C) than benign nodule (Figure 39 D).

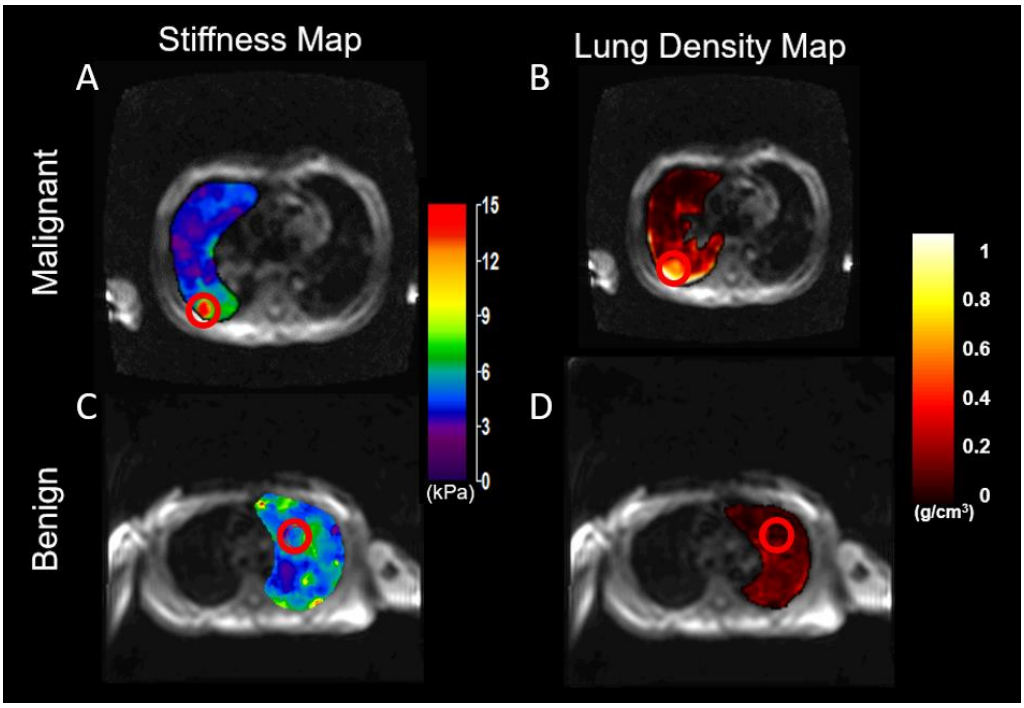

Figure 39. Representative images of MRE stiffness map and lung density map of malignant and benign nodule. Red circles highlight the regions with pulmonary nodules. A) Stiffness map of malignant nodule show high stiffness B) lung density map of malignant nodule shows high density in the area C) benign nodule stiffness map shows low stiffness D) lung density map of the benign nodule shows normal range of lung density.

Similarly, the representative images of the strain and strain gradient analysis through FEM shows differences between malignant and benign nodules. Malignant nodule shows low strain (Figure 40 A) and for strain gradient it is hard to determine if the gradient is changing much in the region. The benign nodules show similar strain (Figure 40 C) and strain gradient (Figure 40 D) values to the normal region of the lungs.

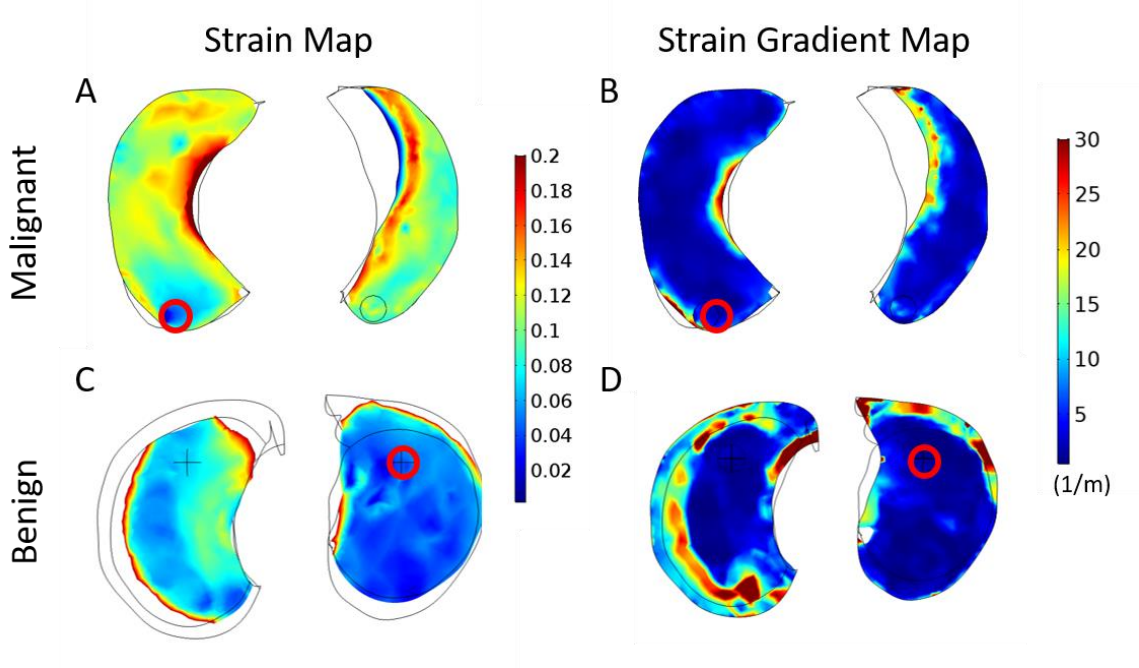

Figure 40. Representative images of FEM analysis of strain and strain gradient map of malignant and benign nodule. Red circles highlight the regions with pulmonary nodules. A) Malignant nodule shows low strain B) strain gradient value it is hard to determine C) benign nodule shows similar strain values as the normal region D) strain gradient values of benign nodules show similar values to the normal region.

Figure 41 shows comparison of malignant and benign nodules without normalization to the contralateral lungs. There was very high variability in the stiffness

values of the malignant nodules and as a result it was hard to detect any differences in the shear stiffness values between malignant and benign nodules (Figure 41 A). Interestingly, looking at strain and strain gradient values, we see a trend in these two datasets. Strain evaluation of the malignant and benign nodule show that there is lower strain in the malignant nodules (Figure 41 B). This may be due to the fact that the malignant nodules may be stiffer than the benign nodules. Furthermore because of this low strain in the region, when looking at strain gradient, within the malignant nodules there seems to be high strain gradient compared to benign nodules (Figure 41 C). Although there was no significant difference detected between malignant and benign nodules due to low sample size, there is a trend that malignant nodules are marked by lower strain and high gradient.

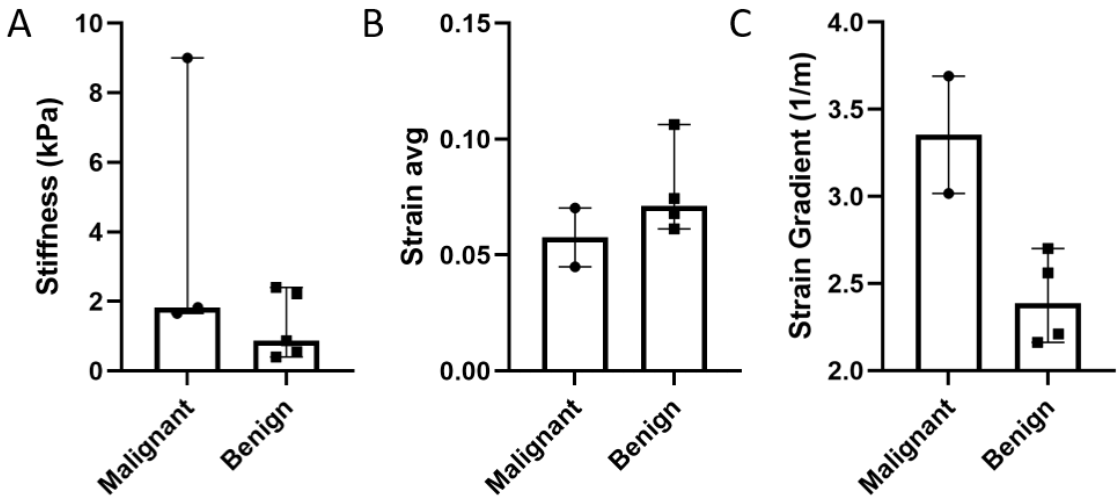

Figure 41. Comparison of malignant and benign nodules (without normalization to contralateral lungs) of A) shear stiffness B) strain C) strain gradient. There is no significant difference but there is trend in low strain and high strain gradient in malignant nodules.

Comparison of Malignant and Benign Nodules with Normalization

Although it is interesting to observe the trend in strain and strain gradient between the malignant and benign nodules, there is need for normalization of the nodules to the contralateral lungs. Figure 42 shows normalized comparison of malignant and benign nodules to the control (region in contralateral region of the lung) to account for patient-to-patient difference. The normalization of shear stiffness values show that the malignant nodules may be stiffer compared to benign nodules (Figure 42 A). Furthermore, both strain (B)and strain gradient values (Figure 42 C) show that there may be difference between malignant and benign nodules.

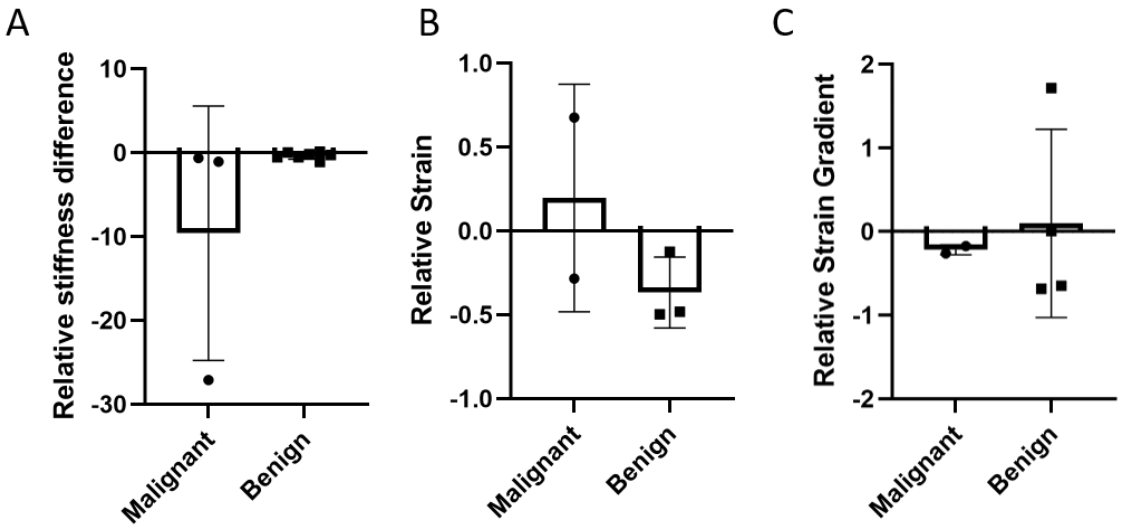

Figure 42. Comparison of malignant and benign nodules (with normalization to contralateral lungs) of A) shear stiffness B) strain C) strain gradient. There is no significant difference but there is trend in all shear stiffness, strain and strain gradient values.

Discussion

Lung cancer is leading cause of cancer related in the United States. Lung cancer's five-year survival rate is 18.6% which is very low compared to other types of cancer due to late detection from lack of proper screening[2]. Indeterminate pulmonary nodules (IPN) further pose a problem to early detection of lung cancer due to lack of proper guideline of managing and diagnosing IPN patient population. Current diagnosing tools – CT scan and PET scans expose patients to high amount of radiation and biopsy is invasive and could lead to complications. This calls for better markers and tools for managing and diagnosing pulmonary nodules.

Our work has shown the new technique of using MRE, non-invasive imaging system, with FEM could be a new diagnosing tool for IPN. Although the patient sample size were small, our work has shown that there is trend of high shear stiffness (Figure 42A), low strain (Figure 41 B) and high strain gradient (Figure 41 C) in the malignant nodules. This may be due to the fact that as the tumor progresses, there is increased in proliferation and recruitment of cells that makes the tumor more compact as well as there is increase remodeling of deposition of extracellular matrix[131, 132]. This leads to increased tumor stiffness. This explains why the malignant nodules exhibit higher shear stiffness in our study and result in low strain and high strain gradient.

Although the increased stiffness maybe related to nodule being malignant, there could be other implications. The benign nodules can exhibit higher shear stiffness if they contain calcification or tissues scarring. Calcification of the nodules can be both malignant and benign[133]. Calcification in malignant nodules may be mainly due to

primary cancer and metastatic bone cancer[133]. However, majority of the nodule calcification is from benign causes such as pulmonary hamartoma (benign lung tumor) or granuloma from infection in the lungs[133]. Problem with the calcification in the nodules can be resolved by analyzing the nodules with CT images to identify the calcification.

Pulmonary fibrosis is caused by inflammatory response in response to lung injury by other disease such as pneumonia, exposure to toxins, autoimmune disease[134]. During pulmonary fibrosis, excessive matrix production and deposition leads to increased lung stiffness[49]. These are some examples that having high shear stiffness in lung nodules does not necessarily mean that the nodule is malignant. Therefore, we need to continue the analysis of different types of lung nodules to observer if we can better characterize mechanical properties of different lung nodules.

Another limitation for our study is that in our study we have not included any nodules of size smaller that 1cm. The current resolution of the MRE technique we are using is low and cannot detect the mechanical properties below 1 cm. Therefore, we need to further investigate in increasing spatial resolution of MRE technique by increasing vibrational frequency of the drivers greater than 50 Hz.

Despite these limitations addressed in the discussion, this study is promising that shows that the lung has heterogeneous mechanical properties such as shear stiffness, strain and strain gradient. This study has demonstrated the different mechanical marker can be characterized using MRE imaging in combination with FEM. The identification of different mechanical markers can be a promising diagnosing tool for IPN patients.

Relying on the non-invasive method to follow the IPN patients is promising in reducing complications of current diagnosing tools.

Chapter 5: Conclusions and Future Directions

Lung cancer is leading cause of cancer-related deaths in the United States. U.S with 5-year survival rate of 18.6%. This low survival rate is due to late detection from lack of proper screening[2] and they develop resistance to drug therapy. Indeterminate pulmonary nodules (IPNs) are pulmonary nodules size between 7-20mm diameter solid nodules. 90% of IPNs are incidentally found and they are hard to diagnosis due to their small size and current diagnosis methods such as CT, PET scans and biopsy involve high exposure to radiation or invasive and could lead to complications.

The majority of lung cancer patients have non-small cell lung cancer (NSCLC) and 64% of these patients exhibit driver mutations such as epithelial growth factor receptor (EGFR), anaplastic lymphoma kinase (ALK) and Ras mutations. These patients have shown to have improved survival rate if they are treated with targeted therapies directed against the driver mutations. Although these patients initially show strong response to targeted therapies, most patients develop resistance to these targeted treatments through secondary point mutation and epithelial to mesenchymal transition (EMT).

The lung is a dynamic organ where alveolar epithelial cells are normally exposed to significant mechanical forces (i.e. ~8% cyclic strain, transmural pressure and shear stress) while primary lung tumor cells experience a 40-fold decrease in these mechanical

forces/strain. Although biomechanical factors in the tumor microenvironment have been shown to be a significant driver of cancer progression, there is limited information about how biophysical forces alters drug sensitivity in lung adenocarcinoma cells. Based on the known importance of mechanical forces/strain on lung injury and repair and the significant difference in cyclic strain applied to normal and cancer cells in the lung, we hypothesized that cyclic mechanical strain would activate important oncogenic pathways and alter drug sensitivity.

Magnetic resonance electrography (MRE) is a non-invasive imaging technique that uses shear wave propagation to measure mechanical stiffness of soft tissues. Dr. Kolipaka's lab has developed an MRE protocol that can measure temporally and spatially varying changes in lung tissue stiffness from normal adults. Furthermore, MRE has been used to quantify a 3-fold increase in lung tissue stiffness in fibrotic patients compared to normal controls. However, MRE has not been used to evaluate the stiffness profile of tumors within in lung cancer patients.

In this dissertation we test the hypothesis that the mechanical forces present within lung tumor microenvironment plays an important role in tumor progression and therapeutic response. Based on this hypothesis, we propose to 1) define different biophysical forces present in lung tumor microenvironment 2) investigate role of biomechanical forces in drug response and migratory behavior on the lung adenocarcinoma cells *in-vitro* and 3) verify and identify the biomechanical forces in patients with using the non-invasive imaging (i.e. MRE) and finite element modeling (FEM).

In chapter 2, the goal of the study is to develop a novel in-vitro system that better recapitulates the mechanical environment that develops during lung cancer and uses and idealized computational models of lung deformation to develop that in-vitro system. Furthermore, the second goal is to use the in-vitro system to understand how complex heterogenous changes in mechanical strain influence cancer cell migration and response to therapy. The finite element modeling of idealized lung model with tumor showed that there are heterogeneous strains and stresses present – low strain in stiff center of tumor, high strain and strain gradient in the peritumoral region. Using this, we have developed novel *in-vitro* system to generate non-uniform deformation. High strain and strain gradient led to increase in migration and increase in response to drug therapy. Furthermore, we have studied the effect of myoferlin (MYOF) protein as a therapeutic method and found MYOF knock down shows decrease in migration and increase in sensitivity to drug therapy.

In chapter 3, the goal of the study is to integrate these magnetic resonance elastography (MRE) stiffness measurements to into a novel FEM of lung deformation and quantify heterogenous strain and strain gradient distributions. Comparing FEM lung deformation with uniform average stiffness with MRE heterogeneous stiffness models, we have found that although the uniform FEM models was able to capture strain measurement, there was lack of variation in the values and failed to capture the changes in strain gradient within the model. After verifying the importance of heterogeneity in understanding lung deformation, this novel FEM technique to analyze the strain and strain distribution in cystic fibrotic (CF) patients. In CF patients the CF consolidation

areas were stiffer than other part of the lung and showed decrease in strain and smaller variation in strain gradient values.

In chapter 4, the goal of this study was to develop new diagnosing tool using MRE and FEM to investigate mechanical differences between benign and malignant pulmonary nodules. For this study we have recruited indeterminate pulmonary nodule (IPN) patients that have undergone diagnosis of the nodule to quantify heterogenous stiffness, strain and strain gradient distributions in benign and malignant nodules to compare and understand the different spatial gradients in tensile strain. We have seen increased stiffness and low strain and high strain gradient in malignant nodule patients.

Collectively, through this dissertation, we were able to show that there is heterogeneous mechanical characteristics – 1) low strain in stiff tumor 2) high magnitude of strain 3) strain gradient – that are present in lung microenvironment. High strain and strain gradient affect the cell migration and response to drug therapy. We have developed new technique that integrates MRE heterogenous stiffness into FEM to be able to characterize the mechanical properties indifferent lung disease.

Future Directions

In chapter 2, we were not able to further investigate into the relationship between cyclic strain and MYOF. Therefore, we hope to carry out experiments to further investigate the therapeutic application of MYOF by carrying out experiments looking at the effect of cyclic strain and non-uniform deformation on MYOF.

For chapter 3 of the dissertation, we have only compared the uniform stiffness FEM models with heterogeneous FEM models of the normal volunteers. Our future study includes, comparing the uniform average stiffness of the CF patients with the heterogeneous stiffness models to further validate the use of spatial heterogeneity is important in characterizing mechanical properties of the lung.

For chapter 4, we hope to continue the recruitment of the IPN patients to continue to understand the different mechanical characteristic between benign and malignant nodules. Furthermore, it would be interesting to conduct comparison analysis on patients that have not yet undergone biopsy/chemotherapy with patients that have gone biopsy/chemotherapy. This is to understand if any process of biopsy and chemotherapy would alter the mechanical properties of the nodule. Another future study for this chapter is to increase the resolution of the MRE technique to be able to have higher resolution for smaller nodules < 6mm.

Bibliography

1. Cancer Facts & Figures 2018. American Cancer Society: Atlanta.
2. Howlader N, N. A., Krapcho M, Miller D, Brest A, Yu M, Ruhl J, Tatalovich Z, Mariotto A, Lewis DR, Chen HS, Feuer EJ, Cronin KA, SEER Cancer Statistics Review. National Cancer Institute: Bethesda, MD, 1975-2017.
3. Chiles, C., Lung cancer screening with low-dose computed tomography. *Radiol Clin North Am* **2014,** *52* (1), 27-46.
4. Massion, P. P.; Walker, R. C., Indeterminate pulmonary nodules: risk for having or for developing lung cancer? *Cancer Prev Res (Phila)* **2014,** *7* (12), 1173-8.
5. MacMahon, H.; Naidich, D. P.; Goo, J. M.; Lee, K. S.; Leung, A. N. C.; Mayo, J. R.; Mehta, A. C.; Ohno, Y.; Powell, C. A.; Prokop, M.; Rubin, G. D.; Schaefer-Prokop, C. M.; Travis, W. D.; Van Schil, P. E.; Bankier, A. A., Guidelines for Management of Incidental Pulmonary Nodules Detected on CT Images: From the Fleischner Society 2017. *Radiology* **2017,** *284* (1), 228-243.
6. Zappa, C.; Mousa, S. A., Non-small cell lung cancer: current treatment and future advances. *Transl Lung Cancer Res* **2016,** *5* (3), 288-300.
7. Kris, M. G.; Johnson, B. E.; Berry, L. D.; Kwiatkowski, D. J.; Iafrate, A. J.; Wistuba, I. I.; Varella-Garcia, M.; Franklin, W. A.; Aronson, S. L.; Su, P. F.; Shyr, Y.; Camidge, D. R.; Sequist, L. V.; Glisson, B. S.; Khuri, F. R.; Garon, E. B.; Pao, W.; Rudin, C.; Schiller, J.; Haura, E. B.; Socinski, M.; Shirai, K.; Chen, H.; Giaccone, G.; Ladanyi, M.; Kugler, K.; Minna, J. D.; Bunn, P. A., Using multiplexed assays of oncogenic drivers in lung cancers to select targeted drugs. *JAMA* **2014,** *311* (19), 1998-2006.
8. Lynch, T. J.; Bell, D. W.; Sordella, R.; Gurubhagavatula, S.; Okimoto, R. A.; Brannigan, B. W.; Harris, P. L.; Haserlat, S. M.; Supko, J. G.; Haluska, F. G.; Louis, D. N.; Christiani, D. C.; Settleman, J.; Haber, D. A., Activating mutations in the epidermal growth factor receptor underlying responsiveness of non-small-cell lung cancer to gefitinib. *N Engl J Med* **2004,** *350* (21), 2129-39.
9. Sherwood, J.; Dearden, S.; Ratcliffe, M.; Walker, J., Mutation status concordance between primary lesions and metastatic sites of advanced non-small-cell lung cancer and the impact of mutation testing methodologies: a literature review. *J Exp Clin Cancer Res* **2015,** *34*, 92.
10. Morgillo, F.; Della Corte, C. M.; Fasano, M.; Ciardiello, F., Mechanisms of resistance to EGFR-targeted drugs: lung cancer. *ESMO Open* **2016,** *1* (3), e000060.
11. Casaluce, F.; Sgambato, A.; Sacco, P. C.; Palazzolo, G.; Maione, P.; Rossi, A.; Ciardiello, F.; Gridelli, C., Resistance to Crizotinib in Advanced Non-Small Cell Lung Cancer (NSCLC) with ALK Rearrangement: Mechanisms, Treatment Strategies and New Targeted Therapies. *Curr Clin Pharmacol* **2016,** *11* (2), 77-87.

12. Steeg, P. S., Metastasis suppressors alter the signal transduction of cancer cells. *Nat Rev Cancer* **2003,** *3* (1), 55-63.
13. Lamouille, S.; Xu, J.; Derynck, R., Molecular mechanisms of epithelial-mesenchymal transition. *Nat Rev Mol Cell Biol* **2014,** *15* (3), 178-96.
14. Polyak, K.; Weinberg, R. A., Transitions between epithelial and mesenchymal states: acquisition of malignant and stem cell traits. *Nat Rev Cancer* **2009,** *9* (4), 265-73.
15. Zhang, Y.; Weinberg, R. A., Epithelial-to-mesenchymal transition in cancer: complexity and opportunities. *Front Med* **2018,** *12* (4), 361-373.
16. Yilmaz, M.; Christofori, G., EMT, the cytoskeleton, and cancer cell invasion. *Cancer Metastasis Rev* **2009,** *28* (1-2), 15-33.
17. Butcher, D. T.; Alliston, T.; Weaver, V. M., A tense situation: forcing tumour progression. *Nat Rev Cancer* **2009,** *9* (2), 108-22.
18. Paszek, M. J.; Zahir, N.; Johnson, K. R.; Lakins, J. N.; Rozenberg, G. I.; Gefen, A.; Reinhart-King, C. A.; Margulies, S. S.; Dembo, M.; Boettiger, D.; Hammer, D. A.; Weaver, V. M., Tensional homeostasis and the malignant phenotype. *Cancer Cell* **2005,** *8* (3), 241-54.
19. Pathak, A.; Kumar, S., Biophysical regulation of tumor cell invasion: moving beyond matrix stiffness. *Integr Biol (Camb)* **2011,** *3* (4), 267-78.
20. Shieh, A. C., Biomechanical forces shape the tumor microenvironment. *Ann Biomed Eng* **2011,** *39* (5), 1379-89.
21. Tilghman, R. W.; Cowan, C. R.; Mih, J. D.; Koryakina, Y.; Gioeli, D.; Slack-Davis, J. K.; Blackman, B. R.; Tschumperlin, D. J.; Parsons, J. T., Matrix rigidity regulates cancer cell growth and cellular phenotype. *PLoS One* **2010,** *5* (9), e12905.
22. Volakis, L. I.; Li, R.; Ackerman, W. E.; Mihai, C.; Bechel, M.; Summerfield, T. L.; Ahn, C. S.; Powell, H. M.; Zielinski, R.; Rosol, T. J.; Ghadiali, S. N.; Kniss, D. A., Loss of myoferlin redirects breast cancer cell motility towards collective migration. *PLoS One* **2014,** *9* (2), e86110.
23. Li, R.; Ackerman, W. E.; Mihai, C.; Volakis, L. I.; Ghadiali, S.; Kniss, D. A., Myoferlin depletion in breast cancer cells promotes mesenchymal to epithelial shape change and stalls invasion. *PLoS One* **2012,** *7* (6), e39766.
24. Turtoi, A.; Blomme, A.; Bellahcène, A.; Gilles, C.; Hennequière, V.; Peixoto, P.; Bianchi, E.; Noel, A.; De Pauw, E.; Lifrange, E.; Delvenne, P.; Castronovo, V., Myoferlin is a key regulator of EGFR activity in breast cancer. *Cancer Res* **2013,** *73* (17), 5438-48.
25. Song, D. H.; Ko, G. H.; Lee, J. H.; Lee, J. S.; Lee, G. W.; Kim, H. C.; Yang, J. W.; Heo, R. W.; Roh, G. S.; Han, S. Y.; Kim, D. C., Myoferlin expression in non-small cell lung cancer: Prognostic role and correlation with VEGFR-2 expression. *Oncol Lett* **2016,** *11* (2), 998-1006.
26. Carmeliet, P.; Jain, R. K., Molecular mechanisms and clinical applications of angiogenesis. *Nature* **2011,** *473* (7347), 298-307.
27. Sugimoto, H.; Mundel, T. M.; Kieran, M. W.; Kalluri, R., Identification of fibroblast heterogeneity in the tumor microenvironment. *Cancer Biol Ther* **2006,** *5* (12), 1640-6.

28. Brittan, M.; Hunt, T.; Jeffery, R.; Poulsom, R.; Forbes, S. J.; Hodivala-Dilke, K.; Goldman, J.; Alison, M. R.; Wright, N. A., Bone marrow derivation of pericryptal myofibroblasts in the mouse and human small intestine and colon. *Gut* **2002,** *50* (6), 752-7.
29. Willis, B. C.; duBois, R. M.; Borok, Z., Epithelial origin of myofibroblasts during fibrosis in the lung. *Proc Am Thorac Soc* **2006,** *3* (4), 377-82.
30. Spaeth, E. L.; Dembinski, J. L.; Sasser, A. K.; Watson, K.; Klopp, A.; Hall, B.; Andreeff, M.; Marini, F., Mesenchymal stem cell transition to tumor-associated fibroblasts contributes to fibrovascular network expansion and tumor progression. *PLoS One* **2009,** *4* (4), e4992.
31. Erez, N.; Truitt, M.; Olson, P.; Arron, S. T.; Hanahan, D., Cancer-Associated Fibroblasts Are Activated in Incipient Neoplasia to Orchestrate Tumor-Promoting Inflammation in an NF-kappaB-Dependent Manner. *Cancer Cell* **2010,** *17* (2), 135-47.
32. Wells, J. M.; Gaggar, A.; Blalock, J. E., MMP generated matrikines. *Matrix Biol* **2015,** *44-46*, 122-9.
33. Jain, R. K.; Martin, J. D.; Stylianopoulos, T., The role of mechanical forces in tumor growth and therapy. *Annu Rev Biomed Eng* **2014,** *16*, 321-46.
34. Kao, S. H.; Wang, W. L.; Chen, C. Y.; Chang, Y. L.; Wu, Y. Y.; Wang, Y. T.; Wang, S. P.; Nesvizhskii, A. I.; Chen, Y. J.; Hong, T. M.; Yang, P. C., GSK3β controls epithelial-mesenchymal transition and tumor metastasis by CHIP-mediated degradation of Slug. *Oncogene* **2017,** *36* (42), 5916.
35. Tse, J. M.; Cheng, G.; Tyrrell, J. A.; Wilcox-Adelman, S. A.; Boucher, Y.; Jain, R. K.; Munn, L. L., Mechanical compression drives cancer cells toward invasive phenotype. *Proc Natl Acad Sci U S A* **2012,** *109* (3), 911-6.
36. Shukla, V. C.; Higuita-Castro, N.; Nana-Sinkam, P.; Ghadiali, S. N., Substrate stiffness modulates lung cancer cell migration but not epithelial to mesenchymal transition. *J Biomed Mater Res A* **2016,** *104* (5), 1182-93.
37. Swaminathan, V.; Mythreye, K.; O'Brien, E. T.; Berchuck, A.; Blobe, G. C.; Superfine, R., Mechanical stiffness grades metastatic potential in patient tumor cells and in cancer cell lines. *Cancer Res* **2011,** *71* (15), 5075-80.
38. Kraning-Rush, C. M.; Califano, J. P.; Reinhart-King, C. A., Cellular traction stresses increase with increasing metastatic potential. *PLoS One* **2012,** *7* (2), e32572.
39. Provenzano, P. P.; Eliceiri, K. W.; Campbell, J. M.; Inman, D. R.; White, J. G.; Keely, P. J., Collagen reorganization at the tumor-stromal interface facilitates local invasion. *BMC Med* **2006,** *4* (1), 38.
40. Shukla, V. C.; Duarte-Sanmiguel, S.; Panic, A.; Senthilvelan, A.; Moore, J.; Bobba, C.; Benner, B.; Carson, W. E.; Ghadiali, S. N.; Gallego-Perez, D., Reciprocal Signaling between Myeloid Derived Suppressor and Tumor Cells Enhances Cellular Motility and is Mediated by Structural Cues in the Microenvironment. *Adv Biosyst* **2020,** *4* (6), e2000049.
41. Levitzky, M., *Pulmonary Physiology*. 9th ed.; McGraw-Hill Education: 2018; p 320.

42. Waters, C. M.; Roan, E.; Navajas, D., Mechanobiology in Lung Epithelial Cells: Measurements, Perturbations, and Responses. *Compr Physiol* **2012,** *2* (1), 1-29.
43. Waters, C. M.; Sporn, P. H.; Liu, M.; Fredberg, J. J., Cellular biomechanics in the lung. *Am J Physiol Lung Cell Mol Physiol* **2002,** *283* (3), L503-9.
44. Liu, M.; Xu, J.; Tanswell, A. K.; Post, M., Stretch-induced growth-promoting activities stimulate fetal rat lung epithelial cell proliferation. *Exp Lung Res* **1993,** *19* (4), 505-17.
45. Diem, K.; Fauler, M.; Fois, G.; Hellmann, A.; Winokurow, N.; Schumacher, S.; Kranz, C.; Frick, M., Mechanical stretch activates piezo1 in caveolae of alveolar type I cells to trigger ATP release and paracrine stimulation of surfactant secretion from alveolar type II cells. *Faseb j* **2020,** *34* (9), 12785-12804.
46. Sanchez-Esteban, J.; Cicchiello, L. A.; Wang, Y.; Tsai, S. W.; Williams, L. K.; Torday, J. S.; Rubin, L. P., Mechanical stretch promotes alveolar epithelial type II cell differentiation. *J Appl Physiol (1985)* **2001,** *91* (2), 589-95.
47. Skinner, S. J.; Somervell, C. E.; Olson, D. M., The effects of mechanical stretching on fetal rat lung cell prostacyclin production. *Prostaglandins* **1992,** *43* (5), 413-33.
48. Suki, B.; Sato, S.; Parameswaran, H.; Szabari, M. V.; Takahashi, A.; Bartolák-Suki, E., Emphysema and mechanical stress-induced lung remodeling. *Physiology (Bethesda)* **2013,** *28* (6), 404-13.
49. Hinz, B., Mechanical aspects of lung fibrosis: a spotlight on the myofibroblast. *Proc Am Thorac Soc* **2012,** *9* (3), 137-47.
50. Parker, A. L.; Cox, T. R., The Role of the ECM in Lung Cancer Dormancy and Outgrowth. *Front Oncol* **2020,** *10*, 1766.
51. Hart, N.; Polkey, M. I.; Clément, A.; Boulé, M.; Moxham, J.; Lofaso, F.; Fauroux, B., Changes in pulmonary mechanics with increasing disease severity in children and young adults with cystic fibrosis. *Am J Respir Crit Care Med* **2002,** *166* (1), 61-6.
52. Raczkowska, J.; Orzechowska, B.; Patryas, S.; Awsiuk, K.; Kubiak, A.; Kinoshita, M.; Okamoto, M.; Bobrowska, J.; Stachura, T.; Soja, J.; Sładek, K.; Lekka, M., Effect of Substrate Stiffness on Physicochemical Properties of Normal and Fibrotic Lung Fibroblasts. *Materials (Basel)* **2020,** *13* (20).
53. Shukla, V. C.; Higuita-Castro, N.; Nana-Sinkam, P.; Ghadiali, S. N., Substrate stiffness modulates lung cancer cell migration but not epithelial to mesenchymal transition. *Journal of Biomedical Materials Research Part a* **2016,** *104* (5), 1182-1193.
54. Higuita-Castro, N.; Mihai, C.; Hansford, D. J.; Ghadiali, S. N., Influence of airway wall compliance on epithelial cell injury and adhesion during interfacial flows. *Journal of Applied Physiology* **2014,** *117* (11), 1231-1242.
55. Tschumperlin, D. J.; Ligresti, G.; Hilscher, M. B.; Shah, V. H., Mechanosensing and fibrosis. *J Clin Invest* **2018,** *128* (1), 74-84.
56. Gattinoni, L.; Marini, J. J.; Collino, F.; Maiolo, G.; Rapetti, F.; Tonetti, T.; Vasques, F.; Quintel, M., The future of mechanical ventilation: lessons from the present and the past. *Crit Care* **2017,** *21* (1), 183.

57. Kelly, G. T.; Faraj, R.; Zhang, Y.; Maltepe, E.; Fineman, J. R.; Black, S. M.; Wang, T., Pulmonary Endothelial Mechanical Sensing and Signaling, a Story of Focal Adhesions and Integrins in Ventilator Induced Lung Injury. *Front Physiol* **2019,** *10*, 511.
58. Hurtado, D. E.; Erranz, B.; Lillo, F.; Sarabia-Vallejos, M.; Iturrieta, P.; Morales, F.; Blaha, K.; Medina, T.; Diaz, F.; Cruces, P., Progression of regional lung strain and heterogeneity in lung injury: assessing the evolution under spontaneous breathing and mechanical ventilation. *Ann Intensive Care* **2020,** *10* (1), 107.
59. Hurtado, D. E.; Villarroel, N.; Andrade, C.; Retamal, J.; Bugedo, G.; Bruhn, A., Spatial patterns and frequency distributions of regional deformation in the healthy human lung. *Biomech Model Mechanobiol* **2017,** *16* (4), 1413-1423.
60. Chagnon-Lessard, S.; Jean-Ruel, H.; Godin, M.; Pelling, A. E., Cellular orientation is guided by strain gradients. *Integr Biol (Camb)* **2017,** *9* (7), 607-618.
61. Hsieh, H. Y.; Camci-Unal, G.; Huang, T. W.; Liao, R.; Chen, T. J.; Paul, A.; Tseng, F. G.; Khademhosseini, A., Gradient Static-Strain Stimulation in a Microfluidic Chip for 3D Cellular Alignment. *Lab Chip* **2014,** *14* (3), 482-93.
62. Lutz, A.; Jung, D.; Diem, K.; Fauler, M.; Port, F.; Gottschalk, K.; Felder, E., Acute effects of cell stretch on keratin filaments in A549 lung cells. *FASEB J* **2020,** *34* (8), 11227-11242.
63. Wang, W. H.; Hsu, C. L.; Huang, H. C.; Juan, H. F., Quantitative Phosphoproteomics Reveals Cell Alignment and Mitochondrial Length Change under Cyclic Stretching in Lung Cells. *Int J Mol Sci* **2020,** *21* (11).
64. Schmitt, S.; Hendricks, P.; Weir, J.; Somasundaram, R.; Sittampalam, G. S.; Nirmalanandhan, V. S., Stretching mechanotransduction from the lung to the lab: approaches and physiological relevance in drug discovery. *Assay Drug Dev Technol* **2012,** *10* (2), 137-47.
65. Ning, Q. M.; Sun, X. N.; Zhao, X. K., Role of mechanical stretching and lipopolysaccharide in early apoptosis and IL-8 of alveolar epithelial type II cells A549. *Asian Pac J Trop Med* **2012,** *5* (8), 638-44.
66. Lv, Z.; Wang, Y.; Liu, Y. J.; Mao, Y. F.; Dong, W. W.; Ding, Z. N.; Meng, G. X.; Jiang, L.; Zhu, X. Y., NLRP3 Inflammasome Activation Contributes to Mechanical Stretch-Induced Endothelial-Mesenchymal Transition and Pulmonary Fibrosis. *Crit Care Med* **2018,** *46* (1), e49-e58.
67. Huh, D.; Matthews, B. D.; Mammoto, A.; Montoya-Zavala, M.; Hsin, H. Y.; Ingber, D. E., Reconstituting organ-level lung functions on a chip. *Science* **2010,** *328* (5986), 1662-8.
68. Li, K.; Yang, X.; Xue, C.; Zhao, L.; Zhang, Y.; Gao, X., Biomimetic human lung-on-a-chip for modeling disease investigation. *Biomicrofluidics* **2019,** *13* (3), 031501.
69. Kızılkurtlu, A. A.; Polat, T.; Aydın, G. B.; Akpek, A., Lung on a Chip for Drug Screening and Design. *Curr Pharm Des* **2018,** *24* (45), 5386-5396.
70. Gkatzis, K.; Taghizadeh, S.; Huh, D.; Stainier, D. Y. R.; Bellusci, S., Use of three-dimensional organoids and lung-on-a-chip methods to study lung development, regeneration and disease. *Eur Respir J* **2018,** *52* (5).

71. Kimura, H.; Sakai, Y.; Fujii, T., Organ/body-on-a-chip based on microfluidic technology for drug discovery. *Drug Metab Pharmacokinet* **2018,** *33* (1), 43-48.
72. Hassell, B. A.; Goyal, G.; Lee, E.; Sontheimer-Phelps, A.; Levy, O.; Chen, C. S.; Ingber, D. E., Human Organ Chip Models Recapitulate Orthotopic Lung Cancer Growth, Therapeutic Responses, and Tumor Dormancy In Vitro. *Cell Rep* **2017,** *21* (2), 508-516.
73. Shrestha, J.; Razavi Bazaz, S.; Aboulkheyr Es, H.; Yaghobian Azari, D.; Thierry, B.; Ebrahimi Warkiani, M.; Ghadiri, M., Lung-on-a-chip: the future of respiratory disease models and pharmacological studies. *Crit Rev Biotechnol* **2020,** *40* (2), 213-230.
74. Spassov, S.; Wenzel, C.; Lozano-Zahonero, S.; Boycheva, D.; Streicher, L.; Schmidt, J.; Schumann, S., Sine ventilation in lung injury models: a new perspective for lung protective ventilation. *Sci Rep* **2020,** *10* (1), 11690.
75. Bobba, C. M.; Fei, Q.; Shukla, V.; Lee, H.; Patel, P.; Putman, R. K.; Spitzer, C.; Tsai, M.; Wewers, M. D.; Lee, R. J.; Christman, J. W.; Ballinger, M. N.; Ghadiali, S. N.; Englert, J. A., Nanoparticle delivery of microRNA-146a regulates mechanotransduction in lung macrophages and mitigates injury during mechanical ventilation. *Nat Commun* **2021,** *12* (1), 289.
76. Cressoni, M.; Gotti, M.; Chiurazzi, C.; Massari, D.; Algieri, I.; Amini, M.; Cammaroto, A.; Brioni, M.; Montaruli, C.; Nikolla, K.; Guanziroli, M.; Dondossola, D.; Gatti, S.; Valerio, V.; Vergani, G. L.; Pugni, P.; Cadringher, P.; Gagliano, N.; Gattinoni, L., Mechanical Power and Development of Ventilator-induced Lung Injury. *Anesthesiology* **2016,** *124* (5), 1100-8.
77. Khazaee, R.; McCaig, L. A.; Yamashita, C.; Hardy, D. B.; Veldhuizen, R. A. W., Maternal protein restriction during perinatal life affects lung mechanics and the surfactant system during early postnatal life in female rats. *PLoS One* **2019,** *14* (4), e0215611.
78. Sezik, M.; Antalyali, M.; Ozmen, O.; Haligur, M.; Koker, A.; Ozkaya, O.; Kosker, M., Ultra-high dose of intra-amniotic or direct fetal intramuscular betamethasone for lung maturation in the preterm goat model. *Eur J Obstet Gynecol Reprod Biol* **2012,** *164* (1), 15-23.
79. Fust, A.; Bates, J. H.; Ludwig, M. S., Mechanical properties of mouse distal lung: in vivo versus in vitro comparison. *Respir Physiol Neurobiol* **2004,** *143* (1), 77-86.
80. Fredberg, J. J.; Stamenovic, D., On the imperfect elasticity of lung tissue. *J Appl Physiol (1985)* **1989,** *67* (6), 2408-19.
81. Noferest, B. S.; Santhanam, A. P.; Ilegbusi, O. J., Effect of gravity on subject-specific human lung deformation. *Mathematical and Computer modelling of Dynamical Systems* **2018,** *24* (1), 87-101.
82. Tehrani, J. N.; Yang, Y.; Werner, R.; Lu, W.; Low, D.; Guo, X.; Wang, J., Sensitivity of tumor motion simulation accuracy to lung biomechanical modeling approaches and parameters. *Phys Med Biol* **2015,** *60* (22), 8833-49.

83. Eom, J.; Xu, X. G.; De, S.; Shi, C., Predictive modeling of lung motion over the entire respiratory cycle using measured pressure-volume data, 4DCT images, and finite-element analysis. *Med Phys* **2010,** *37* (8), 4389-400.
84. Yang, C.; Dong-Hai, Z.; Ling-Ying, L.; Yong-Hui, Y.; Yang, W.; Li-Wei, Z.; Rui-Guo, H.; Jia-Ke, C., Simulation of blast lung injury induced by shock waves of five distances based on finite element modeling of a three-dimensional rat. *Sci Rep* **2019,** *9* (1), 3440.
85. Villard, P.; Beuve, M.; Shariat, B.; Baudet, V.; Jaillet, F., Simulation of lung behaviour with finite elements: influence of bio-mechanical parameters. *Third International Conference on Medical Information Visualization Biomedical Visualization* **2005**, 9-14.
86. Werner, R.; Ehrhardt, J.; Schmidt, R.; Handels, H., Patient-specific finite element modeling of respiratory lung motion using 4D CT image data. *Med Phys* **2009,** *36* (5), 1500-11.
87. Mariappan, Y. K.; Glaser, K. J.; Ehman, R. L., Magnetic resonance elastography: a review. *Clin Anat* **2010,** *23* (5), 497-511.
88. Zhou, B.; Yang, X.; Zhang, X.; Curran, W. J.; Liu, T., Ultrasound Elastography for Lung Disease Assessment. *IEEE Trans Ultrason Ferroelectr Freq Control* **2020,** *67* (11), 2249-2257.
89. Zhang, X.; Osborn, T.; Zhou, B.; Meixner, D.; Kinnick, R. R.; Bartholmai, B.; Greenleaf, J. F.; Kalra, S., Lung Ultrasound Surface Wave Elastography: A Pilot Clinical Study. *IEEE Trans Ultrason Ferroelectr Freq Control* **2017,** *64* (9), 1298-1304.
90. Clay, R.; Bartholmai, B. J.; Zhou, B.; Karwoski, R.; Peikert, T.; Osborn, T.; Rajagopalan, S.; Kalra, S.; Zhang, X., Assessment of Interstitial Lung Disease Using Lung Ultrasound Surface Wave Elastography: A Novel Technique With Clinicoradiologic Correlates. *J Thorac Imaging* **2019,** *34* (5), 313-319.
91. Lim, C. K.; Chung, C. L.; Lin, Y. T.; Chang, C. H.; Lai, Y. C.; Wang, H. C.; Yu, C. J., Transthoracic Ultrasound Elastography in Pulmonary Lesions and Diseases. *Ultrasound Med Biol* **2017,** *43* (1), 145-152.
92. Hasse, K.; Hsieh, S. S.; O'Connell, D.; Stiehl, B.; Min, Y.; Neylon, J.; Low, D. A.; Santhanam, A. P., Systematic feasibility analysis of performing elastography using reduced dose CT lung image pairs. *Med Phys* **2020,** *47* (8), 3369-3375.
93. Zhou, B.; Bartholmai, B. J.; Kalra, S.; Osborn, T. G.; Zhang, X., Lung US Surface Wave Elastography in Interstitial Lung Disease Staging. *Radiology* **2019,** *291* (2), 479-484.
94. Miranda, D.; Jafari, P.; Dempsey, S.; Samani, A., 4D-CT Hyper-Elastography Using a Biomechanical Model. *Annu Int Conf IEEE Eng Med Biol Soc* **2020,** *2020*, 1791-1794.
95. Fakhouri, F.; Dong, H.; Kolipaka, A., Magnetic resonance elastography of the lungs: A repeatability and reproducibility study. *NMR Biomed* **2019,** *32* (7), e4102.
96. Mariappan, Y. K.; Glaser, K. J.; Hubmayr, R. D.; Manduca, A.; Ehman, R. L.; McGee, K. P., MR elastography of human lung parenchyma: technical development,

theoretical modeling and in vivo validation. *J Magn Reson Imaging* **2011,** *33* (6), 1351-61.
97. Kolipaka, A.; Schroeder, S.; Mo, X.; Shah, Z.; Hart, P. A.; Conwell, D. L., Magnetic resonance elastography of the pancreas: Measurement reproducibility and relationship with age. *Magn Reson Imaging* **2017,** *42*, 1-7.
98. Huwart, L.; Peeters, F.; Sinkus, R.; Annet, L.; Salameh, N.; ter Beek, L. C.; Horsmans, Y.; Van Beers, B. E., Liver fibrosis: non-invasive assessment with MR elastography. *NMR Biomed* **2006,** *19* (2), 173-9.
99. Balleyguier, C.; Lakhdar, A. B.; Dunant, A.; Mathieu, M. C.; Delaloge, S.; Sinkus, R., Value of whole breast magnetic resonance elastography added to MRI for lesion characterization. *NMR Biomed* **2018,** *31* (1).
100. Chen, M. C.; Chen, C. H.; Wang, J. C.; Tsai, A. C.; Liou, J. P.; Pan, S. L.; Teng, C. M., The HDAC inhibitor, MPT0E028, enhances erlotinib-induced cell death in EGFR-TKI-resistant NSCLC cells. *Cell Death Dis* **2013,** *4*, e810.
101. Levental, K. R.; Yu, H.; Kass, L.; Lakins, J. N.; Egeblad, M.; Erler, J. T.; Fong, S. F.; Csiszar, K.; Giaccia, A.; Weninger, W.; Yamauchi, M.; Gasser, D. L.; Weaver, V. M., Matrix crosslinking forces tumor progression by enhancing integrin signaling. *Cell* **2009,** *139* (5), 891-906.
102. Munson, J. M.; Shieh, A. C., Interstitial fluid flow in cancer: implications for disease progression and treatment. *Cancer Manag Res* **2014,** *6*, 317-28.
103. Nia, H. T.; Liu, H.; Seano, G.; Datta, M.; Jones, D.; Rahbari, N.; Incio, J.; Chauhan, V. P.; Jung, K.; Martin, J. D.; Askoxylakis, V.; Padera, T. P.; Fukumura, D.; Boucher, Y.; Hornicek, F. J.; Grodzinsky, A. J.; Baish, J. W.; Munn, L. L.; Jain, R. K., Solid stress and elastic energy as measures of tumour mechanopathology. *Nat Biomed Eng* **2016,** *1*.
104. Stylianopoulos, T., The Solid Mechanics of Cancer and Strategies for Improved Therapy. *J Biomech Eng* **2017,** *139* (2).
105. Huang, J. W.; Pan, H. J.; Yao, W. Y.; Tsao, Y. W.; Liao, W. Y.; Wu, C. W.; Tung, Y. C.; Lee, C. H., Interaction between lung cancer cell and myofibroblast influenced by cyclic tensile strain. *Lab Chip* **2013,** *13* (6), 1114-20.
106. Zhang, H. J.; Cai, S. X.; Lu, X.; Wang, Y. L.; Wang, H. B.; Huang, Q. P., [Effects of mechanical strain on the proliferation of pulmonary epithelial cells and reorganization of integrins]. *Sheng Wu Hua Xue Yu Sheng Wu Wu Li Xue Bao (Shanghai)* **2002,** *34* (6), 748-52.
107. Chapman, K. E.; Sinclair, S. E.; Zhuang, D.; Hassid, A.; Desai, L. P.; Waters, C. M., Cyclic mechanical strain increases reactive oxygen species production in pulmonary epithelial cells. *Am J Physiol Lung Cell Mol Physiol* **2005,** *289* (5), L834-41.
108. Balestrini, J. L.; Skorinko, J. K.; Hera, A.; Gaudette, G. R.; Billiar, K. L., Applying controlled non-uniform deformation for in vitro studies of cell mechanobiology. *Biomech Model Mechanobiol* **2010,** *9* (3), 329-44.
109. Neu, C. P.; Hull, M. L., Toward an MRI-based method to measure non-uniform cartilage deformation: an MRI-cyclic loading apparatus system and steady-state cyclic

displacement of articular cartilage under compressive loading. *J Biomech Eng* **2003,** *125* (2), 180-8.
110. Castellano, E.; Santos, E., Functional specificity of ras isoforms: so similar but so different. *Genes Cancer* **2011,** *2* (3), 216-31.
111. Voice, J. K.; Klemke, R. L.; Le, A.; Jackson, J. H., Four human ras homologs differ in their abilities to activate Raf-1, induce transformation, and stimulate cell motility. *J Biol Chem* **1999,** *274* (24), 17164-70.
112. Walsh, A. B.; Bar-Sagi, D., Differential activation of the Rac pathway by Ha-Ras and K-Ras. *J Biol Chem* **2001,** *276* (19), 15609-15.
113. Tomas, A.; Futter, C. E.; Eden, E. R., EGF receptor trafficking: consequences for signaling and cancer. *Trends Cell Biol* **2014,** *24* (1), 26-34.
114. W.H.O., *The Global Impact of Respiratory Disease*. Second ed.; European Respiratory Society, on behalf of the Forum of International Respiratory Societies: 2017.
115. Li, X.; Cao, X.; Guo, M.; Xie, M.; Liu, X., Trends and risk factors of mortality and disability adjusted life years for chronic respiratory diseases from 1990 to 2017: systematic analysis for the Global Burden of Disease Study 2017. *Bmj* **2020,** *368*, m234.
116. Hasse, K.; O'Connell, D.; Min, Y.; Neylon, J.; Low, D. A.; Santhanam, A., Estimation and validation of patient-specific high-resolution lung elasticity derived from 4DCT. *Med Phys* **2018,** *45* (2), 666-677.
117. Turcios, N. L., Cystic Fibrosis Lung Disease: An Overview. *Respir Care* **2020,** *65* (2), 233-251.
118. Hamutcu, R.; Rowland, J. M.; Horn, M. V.; Kaminsky, C.; MacLaughlin, E. F.; Starnes, V. A.; Woo, M. S., Clinical findings and lung pathology in children with cystic fibrosis. *Am J Respir Crit Care Med* **2002,** *165* (8), 1172-5.
119. Holverda, S.; Theilmann, R. J.; Sa, R. C.; Arai, T. J.; Hall, E. T.; Dubowitz, D. J.; Prisk, G. K.; Hopkins, S. R., Measuring lung water: ex vivo validation of multi-image gradient echo MRI. *J Magn Reson Imaging* **2011,** *34* (1), 220-4.
120. Theilmann, R. J.; Arai, T. J.; Samiee, A.; Dubowitz, D. J.; Hopkins, S. R.; Buxton, R. B.; Prisk, G. K., Quantitative MRI measurement of lung density must account for the change in T(2) (*) with lung inflation. *J Magn Reson Imaging* **2009,** *30* (3), 527-34.
121. Mariappan, Y. K.; Glaser, K. J.; Levin, D. L.; Vassallo, R.; Hubmayr, R. D.; Mottram, C.; Ehman, R. L.; McGee, K. P., Estimation of the absolute shear stiffness of human lung parenchyma using (1) H spin echo, echo planar MR elastography. *J Magn Reson Imaging* **2014,** *40* (5), 1230-7.
122. Manduca, A.; Lake, D. S.; Kruse, S. A.; Ehman, R. L., Spatio-temporal directional filtering for improved inversion of MR elastography images. *Med Image Anal* **2003,** *7* (4), 465-73.
123. Manduca, A.; Oliphant, T. E.; Dresner, M. A.; Mahowald, J. L.; Kruse, S. A.; Amromin, E.; Felmlee, J. P.; Greenleaf, J. F.; Ehman, R. L., Magnetic resonance elastography: non-invasive mapping of tissue elasticity. *Med Image Anal* **2001,** *5* (4), 237-54.

124. Huang, T. S.; Yang, G. J.; Tang, G. Y., A fast two-dimensional median filtering algorithm. *IEEE Transactions on Acoustics, Speech, and Signal Processing* **1979,** *27* (1), 13-18.
125. Frieden, B. R., A new restoring algorithm for the preferential enhancement of edge gradients. *Journal of the Optical Society of America* **1976,** *66* (3), 280.
126. Langford, E., Quartiles in Elementary Statistics. *Journal of Statistics Education* **2006,** *14* (3).
127. Spink, D. M. https://www.mathworks.com/matlabcentral/fileexchange/26390-nurbs-toolbox-by-d-m-spink.
128. Zhang, T.; Orton, N. P.; Mackie, T. R.; Paliwal, B. R., Technical note: A novel boundary condition using contact elements for finite element based deformable image registration. *Med Phys* **2004,** *31* (9), 2412-5.
129. StatPearls. 2021.
130. Colasanti, R. L.; Morris, M. J.; Madgwick, R. G.; Sutton, L.; Williams, E. M., Analysis of tidal breathing profiles in cystic fibrosis and COPD. *Chest* **2004,** *125* (3), 901-8.
131. Hanahan, D.; Weinberg, R. A., Hallmarks of cancer: the next generation. *Cell* **2011,** *144* (5), 646-74.
132. Balkwill, F. R.; Capasso, M.; Hagemann, T., The tumor microenvironment at a glance. *J Cell Sci* **2012,** *125* (Pt 23), 5591-6.
133. Khan, A. N.; Al-Jahdali, H. H.; Allen, C. M.; Irion, K. L.; Al Ghanem, S.; Koteyar, S. S., The calcified lung nodule: What does it mean? *Ann Thorac Med* **2010,** *5* (2), 67-79.
134. Meyer, K. C., Pulmonary fibrosis, part I: epidemiology, pathogenesis, and diagnosis. *Expert Rev Respir Med* **2017,** *11* (5), 343-359.